Imperial College London

Organic Mixed Ionic/Electronic Conductors for Bioelectronics Applications

Celia M Pacheco-Moreno

Supervised by Prof. Natalie Stingelin and Prof. Molly M Stevens

Submitted in part fulfilment of the requirements for the degree of
Doctor of Philosophy
Imperial College London - Department of Materials

March 2016

Abstract

The bioelectronics field has incorporated an increasing variety of conducting polymers in applications that involve mixed ionic/electronic transport, yet there is still a lack of design rules to purposefully tune the electronic and ionic contributions to a material's conductivity, as well as processing methods to further control and understand their interplay. New undoped co-polymers were explored as electroactive materials in aqueous media. The range of materials allowed establishing a simple design rule with potential to be explored in other model semiconductors. The most hydrophilic system showed promising response when benchmarked with poly(3,4-ethylenedioxythiophene):poly(styrene sulfonate) (PEDOT:PSS) in order to be employed in new operation modes of devices which rely on the electrochemical doping of the active layer, such as organic electrochemical transistors (OECTs). The capabilities of the most promising co-polymer were further exploited as an ion-to-electron converter by creating multicomponent systems that included a polar insulator to tune the ionic transport. The straightforward and chemically inert blending approach showed enhanced transport of ionic species while maintaining their electronic transport as well as displaying characteristic response times linked to the presence of the polar insulator. By using the semiconductor as a model system and controlling the volume of aggregates present in the solid-state by means of processing, a phenomenological description was given of ionic transport in different regions of semicrystalline polymers along with their associated decay rates. Finally, the effect of humidity in the charge transport of the undoped co-polymers was explored, with a focus on elucidating ionic contributions from electronic ones. The incorporation of an ionic conductor, Nafion®, in a bilayer structure was explored and showed an intimate interaction between the proton conductor and the electronic conductor. The potential of the multilayer structures as humidity sensors and other remarkable features found in their charge transport make these promising systems for further applications in bioelectronics.

Declaration of originality

The work presented in this thesis is original and has been executed by myself. The contents of this thesis are the result of the work conducted since my start as a PhD student and does not include work submitted to qualify for other degree or diploma in any university or research institution.

Appropriate acknowledgement of any contribution from collaborators and/or students is done in the corresponding chapters.

The copyright of this thesis rests with the author and is made available under a Creative Commons Attribution Non-Commercial No Derivatives licence. Researchers are free to copy, distribute or transmit the thesis on the condition that they attribute it, that they do not use it for commercial purposes and that they do not alter, transform or build upon it. For any reuse or redistribution, researchers must make clear to others the licence terms of this work.

Celia M Pacheco-Moreno

Acknowledgements

First I would like to express my gratitude to my supervisor Natalie, for giving me the opportunity to join her group and do research in a topic I love. The support of my supervisor Molly has been a pillar in carrying on during the hard times, and I will greatly miss the lovely times spent during group weekends. To both of them, I am thankful for the chance to follow my dream and be part of the scientific community.

I would like to also thank my collaborators: the group of Prof. Paul Meredith, and in particular Dr Bernard Mostert and Margarita Sheliakina, for their help, scientific input and absolute kindness when I visited and worked in their laboratory at the University of Queensland; Dr Olivier Dautel for synthesising the materials investigated, and along with Dr Guillaume Wantz, for the numerous fruitful scientific discussions.

I want to thank Obra Social "la Caixa" for letting me start dreaming. Their financial support to undertake my MRes and first year of my PhD was a kickstart to my adventures in science. The people working there were lovely and truly encouraging.

Next I want to thank the big Stevens group, for having been supportive and attentive during my presentations even when things were not making so much sense to them. The Polymerz subgroup, full of amazing people who have helped my research find better paths with their feedback and have also celebrated the successes along the journey. Nadav and Astrid, the inspiring scientific discussions and also F&C with you were wonderful. I already miss you guys.

The Stingelin group has become almost a family after so many meals, coffees and laughs shared. I could have never imagined a more loving, caring and fun group. You have been able to bring perspective when the stress of non-working experiments felt overwhelming, or the load of work became too large, or I made unreasonably high demands of myself in the name of research. Perspective has kept me sane and happy, and I thank you for sharing teas, coffees, beers and words to make this happen.

Some people will need to be named here, because these three years have been greatly shaped by their presence in my life. George, we walked hand-by-hand from the beginning and there are too many memorable experiences to fill in the few lines I have for you. The Spanish Velorucion will miss you very much when you go on your new adventures. Rama, also known as "little",

who's taught me from how to make tea to creating the most fun portfolio of random pictures in College together, I have had the best times with you in London. I love you two so much! Irene, Alberto and the long list of Italians, having you around has made this place feel almost like home, always full of good food, wine, coffee and the most wonderful people. Aperitivos will be missed much... and so will you! The Spanish crowd, Ester and Jaime, que maravilla que mi Castellano y Catalan no hayan muerto en mis tiempos londinenses! Your kindness, continuous good mood and wise adult advice were wonderful and I will always treasure the many hours spent talking about food! It cannot happen again in such an extent, I can assure you! Jasvir and Jorge, the teas and hugs shared made so many of my days, I am so lucky to have such great people in my life. The rest of my CDT cohort, thanks for the good times shared, you were such a lovely team. I also want to thank my friends Mercedes and Aida, who shared so many times with me, having fun together but also being there during the times of less happy Celia.

Special thanks to my wonderful MSc student Murielle Schreck, who has contributed so positively advancing the science of the bioelectronics team; her outstanding work and friendship made my last few months of research more fun and interesting.

The support that Neil has given be during the last year has been determining to the success of writing this thesis. Thanks for believing in me and being continuously encouraging!

I cannot thank enough the support and help from my lovely Robert, who has also been the best proof-reader ever. You have been a star during this long writing process. I came out in one happy piece and I am already looking forward to new adventures.

The list of friends who have given me support and love from the distance is real long. Friends from Barcelona, you have been a source of inspiration ever since I met you. I also want to thank my friends from Valencia, especially J.A, Cris and Carmina, who with I started shaping my formation and ambitions in science. I miss you a lot. My friends from back home, "gent del poble", you are far away but I know you are also there for me, especially Marisa and Maria, you wonderful ladies!

Finally, but certainly not least, I want to thank my family for being so supportive and loving in every single step and decision I've taken in my life. Knowing that you are there, unconditionally loving me, makes me a stronger and more courageous person to pursue my dreams. You have

taught me that falling is also part of life and that I should not feel ashamed of it. During my times as a PhD student, this has kept me afloat and with a smile in my face. I am lucky to be saying thanks to you all today.

I would like to acknowledge the various grants/funding bodies that generously contributed to funding my PhD research: EPSRC Centre for Doctoral Training in Plastic Electronic Materials (code: EP/L016702/1), EPSRC Centre for Innovative Manufacturing in Large Area Electronics (code: EP/K03099X/1), Heterointerface control of organic semiconductor devices (code: EP/G060738/1) and EPSRC Impact Acceleration Grant (code: EP/K503733/1). I moreover acknowledge support via projects funded by KAUST through a Global Collaborative Research Academic Excellence Alliance (AEA) grant as well as a Competitive Research grant (CRG-1-2012-THO-015-IMP).

Dedication

To Robert for his love, support and patience.

Abbreviations

a.u.	-	arbitrary units
AFM	-	atomic force microscope
Ag/AgCl	-	silver/silver chloride redox couple
Bu_4NPF_6	-	tetrabutylammonium hexafluorophosphate
$CHCl_3$	-	chloroform
CV	-	cyclic voltammetry
DC	-	direct current
DI	-	deionised
DMSO	-	dimethyl sulfoxide
DSC	-	differential scanning calorimetry
EC	-	electrochromic
EO	-	extent of oxidation
F_4TCNQ	-	7,7,8,8-tetracyano-2,3,5,6-tetrafluoroquinodimethane
GOPS	-	3-glycidoxypropyltrimethoxysilane
GS	-	good solvent
HOMO	-	highest occupied molecular orbital
I-V	-	current - voltage
ITO	-	indium tin oxide
LEC	-	light-emitting electrochemical cell
LUMO	-	lowest occupied molecular orbital
M_w	-	mass-average molecular weight

MO	-	molecular orbital
MoOx	-	molybdenum oxide
NIR	-	near infrared
OECT	-	organic electrochemical transistor
OLED	-	organic light emitting diode
OPV	-	organic photovoltaic
OSC	-	organic semiconductor
P3HT	-	poly(3-hexylthiophene)
PANI	-	poly(aniline)
PDMS	-	poly(dimethylsiloxane)
PEDOT	-	poly(3,4-ethylenedioxythiophene)
PEG	-	poly(ethylene glycol)
PMMA	-	poly(methyl methacrylate)
Ppy	-	poly(pyrrole)
PSS	-	poly(styrene sulfonate)
PVA	-	poly(vinyl alcohol)
PVP	-	poly(vinyl pyrrolidone)
RR	-	regio-regular
RT	-	room temperature
SCE	-	saturated calomel electrode
SCLC	-	space-charge limited current
SD	-	standard deviation
SMU	-	source-measure unit

SNR	-	signal-to-noise ratio
TFT	-	thin film transistor
THF	-	tetrahydrofuran
TOS	-	toluene sulfonate

Contents

Abstract **i**

Declaration of originality **ii**

Acknowledgements **v**

Abbreviations **x**

1 Introduction **1**

1.1 Brief history and outlook of bioelectronics 2

1.2 Organic electronics 5

1.2.1 Charge transport in conjugated systems 5

1.2.2 Doping conjugated polymers 6

1.3 Iontronics: mixed transport platforms 9

1.3.1 Organic Electrochemical Transistors (OECTs) 9

1.3.2 Other iontronics applications 11

1.4 Mixed ionic/electronic transport in polymers 13

1.5 Scope of the thesis 16

1.6 Publications 17

2 Experimental **19**

2.1 Thin film preparation 20

2.2 UV-Vis spectroscopy 22

2.3 Differential Scanning Calorimetry (DSC) 23

3 Ion-to-electron transducing materials: insights on molecular design **25**

3.1 Introduction 26

3.2 Materials and methods 28

3.2.1 Steady-state charge transport measurements 29

3.2.2 Contact angle 29

3.2.3 Cyclic voltammetry 30

3.2.4 Real-time electroactivity: assessing ionic transport 30

3.3 Results and discussion 37

3.3.1 Thiophene derivatives bearing -OH moiety: thin-film solid-state and polarity 37

3.3.2 Electronic transport 39

3.3.3 Ionic transport: an optical assessment 42

3.3.4 Influence of alkyl chain length 52

3.3.5 Benchmarking with PEDOT:PSS 55

3.4 Conclusions 57

4 Semiconductor/insulator blends as mixed (electronic/ionic) conductors **59**

4.1 Introduction 60

4.2 Materials and methods 62

4.2.1 Blends containing MMAcoMAPC1 62

4.2.2 P3HT(C6OH)$_{50\%}$:PVA blends - solvent choice 63

4.2.3 Sample preparation for DSC 64

4.2.4 Sample preparation for contact angle of top/bottom surfaces 64

4.2.5 Real-time electroactivity: advanced data handling 65

4.3 Results and discussion 67

4.3.1 PVA blends: solid state structure 67

4.3.2 Electronic transport 76

4.3.3 Ionic transport 77

4.3.4 A relation between aggregation and ionic transport 82

4.3.5 Influence of ion size on ionic transport 87

4.3.6 Blends with other polar insulators 91

4.4 Conclusions 94

5 Charge transport properties of polymer thin films under controlled hydration 95

5.1 Introduction 96

5.2 Materials and methods 98

5.2.1 Van der Pauw configuration: sample preparation 99

5.2.2 Van der Pauw configuration: tests and data handling 102

5.3 Results and discussion 105

5.3.1 Thiophene derivatives with -OH moieties: transport vs. hydration 105

5.3.2 Influence of metal as electrode material 111

5.3.3 Proton/Electron bilayer conductors 115

5.4 Conclusions 122

Summary of thesis achievements **124**

Bibliography **127**

Appendices **142**

A Electrochromic testing **142**

List of Tables

3.1 Mobility, field dependence coefficient and hole concentration of polythiophene polymers 40

3.2 Saturating relative absorbance of thiophene derivatives over 10 bias runs 50

4.1 Summary of decay rates of P3HT(C6OH)$_{50\%}$, processed from THF and THF:DMSO, and P3HT(C6OH)$_{50\%}$:PVA blend. 85

5.1 Oxidation and reduction peak voltages of P3HT(C6OH)$_{50\%}$ at 22 mbar H_2O vapour pressure using *Al* electrodes. 114

List of Figures

1.1 Illustration of torpedo ray by John Walsh 2

1.2 Schematics of an OECT and its typical time response 10

1.3 Schematics of an inorganic (Si) and an organic semiconductor (PEDOT:PSS). . 13

1.4 Schematic of a multifunctional biomaterial. 14

2.1 Sketch of a wire-bar coater 20

2.2 Typical DSC thermogram 23

3.1 Chemical structures of polymers: P3HT, P3HT(C6OH)$_{10\%}$, P3HT(C6OH)$_{20\%}$ P3HT(C6OH)$_{50\%}$ and P3HT(C11OH)$_{50\%}$ 28

3.2 Schematic of electrochromic setup 31

3.3 Sketch of absorbance spectra during oxidation and time dependency 32

3.4 Exponential decay models 34

3.5 Exponential decay model for relative absorbance case 35

3.6 UV-Vis spectra of polymers from Fig. 3.1 37

3.7 Water contact angle of polymers from Fig. 3.1 38

3.8 Steady-state current density vs. voltage curves of polymers **1** - **4** from Fig. 3.1 . 39

3.9 Cyclic voltammograms of polymers **1** - **5** in liquid and thin film form 43

3.10 Real-time absorbance spectra of thin films during applied bias of polymers **1** - **4** from Fig. 3.1 44

3.11 Normalised real-time absorbance spectra of a thin film of **4** from Fig. 3.1 and graph of its time dependency 45

3.12 Relative absorbance spectra at 550 nm of thin films during applied bias of polymers **1** - **4** from Fig. 3.1 46

3.13 Calculation of polythiophene derivatives' stability over 10 bias runs 49

3.14 Relative absorbance spectra at 550 nm of thin films during 10^{th} applied bias run of polymers **1** - **4** from Fig. 3.1 51

3.15 Relative absorbance spectra at 550 nm of thin films during applied bias of polymers **4** - **5** from Fig. 3.1 52

3.16 Real-time absorbance spectra of thin films during applied bias of polymers **4** and PEDOT:PSS 55

3.17 Relative absorbance spectra at 550 nm of thin films during applied bias of PEDOT:PSS 56

4.1 Chemical structures of polymers P3HT(C6OH)$_{50\%}$, PVA and MMAcoMAPC1 . 62

4.2 Schematic of polymer thin films peeled off using a PDMS stamp 64

4.3 Image of P3HT(C6OH)$_{50\%}$ and PVA neat solutions at RT and 58 °C 67

4.4 Optical micrographs of an encapsulated solution of P3HT(C6OH)$_{50\%}$:PVA (50:50 wt%) blend in THF:DMSO 2:1 v/v % at different temperatures 68

4.5 Differential scanning calorimetry (DSC) of P3HT(C6OH)$_{50\%}$:PVA blends of varying ratios. 69

4.6 Melting enthalpies and temperatures of P3HT(C6OH)$_{50\%}$ and PVA for different blend ratios as measured by DSC. 70

4.7 Polymer blend thin films on glass and peeled off using a PDMS stamp 71

4.8 Water contact angle on the top and bottom surface of P3HT(C6OH)$_{50\%}$:PVA blend films 72

4.9 Atomic force microscope (AFM) images in air and fluid of P3HT(C6OH)$_{50\%}$ and P3HT(C6OH)$_{50\%}$:PVA blend thin films 73

4.10 Film thickness of P3HT(C6OH)$_{50\%}$:PVA blends after 24 h immersed in electrolyte 74

4.11 Conductivity of P3HT(C6OH)$_{50\%}$:PVA blends measured by 4-point probe 76

4.12 Real-time absorbance spectra of thin films during applied bias of P3HT(C6OH)$_{50\%}$ and P3HT(C6OH)$_{50\%}$:PVA (50:50 wt%) blend 77

4.13 Relative absorbance spectra at 550 nm during applied bias of P3HT(C6OH)$_{50\%}$ and P3HT(C6OH)$_{50\%}$:PVA (50:50 wt%) blend 78

4.14 Characteristic oxidation time response, t_{80}, of P3HT(C6OH)$_{50\%}$:PVA blends . . 79

4.15 Semi-logarithmic relative absorbance spectra at 550 nm of thin films during applied bias of P3HT(C6OH)$_{50\%}$ and P3HT(C6OH)$_{50\%}$:PVA (50:50 wt%) blend . 80

4.16 UV-Vis spectra of P3HT(C6OH)$_{50\%}$ thin film processed from THF and THF:DMSO 2:1 v/v% 82

4.17 Real-time and relative absorbance spectra at 550 nm of thin films during applied bias of P3HT(C6OH)$_{50\%}$ processed from THF and THF:DMSO 2:1 v/v% 83

4.18 Semi-logarithmic relative absorbance spectra at 550 nm of thin films during applied bias of P3HT(C6OH)$_{50\%}$ processed from THF and THF:DMSO 2:1 v/v% 84

4.19 Differential scanning calorimetry (DSC) of P3HT(C6OH)$_{50\%}$ processed from THF and THF:DMSO 2:1 v/v%. 86

4.20 Chemical structures of salts used to prepare aqueous electrolytes: NaCl, KCl and NaTOS 87

4.21 Relative absorbance spectra at 550 nm during applied bias of P3HT(C6OH)$_{50\%}$ and P3HT(C6OH)$_{50\%}$:PVA (50:50 wt%) blend using NaCl and KCl electrolytes . 88

4.22 Characteristic oxidation time response, t_{80}, of P3HT(C6OH)$_{50\%}$:PVA blends using KCl electrolyte 89

4.23 Relative absorbance spectra at 550 nm and characteristic oxidation time response, t_{80}, during applied bias of P3HT(C6OH)$_{50\%}$ and P3HT(C6OH)$_{50\%}$:PVA (50:50 wt%) blend using NaTOS electrolytes 90

4.24 Conductivity of P3HT(C6OH)$_{50\%}$:MMAcoMAPC1 blends measured by 2-point . 91

4.25 Optical micrographs of thin films of P3HT(C6OH)$_{10\%}$ and P3HT(C6OH)$_{50\%}$ and their corresponding 50 wt% blend with MMAcoMAPC1. 92

4.26 Relative absorbance spectra at 550 nm and characteristic oxidation time response, t_{80}, during applied bias of P3HT(C6OH)$_{50\%}$:MMAcoMAPC1 blends. . . 93

5.1 Chemical structures of polymers: P3HT, P3HT(C6OH)$_{10\%}$, P3HT(C6OH)$_{20\%}$, P3HT(C6OH)$_{50\%}$ and Nafion® 98

5.2 Shadow mask and sketch of a sample prepared for van der Pauw tests. 99

5.3 Example of a sample prepared for van der Pauw tests. 100

5.4 Picture of the experimental setup to perform hydration-controlled van der Pauw tests. 101

5.5 Sketch of the eight van der Pauw configurations. 103

5.6 I-V curves and conductivity of P3HT vs. H_2O vapour pressure measured by van der Pauw method. 105

5.7 I-V curves and conductivity of P3HT(C6OH)$_{10\%}$ vs. H_2O vapour pressure measured by van der Pauw method. 107

5.8 I-V curves and conductivity of P3HT(C6OH)$_{20\%}$ vs. H_2O vapour pressure measured by van der Pauw method. 108

5.9 I-V curves and conductivity of P3HT(C6OH)$_{50\%}$ vs. H_2O vapour pressure measured by van der Pauw method. 109

5.10 Conductivity of P3HT and derivatives vs. H_2O vapour pressure measured by van der Pauw method. 110

5.11 Conductivity of P3HT derivatives when using *Al* and *Au* electrodes vs. H_2O vapour pressure measured by van der Pauw method. 111

5.12 Comparison of I-V curves of materials **2**, **3** and **4**, using *Al* and *Au* electrodes, vs. H_2O vapour pressure measured by van der Pauw method. 112

5.13 I-V curves of material **4** at 22 mbar H_2O vapour pressure using *Al* electrodes. All van der Pauw configurations shown for two samples. 114

5.14 I-V curves and conductivity of P3HT and Nafion® vs. H_2O vapour pressure measured by van der Pauw method. 115

5.15 I-V curves and conductivity of P3HT/Nafion® and Nafion®/P3HT bilayers vs. H_2O vapour pressure measured by van der Pauw method. 117

5.16 I-V curves of Nafion®/P3HT (top) bilayers at varying voltage-sweep rates at 18 mbar H_2O vapour pressure measured by van der Pauw method. 118

5.17 Conductivity of P3HT, Nafion® and their bilayers vs. H_2O vapour pressure measured by van der Pauw method. 120

5.18 UV-Vis absorbance of P3HT and Nafion®/P3HT (top) bilayers. 120

A.1 Material **2**: real-time absorbance spectra during oxidation, normalised spectra and relative absorbance at 550 nm vs. time 143

A.2 Material **3**: real-time absorbance spectra during oxidation, normalised spectra and relative absorbance at 550 nm vs. time 144

A.3 Material **4**: real-time absorbance spectra during oxidation, normalised spectra and relative absorbance at 550 nm vs. time 145

A.4 Material **5**: real-time absorbance spectra during oxidation, normalised spectra and relative absorbance at 550 nm vs. time 146

Chapter 1

Introduction

1.1 Brief history and outlook of bioelectronics

The birth of electricity, or "current" electricity, has been historically linked to the experiments of Luigi Galvani during the late eighteenth century.[1] Galvani's research was stimulated by previous studies conducted by John Walsh (1776) on electric fish, particularly on proving the electric character of the shocks observed in torpedo rays.[2] Figure 1.1 shows the illustration presented with his findings in his letter to the Royal Society. Taking inspiration from nature for new theories about the flow of charges, which at the time was thought of as "fluid animal electricity", has not stopped but only been transformed into a new ambition to understand the electronics involved in biology and medicine.

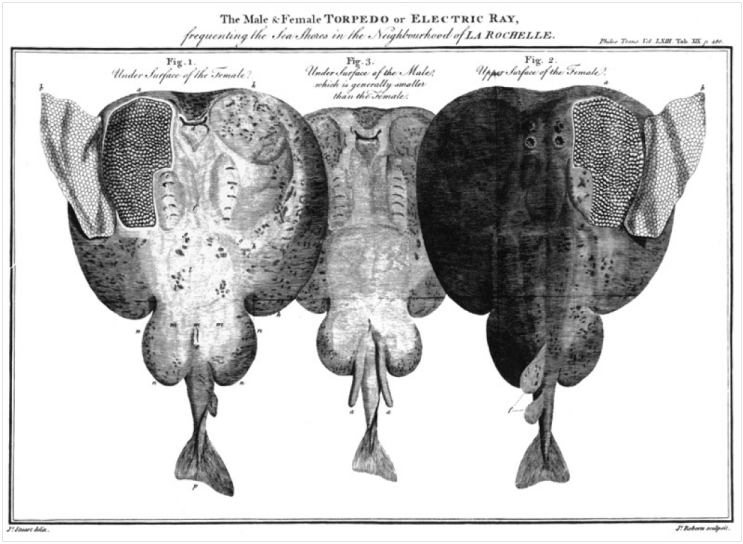


Figure 1.1: Illustration of a male and female torpedo ray by John Walsh from his letter.[2]

In a broad context, bioelectronics can be understood as the interface of electronics with biology. The wealth of perspectives that the scientific community has taken on these interactions is enormous. It deals with sensing applications for the detection of relevant biomolecules in biology and medicine, but also focuses on implementing biological systems/components in electronic applications, for example using DNA or proteins in charge transport applications.[3,4] The direct interfacing of biological systems with electronic devices has also been demonstrated in brain-machine interfacing, with reports aiming to further the understanding of brain neural networks or enabling the interaction with prosthetic devices for the restoration of body functions.[5,6,7]

The success of some of these concepts can be seen in a variety of everyday applications implemented in healthcare; around 500,000 pacemakers were implanted in Europe alone in 2013,[8] and along with defibrillators, save millions of lives around the globe every year; the cochlear implant, experimentally implanted first in 1957,[9] has allowed hearing loss recovery in children and adults with around 100,000 implantees recorded in Europe in 2011;[10] deep-brain stimulation has been applied to alleviate Parkinson's disease symptoms, such as tremor as well as depression and pain;[11,12] glucose sensors have aided diabetic patients for over three decades in monitoring their blood glucose, with point-of-care devices becoming more sophisticated and providing continuous control.[13] Recent advances evidence a blooming interest in the integration of bioelectronics also in the kingdom Plantae, introducing the new e-Plant concept, "possibly serving as a complement to existing molecular genetic techniques used in plant science and agriculture".[14]

In the field of medicine a newly coined term, "electroceuticals", has also appeared, which envisions a new era moving away from molecular medicines.[15] Bioelectronics concepts seem to have opened frontiers in the way people will envision health care, with science proposing "closed-loop" applications, meaning all processes from diagnosis to monitoring and treatment would be coupled in possibly even wearable healthcare devices. The biggest challenge reported by Kristoffer[15] was probably the multidisciplinary character of this discipline and the need for bridging understanding across many fields of research. A snapshot of the complexity of the concept as described in his own words is as follows: "to develop treatment devices, bioengineers designing biocompatible interfaces will need to collaborate with electrical engineers to develop microchips for real-time signal processing; with nanotechnologists to create energy sources; and with neurosurgeons to ensure that these designs can be implanted and connected". This encompasses only a small portion of the design of new diagnosis, monitoring and treatment systems.

The integration of modern technologies (i.e. semiconductor electronic devices, the conductivity of which can be modulated) with biology can lead to breakthroughs in many fields, such as medicine. It is at this stage that the engineering of new materials, and the understanding of the physics of the transport processes that take place in materials of interest, plays a pivotal

role.

Using new technologies to miniaturise devices and target specific cells, or groups of cells, has been one of the contributions of semiconducting devices to bioelectronics.[16] Specific targeting can be crucial for improving certain treatments where the lack of localised delivery of electrical impulses can be detrimental. For example, deep-brain stimulation can lead to emotional and cognitive side effects in treated Parkinson patients.[12]

The field of organic electronics has provided further benefit to the new realms of bioelectronic interfaces and applications, since (semi-)conducting polymers offer a unique combination of semiconductor properties (charge transport) and those of typical polymers (ease of processing, synthesis, flexibility, etc.).[17] Although their flexibility seems to be one the most attractive attributes for bioelectronics, due to improved matching to the mechanical properties of tissue, it is really their ability to withstand ionic bulk currents that sets them apart from typical inorganic semiconductors.[18,19] Since biological systems strongly rely on ion fluxes for the regulation of cellular processes, conducting polymers appear to be excellent candidate materials to bridge the electronic and the biological worlds.[3,20]

Their success can be seen in the variety of applications that have already been achieved in biosensing,[21,22] tissue engineering,[23,24,25,26] drug delivery devices,[27,28] bio-actuators,[29,30] and neural probes.[7,31,32]

1.2 Organic electronics

1.2.1 Charge transport in conjugated systems

Organic materials are constructed around a backbone of carbon atoms, each containing four valence electrons at the atomic orbitals 2s, $2p_x$, $2p_y$ and $2p_z$. When two or more carbons combine forming a molecule and each carbon then attaches to three groups in total, sp^2-hybridisation takes place to form molecular orbitals (MOs). During a hybridisation process, a linear combination of atomic orbitals form a set of MOs. In sp^2-hybridisation, three of the orbitals, namely 2s, $2p_x$ and $2p_y$, combine to form three co-planar sp^2 MOs, arranged in the plane at 120° from each other, which are involved in forming rigid σ-bonds between carbons. The semiconductivity of both polymers and small molecules arises from the delocalisation of electrons that occupy the remaining p_z orbital, which does not hybridise and is oriented perpendicular to the polymer backbone.[33]

The alignment of the p_z orbitals along the backbone allows the overlap of their wavefunctions, forming the so-called π-bonds that extend over adjacent carbon atoms. The alternation of single (σ) and double ($\sigma + \pi$) bonds is referred to as conjugation and leads to delocalised π-electrons along the conjugation length of the molecule, a concept in parallel to band theory of inorganic semiconductors. Going one step further in forming MOs, from the linear combination of p_z atomic orbitals from N atoms, the molecule's π-electrons energy levels are split in a set of $N/2$ π-bonding states and a set of $N/2$ higher energy π^*-antibonding states. In an unexcited neutral molecule, the N electrons will fully occupy the $N/2$ lower energy states (π), each containing two anti-parallel spin electrons, whereas the upper energy band (π^*) is unoccupied.[33]

When increasing the number of contributing atoms to N= ∞ the energy band-gap E_g between the Highest Occupied Molecular Orbital (HOMO) and the Lowest Occupied Molecular Orbital (LUMO) would intuitively reduce to the point where a continuous band of π and π^* energy levels is formed in the fashion of a one-dimensional metal. However, this lattice structure is energetically unstable and the Peierls distortion, which was described as a shift of the atoms locations to their neighbouring atom, effectively looking like a dimerisation with periodicity $2a$

(twice that of the original lattice, a), predicts electrons to be at a lower energy under these conditions, than in the perfect crystal.[34] This new arrangement of the atoms results in the split between the molecular π and π^* bands, with an energy band-gap E_g ranging between 1 and 5 eV. Considering the band structure described, the conjugated molecules hence behave as semiconductors in which the continuous π states act as a valence band and the π^* states act as a conduction band to which electrons can be promoted following the absorption of light.[33,35]

Charge transport in conjugated materials further depends on how the delocalised electrons move from molecule to molecule, since these are only weakly bonded rather than belonging to a fully ordered crystal lattice. The hopping rate of carriers from one to another is determined by the overlap of their molecular wave-functions, meaning more ordered (crystalline) materials in their solid-state which generally have greater $\pi - \pi$ overlap would hence generally have better transport.[36]

The contributions of short-range and long-range order on charge transport are complex and still being scrutinised by the research community. Using a broad range of materials with different levels of order, a recent work by Noriega et al. evidenced the importance of having interconnected short-range aggregates to achieve high charge mobility materials.[37] As they described, "these aggregates can act as efficient interchain hopping sites to promote charge transport", meaning semi-crystalline polymers can offer unique transport properties, tuneable through the various levels of order that can be achieved.

1.2.2 Doping conjugated polymers

The underlying principle of doping organic semiconductors is close to that of doping for their inorganic counterparts in that mobile carriers are generated by the addition of an electron donor/acceptor. Chemically synthesised organic semiconductors are in general nominally undoped materials.[38]

While atom substitution takes place during doping of inorganic semiconductors, which is generally done by ion implantation, p-dopants are added to organic semiconductors and find location

in the interstices of the weakly bonded molecules (polymer chains).[39,40] The generation of free carriers in organics is complex and is coupled to lattice deformation/molecular rearrangements. The combination of the generated charge and modifications in the lattice dimerisation pattern are called polarons.[41] The increase in the number of charges upon doping broadens the polaronic band within the band-gap. Although it is found that the density of dopants relates to increasingly larger conductivities, no direct theoretical relation has so far been found.[40] Since the creation of polarons is linked to the creation of new energetic states within the band-gap, the light absorbing properties of the polymers also change when doped. This is very evident in the case of polyaniline (PANI) which changes colour from white/transparent in the fully reduced state, to light/dark green in the partial/fully oxidised forms.[42]

A multitude of dopants has been reported in the literature; inorganic species such as oxidising gases (I_2, Br_2), small atoms (Cs, Li) or acids (HCl); polyelectrolytes (PSS); and larger aromatic molecules, referred to as molecular dopants (F_4TCNQ).[43,44,45,46] Amongst these, molecular dopants are considered the most suitable due to their better stability and also the capability to control their energy levels, and hence closely match them to specific semiconducting systems. However, despite their preference, the volatility and diffusivity within the host material of most molecular dopants has limited their success in long-term stable applications.[47] It is therefore not surprising that they have not been employed in bioelectronics, since they also tend to be highly toxic.

All of the above dopants are *p*-dopants, meaning mobile holes are generated by their addition to organic semiconductors. Achieving *n*-doping in organic materials has proved challenging due to the energy level of the involved orbitals, which renders doping highly unstable in ambient conditions.[48]

Dopants can also be added during synthesis, for example when polymers are electropolymerised.[49] In this case, a metal electrode is immersed in a solution which contains the monomers of interest and the dopant molecule/macromolecule. When a current (or voltage) is driven in the electrochemical cell, the polymer is formed in the oxidised state, in which the dopant acts as a counter-ion embedded in the polymer matrix which provides charge neutrality. The bias

choices highly determine the microstructure of the electropolymerised film. Electropolymerisation has played a key role in the development of conducting polymers and has been particularly present in bioelectronics, for instance in broadly used polymers such as polypyrrole (Ppy) or poly(3,4-ethylenedioxythiophene) (PEDOT).[7,26,50,51,52]

Electrochemical processes can also be involved in the doping/dedoping of conducting polymers, in which case a source of ions (a liquid electrolyte or a gel) in contact with the organic semiconductor, generally cast as a film, is involved in providing the counter-ions required to complete the redox transformation.[53] The electrochemical doping of polymers is complex, involving a multitude of processes; charge transfer between the electrolyte/semiconductor and the semiconductor/electrode substrate, ionic diffusion in the electrolyte and within the bulk of the semiconductor, volume changes from the swelling/shrinkage of the semiconductor, and changes in conductivity due to doping/dedoping.[18] The inclusion of ions in the polymer to neutralise the generated charge, as well as the potential flux of solvent during the redox process, requires further structural reorganisations in order to accommodate them in space. The increase in conductivity during electrochemical doping is the principle of operation of Organic Electrochemical Transistors (OECTs), which have been highly useful devices for furthering the understanding of the interplay between ionic and electronic species in such redox processes.[22]

The relevance of electrochemical doping/dedoping to the study of ionic transport in polymers will be drawn upon in the course of this thesis.

1.3 Iontronics: mixed transport platforms

While electronics deals with the flux of electrons and holes, iontronics is the field related to the modulation of ions as well as those charge carriers.[18] Although the involvement of ions in charge transport processes and devices made of polymers dates back many decades, the establishment of iontronics as a research field in its own right is very recent.[54] This is mostly due to its multidisciplinary character, involving a broad variety of applications and researchers converging from many other fields.

As already mentioned in Section 1.2.2, electrochemical processes have been highly relevant in the development of the organic electronics field. They have been used for synthesis of materials, in doping to enhance charge transport and also in analytical methods to understand material properties such as redox transitions or ionic transport.

During electrochemical processes, multiple properties of materials can be modulated in a controlled manner, such as conductivity, colour, intensity of fluorescence and volume. Applying these principles of modulation has allowed the use of organic semiconductors as active materials in various device structures with applications in electrochromism, artificial muscles, light-emitting electrochemical cells and biosensors.[18]

Lately, purely ionic integrated circuits, referred to in literature as chemical circuits, have been realised.[55] Even when device operating times are in the order of seconds, this is a significant milestone in the field of iontronics which could lead to the controlled and localised release of chemicals in biological systems.

1.3.1 Organic Electrochemical Transistors (OECTs)

Organic Electrochemical Transistors (OECTs) have been used as efficient ion-to-electron converters.[56] During their operation, the organic active layer is in contact with an electrolyte, generally water-based, and electrochemical doping/dedoping of the organic semiconductor at the channel acts as the transducing element of the device. In the most common OECTs, based

on the dedoping of PEDOT:PSS, the transduction mechanism takes place as the injection of cations from the electrolyte compensates the pendant groups of the PSS, which reduces the effective density of holes in the material and hence decreases its conductivity.[57] In short, the flux of ions modulates that of electrons. This is why OECTs act as ion-to-electron converters.

Figure 1.2 (left) shows a sketch of a typical OECT device structure, which has three terminals. By applying a gate voltage (V_G), the gate modulates the conductivity state of the organic semiconductor by electrochemically doping/dedoping it, which is possible due to the electrolyte bridging them. The source electrode is grounded and the potential difference across source-drain electrodes (V_D) drives a current (I_D) with an intensity dependent on the conductivity of the channel.

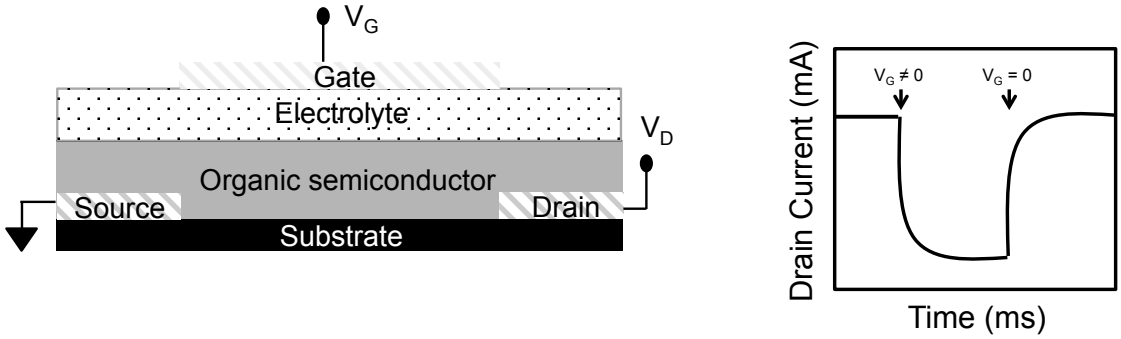


Figure 1.2: Organic ElectroChemical Transistor (OECT). **Left:** Sketch of a device structure. **Right:** Typical time response obtained when a step voltage is applied at the gate V_G and the drain current (I_D) is monitored overtime.

One important characteristic which is general in all transistors, including OECTs, is their signal amplifying capabilities. This is particularly important in sensing applications, since it determines the sensitivity of the sensor. In OECTs, the transconductance (g_m) provides a measure of such amplification and it is calculated as $g_m = \Delta I_D / \Delta V_G$. Large transconductances have been found in OECTs, which has been attributed to the doping/dedoping taking place in the entire volume of the semiconducting material.[58] Time response of OECTs is also relevant in order to operate the devices at the appropriate bandwidth. Figure 1.2 (right) shows a typical response, as measured by the changes of I_D to an applied V_G over time.

From the birth of OECTs in 1984,[59] the miniaturisation and development of fully conformable

devices has made them fit a variety of applications even *in vivo*.[32] Functionalisation of the channel is also possible, allowing the development of platforms with more specific interactions between the biological system and device, as well as improving coupling between the two.[20,60]

As mentioned earlier in this section, PEDOT:PSS is an OECT channel material of paramount importance. Since it is a highly *p*-doped polymer, OECTs which employ PEDOT:PSS as the active layer display large current I_D in the absence of an applied bias V_G. When a positive bias V_G is applied, the free holes are depleted as the polymer becomes dedoped and hence the current I_D drops dramatically. This mode of operation is called depletion, due to the decreasing number of free charge carriers in the channel upon operation. Only recently, accumulation mode OECTs have been reported in the literature employing a polythiophene-based conjugated polyelectrolyte.[61] Accumulation OECTs are of great interest since their initial OFF state provides a low signal background, enhancing signal detection as well as reducing power consumption of the device during operation, since it is in the OFF state unless a signal is detected. The use of intrinsic semiconductors in ion-to-electron transduction is a topic of interest in this thesis.

1.3.2 Other iontronics applications

Organic electronic materials have been most intensely studied for the development of electronics applications such as organic photovoltaics (OPVs), organic light emitting diodes (LEDs) or thin film transistors (TFTs).[62,63]

For some of these applications one can find an ionic version in the literature. In Section 1.3.1 the OECTs presented, being a transistor where transport is modulated by ions fluxes, attained large signal modulation due to the flux occurring in the full volume of the channel.

The Light-Emitting Electrochemical Cell (LEC) is the ionic counterpart of the OLED.[64,65] LECs contain an electroluminescent polymer embedded in an electrolyte in which ions have also been dissolved. The mobile ions separate towards opposite electrodes under an applied bias and form an electrical double layer (EDL) at the electrodes, which is responsible for allowing the devices to operate at low voltages and for their electroluminescence being largely independent

of film thickness. Although the process leading to light-emission is still under debate, LECs promise novel science in understanding mechanisms related to their mixed transport as well as applications in large-area low-cost fabrication.[54]

Other sensor architectures have taken inspiration from what was probably the first organic bioelectronics sensor, the glucose sensor reported by Foulds et al. in the 1980s which used Ppy as active material.[66] The entrapment or biofunctionalisation of bio-recognition molecules in the bulk of polymers has allowed successful biosensors for example for enzyme or DNA detection.[23,67,68]

Volume changes in conducting polymers during electrochemical oxidation/reduction have been exploited for the design of bioactuators operating at low voltages.[53,69] During doping/dedoping of a conducting polymer the insertion of counter-ions in the volume of the material causes its bulk expansion, which can be used to achieve linear strain, bending motion or other actuation depending on the device architecture. More intricate designs have realised micro-robots with potential uses in manipulating micron-size objects in aqueous environments.[70] Although Ppy is the most used polymer in actuation, PANI and polythiophene derivatives are also found in the literature.[71]

One last remarkable application of conducting polymers is in electrochromic (EC) displays. Distribution of information in flexible light-weight displays is a desirable technology that makes conducting polymers most attractive. As mentioned in Section 1.2.2, electrochemical doping/dedoping generates new energy states in the band-gap of the organic semiconductor, which affects its absorption characteristics and hence changes the colour of the polymer in the visible spectra. EC displays need to have the active layer in contact with an electrolyte, which can be a liquid, a gel or a solid electrolye. PEDOT:PSS has been exploited as an EC material due to its potential use both as active layer and supporting electrode, due to its large conductivity, and it has been successfully printed on flexible substrates such as paper.[72,73]

1.4 Mixed ionic/electronic transport in polymers

Electrical stimulus has been shown to affect cellular processes such as cell migration, orientation and differentiation, and is directly involved in the development and function of bone, muscle and nervous tissue.[74,75,76] Although application of electric fields and current pulses has shown an effect on certain experimental setups, biological systems transmit information in a dynamic fashion solely using ions as signal transmitters and regulators. A clear example where mixed ionic/electronic transport has had clear beneficial effect is the use of polymers in neural probes. The delivery of stimulation and recording of neural activity using micro-electrodes coated with a conducting polymer has shown significant improvements compared to bare metal electrodes. The ability to provide therapeutic current levels while maintaining safe voltages is related to the ability of the polymer to sustain mixed transport.[49,51,77] This is attributed partly to the more porous structure, due to weak bonding occurring between polymer chains, compared to the compact crystal lattice found in inorganic semiconductors (Figure 1.3).

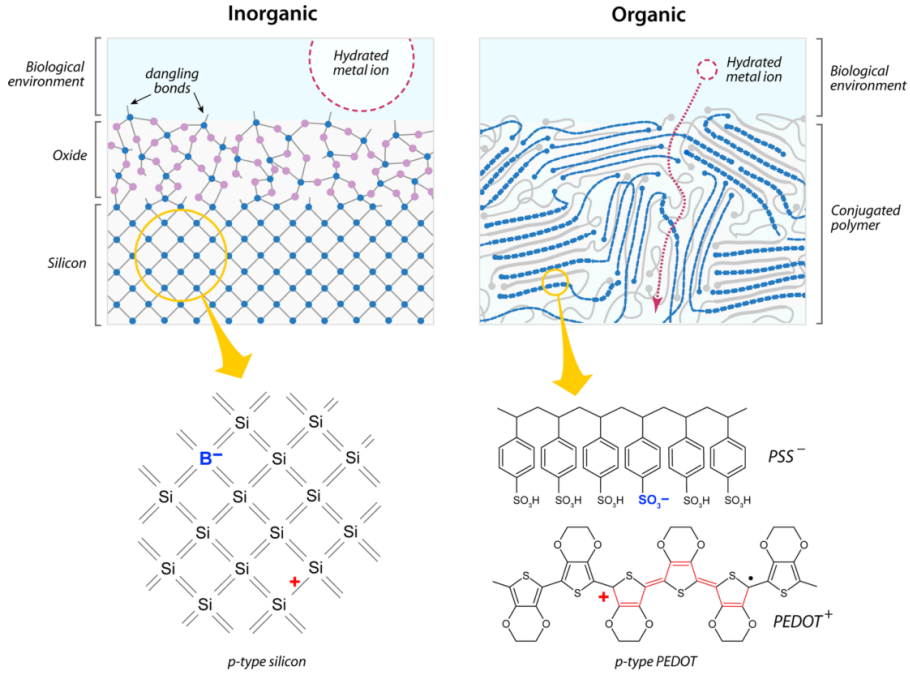


Figure 1.3: Schematics of an inorganic (Si) and an organic semiconductor (PEDOT:PSS) in contact with an electrolyte with hydrated ions (to scale). Reprinted with permission from J. Rivnay, R. M. Owens, and G. G. Malliaras, "The Rise of Organic Bioelectronics," *Chem. Mater.*, vol. 26, no. 1, pp. 679 – 685, 2014.[78] Copyright 2014 American Chemical Society.

Conducting polymers have also become attractive for use as biomaterials due to their promise to tune and deliver multifunctionality arising from the versatility in their chemical design and processing; see Figure 1.4 for a summary of some relevant functions desired in a conducting biomaterial.[79] Hence, they are excellent candidate materials to bridge the electronic and the biological worlds.

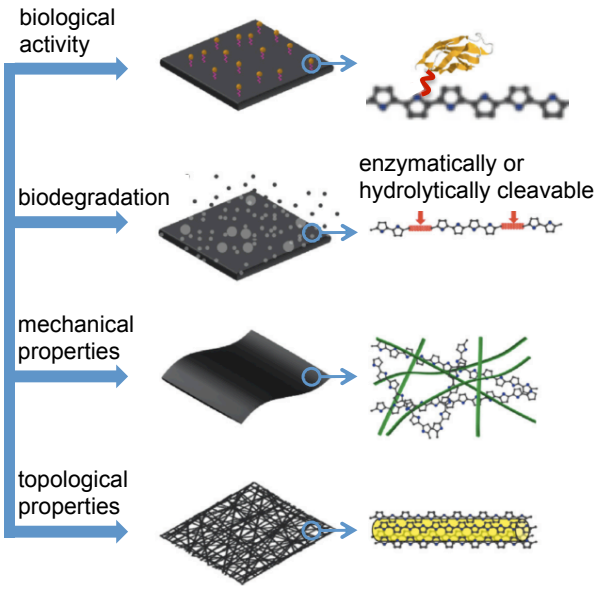


Figure 1.4: Schematic including relevant characteristics to achieve a conducting multifunctional biomaterial. Figure has been adapted and reprinting permission obtained from:
J. G. Hardy, J. Y. Lee, and C. E. Schmidt, "Biomimetic conducting polymer-based tissue scaffolds," *Curr. Opin. Biotechnol.*, vol. 24, no. 5, pp. 847 – 854, 2013.[79]

Since ionic conductivity seems to be one of the key functions of (mixed) conducting polymers, further understanding regarding the control and measurement of ion mobility is required.

The first direct measurement of ionic mobility in mixed conductors was recently measured by Stavrinidou et al. in PEDOT:PSS and PEDOT:TOS.[80,81] The setup involved the electrochemical doping/dedoping of the investigated materials in a planar electrolyte/semiconductor junction, where the moving doping/dedoping front was traced optically over time. The speed of the front movement was used to calculate the mobility of the involved ions using an analytical model. Although the model does not restrict its use to intrinsic polymers which dope during an applied voltage (accumulation mode), it is unsure whether ion injection from the electrolyte may be hindered by the initially low conductivities compared to PEDOT:PSS (used

in its highly doped state in depletion mode).

Even though the picture of the porous, highly mixed conducting PEDOT:PSS has convinced the community of the potential of conducting polymers as a whole in bioelectronics, further insight needs to be gained with regard to the ionic transport in new materials and its optimisation with respect to their electronic conductivity. Learning about the interplay of ionic and electronic transport, along with the means to manipulate both, will be of great importance for continued progress in the field.

1.5 Scope of the thesis

This thesis studies the charge transport of conducting polymers with the potential to sustain mixed ionic/electronic carriers in a variety of single and multi-component systems in order to gain understanding on design rules for new bioelectronic materials, develop facile routes to control ionic transport and learn about the influence of humidity on mixed conducting systems. Chapter 1 provides an introduction to organic bioelectronics and the broad range of applications that rely on mixed ionic/electronic transport. Chapter 2 summarises the general fabrication and characterisation methods used throughout the thesis, with specific methods for each experimental chapter described within the relevant chapters. Chapter 3 addresses the use of new model systems, based on random copolymers, as novel ion-to-electron converters using a simple opto-electrochemical characterisation method. Chapter 4 explores the blending of a polar insulator with one of the ion-to-electron signal transducers as a means to enhance ionic transport. An insight on the influence of order (at specific length-scales) on ionic transport is given. Chapter 5 explores the effect of humidity on the transport of conducting polymers and on novel multi-layer structures involving the proton conductor Nafion®.

1.6 Publications

List updated as of March, 2016.

1. Celia M Pacheco-Moreno, Guillaume Wantz, Olivier J Dautel, Molly M Stevens and Natalie Stingelin.
   "Electroactive polythiophene co-polymers for bioelectronics"
   (*To be submitted*)

2. Celia M Pacheco-Moreno, Nadav Amdursky, Olivier Dautel, Eleni Stavrinidou, Astrid Armgarth, Murielle Schreck, Molly M Stevens, Natalie Stingelin.
   "Derivative polythiophene:PVA blends towards versatile mixed transport materials"
   (*To be submitted*)

Chapter 2

Experimental

2.1 Thin film preparation

ITO substrates (70 - 100 Ω/sq, Sigma-Aldrich) of dimensions 2.5 cm x 2.5 cm were used for casting the thin films whose electrochromism was characterised, which required a conducting and transparent substrate. ITO substrates were cleaned by being sonicated in sequence with acetone and isopropanol for 10 mins each. After being blow-dried with air they were placed in an ultraviolet ozone (O_3) chamber (UVOCS®) for 15 min immediately before film deposition. A maximum lag of 20 min was allowed between O_3 treatment and film deposition to ensure the surfaces were activated.

Glass substrates were used for all other thin film characterisation (UV-Vis spectroscopy, contact angle, DSC sample preparation, AFM, film stability in water and 4-point electrical measurements, including those by the van der Pauw method) and were cleaned following equivalent steps to ITO substrates, without ultraviolet O_3 plasma treatment.

Thin films were fabricated using a temperature controlled wire-bar coater (K 101 Control Coater, Printcoat Instruments); a sketch can be seen in Figure 2.1.

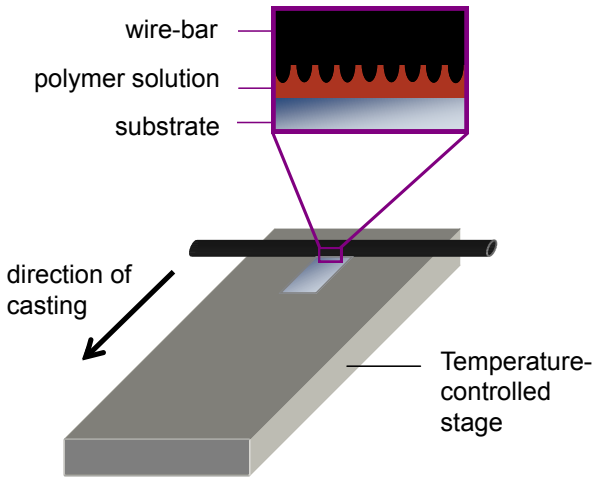


Figure 2.1: Sketch of a wire-bar coater with a temperature-controlled stage.

The wire bar coater consists of a temperature-controlled stage onto which substrates are placed, and a parallel cylindrical bar winded with wire of varying width. The closely winded wires (a close up can be seen in Figure 2.1) uptake the solution into the gaps by capillarity and greatly

determines the thickness of films when the coating is done in contact (bar is directly resting onto the substrate). The width of the wire is less relevant when films are coated leaving a bar-to-substrate gap (this is the case illustrated in Figure 2.1), in which case the coating speed and rheology of the solution play a more relevant role.

A deposition temperature of 40 °C and a speed of 5 in the coater units ($\approx$ 10 cm/s) were used. Films were coated with a number 10 bar, leaving a gap of $\approx$ 0.36 mm between the bar and the substrate. In order to attain reproducibility of the prepared films, the volume of solution used per layer was measured to be 50 μl. Pipette tips were warmed up at the hot stage before pipetting the solution, which ensured no dramatic temperature drop affected the dissolution of the polymers before drying as a thin film.

After film deposition, 2 min were allowed on the hot stage to ensure solvent evaporation. For samples prepared for electrochromic tests (Section 4.3.3 and related ones), thickness was adjusted to improve the signal-to-noise ratio (SNR). Two layers were deposited for this purpose, in which case drying times were:

- 2 min after the first layer deposition
- 4 min after the second layer deposition

No treatment was performed in between the deposition of both layers.

Similarly, samples prepared for DSC were multi-layer cast with up to five layers, in order to obtain enough material for DSC analysis.

After thin film samples were prepared, they were kept in the dark (either in a cupboard or wrapped in aluminium foil) in order to reduce the extent of degradation by photo-oxidation due to UV light.[82]

2.2 UV-Vis spectroscopy

UV-Visible (UV-Vis) spectroscopy is a technique that measures the absorbance of light of a material generally in the wavelength range 200 - 1400 nm, which covers part of the ultraviolet spectrum (UV, 200 - 400 nm), the visible spectrum (Vis, 400 - 700 nm) and the near-infrared (NIR, 700 - 1400 nm). The material can be in the form of a solution (generally very diluted) or cast as thin film on a substrate.

The absorbance is calculated based on Beer's and Lambert's laws, which establish that the absorbance is proportional to the number of absorbing molecules and that the fraction of radiation absorbed does not depend on the radiation intensity, respectively. The equation that related absorbance to the relevant parameters is:

$$A = log_{10}\frac{I_0}{I} = \alpha cL \tag{2.1}$$

where I_0 is the intensity of the incident radiation, I is the transmitted intensity, α is the absorbance coefficient (a constant to each material), or extinction coefficient in older texts, c is the concentration of attenuating species, and L is the path length. The incoming and transmitted intensity is measured for each wavelength.

The absorbance of light takes place when electrons in the valence band are promoted from the ground state to an excited state. The range of wavelengths in UV-Vis spectroscopy captures most of the $\pi \rightarrow \pi^*$ electronic transitions, and hence the technique provides information about the band structure of the studied materials. However, the absorbance of thin films is also affected by the electronic surroundings of the molecules, including the polarity of the solvent in solution spectroscopy, and the molecules' short-range order. The technique can hence provide information related to the microstructure of materials, such as molecular arrangement and ordering.

2.3 Differential Scanning Calorimetry (DSC)

Differential scanning calorimetry (DSC) is a thermal analysis technique that measures the difference in the heat flow between a sample and a reference as a function of temperature. Samples are heated/cooled at a given rate (generally in K/min) and the heat flow required to increase the temperature is compared to that for an empty aluminium pan, which is used as reference.

Changes in the heat flow are related to phase transitions and/or chemical reactions of the material at the given temperature (or generally, temperature range), providing quantitative information on such transitions. The heat difference corresponds to the amount of heat (energy) which is required in order for the material to undergo such transformation(s), while remaining at the same temperature as the reference. Heat flow can be into the sample (endothermic) or out of the sample (exothermic), and needs to be specified in the curves since axes plotting conventions change between instruments.

An example of DSC thermogram of a semi-crystalline polymer is shown in Figure 2.2.

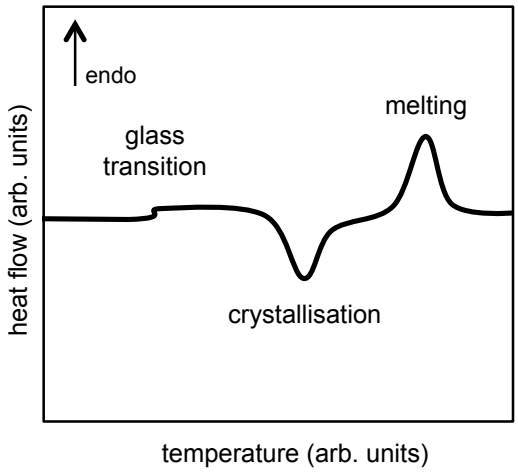


Figure 2.2: Typical DSC thermogram displaying a glass transition, melting and crystallisation of a material.

Glass transitions take place in the amorphous parts of semicrystalline polymers and correspond to a rapid change in the heat capacity when the material changes to a more "rubbery" state

from a more brittle one, or vice versa. It is observed as a step-like change in the thermogram as displayed in Figure 2.2.

Melting, or fusion, is the phase transition that occurs when a crystalline solid changes to the liquid state and it requires a large amount of supplied energy to take place, hence it appears as an endothermic peak in the thermogram. The enthalpy of melting is the heat energy required for breaking down the crystalline lattice and is given by the integral of the area of the DSC peak in conjunction with the heating rate. It is generally given as enthalpy per gram, after being normalised to the mass of the tested sample. The sharper the peak the more defined the crystal structure. Crystallisation is shown as an exothermic peak in the thermogram and depends on the cooling rate of the sample.

For the experiments performed in this thesis, heating/cooling was done at 10 °C/min under nitrogen atmosphere, over a temperature range of 35 - 270 °C. Standard aluminium crucibles were used for encapsulating the sample and as reference pan. Samples ranged in mass from 1.5 - 3 mg.

Chapter 3

Ion-to-electron transducing materials: insights on molecular design

3.1 Introduction

The "soft" nature and high volume accessibility to ions of highly *p*-doped PEDOT:PSS have made it the paramount system in bioelectronics.[32] Although both attributes have been the key to its particular success as an ion-to-electron converter, these characteristics have been misleadingly generalised to all organic semiconductors.[78]

The class of organic semiconductors used in plastic electronics applications such as OLEDs or OPVs differs greatly from PEDOT:PSS.[63] For instance they tend to be processed from organic solvents instead of water and have a rather hydrophobic nature which may hinder the bulk transport of hydrated ions.[83] Additionally, their conductivity is orders of magnitude lower and heavily relies on the molecular order of the polymer in its solid state.[37] However, despite these challenging differences there are opportunities to introduce to organic bioelectronics some of the exciting optoelectronic properties exploited in other fields.

Alternative mixed conductors could also open new pathways of operation in current devices functioning in aqueous media. In order to bridge the gap, it is interesting to study potential intrinsic (undoped) ion-to-electron converters. For this purpose, rational molecular design would be beneficial. In analysing the role of PSS in PEDOT:PSS it is evident that it degenerately dopes the semiconductor as well as enabling the conducting polymer to be dispersed and processed using water as solvent.[84] In other words, PEDOT:PSS can be thought of as a blend of PEDOT and PSS in a length-scale close to the molecular-scale. Additionally, the highest mobility found in the polymer bulk is equal to that of ions in water, meaning inter-diffusion of the aqueous media within the polar bulk is highly relevant.[80]

Since this thesis includes the study of intrinsic organic semiconductors as potential ion-to-electron transducers, certain qualities of the investigated materials were aimed to mimic those of PEDOT:PSS (a reference ion-to-electron converter in literature), without *p*-doping them. In an attempt to achieve a more hydrophilic bulk, polar moieties were added to the common semiconductor poly(3-hexylthiophene) (P3HT) near the 'active centres' at the molecular scale. Some examples of conjugated polyelectrolytes have appeared in the literature as alternative materials

to PEDOT:PSS, namely poly(6-(thiophene-3-yl)hexane-1-sulfonate) tetrabutylammonium and sodium poly(2-(3-thienyl)ethoxy-4-butylsulfonate).[61,85] The approach in this thesis differs from these both in that co-polymerisation is used as a tool to control the density of polar functional groups and also that these groups are of non-ionic nature.

In this Chapter a series of new model systems bearing a small functional polar group is studied. First, random copolymers are used to allow flexibility on the level of functionalisation to control the polarity of the material and, also importantly, not to compromise the solubility of the film in water. The hydrophilic nature of the derivative systems is studied, along with the molecular packing of the materials upon film formation and their charge transport properties. Finally, and more importantly, the viability of such systems as ion-to-electron converters is assessed by using an opto-electrochemical characterisation method and benchmarked with PEDOT:PSS.

The experiments presented in Section 3.3.2 were done in collaboration with Ardalan Armin at the Centre for Organic Photonics and Electronics (COPE), The University of Queensland (Australia).

3.2 Materials and methods

Poly(3-hexylthiophene) (**1:** P3HT) was purchased from Merck (mass-average molecular weight M_w = 54200 g/mol, dispersity Đ = 2.29, regioregularity RR = 94.2 %; stock SAP No EE99202) and used as received.

Polythiophene derivatives poly(3-hexylthiophene)-co-(3-(6-hydroxyhexyl)thiophene) of varying molar ratios **2:** P3HT(C6OH)$_{10\%}$ (M_w = 60000 g/mol, Đ = 1.45), **3:** P3HT(C6OH)$_{20\%}$ (M_w = 37000 g/mol, Đ = 1.30), **4:** P3HT(C6OH)$_{50\%}$ (M_w = 63000 g/mol, Đ = 1.82) and poly(3-hexylthiophene)-co-(3-(11-hydroxyundecyl)thiophene) of 1:1 ratio **5:** P3HT(C11OH)$_{50\%}$ (M_w = 90000 g/mol, Đ = 1.68) were synthesised and provided by Dr Olivier Dautel (AM2N Laboratory, Charles Gerhardt Institute, France). Figure 3.1 shows the chemical structures of polymers **1** - **5**.

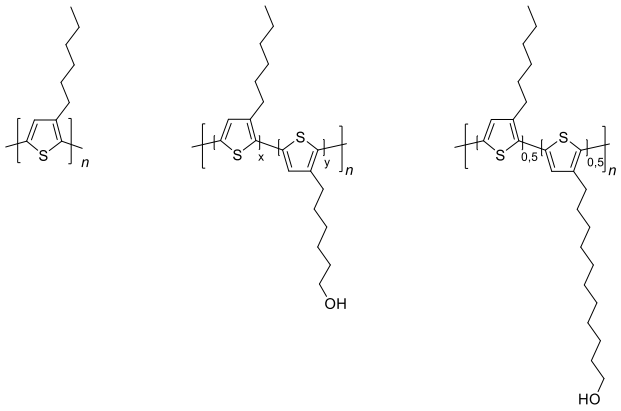


Figure 3.1: Chemical structures of polymers. **Left:** poly(3-hexylthiophene) (**1:** P3HT). **Center:** OH-containing derivatives poly(3-hexylthiophene)-co-(3-(6-hydroxyhexyl)thiophene) of varying ratios: x = 0.9, y = 0.1 (**2:** P3HT(C6OH)$_{10\%}$); x = 0.8, y = 0.2 (**3:** P3HT(C6OH)$_{20\%}$); x = 0.5, y = 0.5 (**4:** P3HT(C6OH)$_{50\%}$). **Right:** poly(3-hexylthiophene)-co-(3-(11-hydroxyundecyl)thiophene) (**5:** P3HT(C11OH)$_{50\%}$).

All polymer solutions were prepared at a concentration of 8 mg/ml and heated while stirring at 58 °C on a hotplate for a minimum of 2 h until fully dissolved. The vials were fitted in a metal chuck in order to ensure homogeneous heating and avoid partial solidification of material close to the solution/air interface. All solutions were freshly prepared and used within a window of 3 h after dissolution.

Derivatives P3HT(C6OH)$_{10\%}$ and P3HT(C6OH)$_{20\%}$ were dissolved in chloroform (with ethanol as a stabiliser) and more polar systems, P3HT(C6OH)$_{50\%}$ and P3HT(C11OH)$_{50\%}$, were dissolved in tetrahydrofuran (THF).

Thin films were prepared on glass or ITO substrates, depending on the characterisation required, following the protocols described in Section 2.1. PEDOT:PSS films were spin-cast at 800 rpm, for 2 min; the PEDOT:PSS (Clevios PH1000) solutions were prepared with the addition of ethylene glycol, DBSA and GOPS, and baked after film deposition as previously reported.[80]

3.2.1 Steady-state charge transport measurements

Sample preparation

Indium tin oxide (ITO) coated glass substrates ($\approx$ 15 Ω/Sq, Xinyan Technology Ltd.) patterned by photolithography were pre-cleaned using Alconox (detergent) solution and a soft cloth before being sonicated in sequence with Alconox, deionised (DI) water, acetone and isopropanol for 10 mins each. Substrates were 2.5 cm x 2.5 cm with 6 pixels of 0.2 cm^2 each.

Films of materials **1**, **2** and **3** were prepared by spin-coating (spinning speed 600 rpm for 25 s) using chloroform as solvent; THF was used for **4**. All solutions were prepared at 20 mg/ml concentration; 10 % of ortho-dichlorobenzene was added to ensure films dried slowly.

J - V characterisation

Current density vs. voltage (J - V) characteristics were acquired in a nitrogen atmosphere using a Keithley 2400 Source Measure Unit.

3.2.2 Contact angle

A sessile drop setup (Krüss) was used to measure the static contact angle of water on polymer films. A droplet of the test liquid (5 μl, distilled water) was deposited on the surface of dry

polymer films (blow dried beforehand to eliminate any particles/dust). An image of the droplet was taken during the first 2 - 3 s and the angle between the substrate (baseline) and the tangent at the liquid/air boundary was calculated. Three measurements were done on a minimum of two samples from different batches.

3.2.3 Cyclic voltammetry

Cyclic voltammetry (CV) was performed in "liquid" and "solid state films" in a common electrolyte (THF and acetonitrile).

For liquid CV, 10^{-3} M THF solutions of polymers **1** - **5** with 0.1 M of tetrabutylammonium hexafluorophosphate (Bu_4NPF_6) as electrolyte were used.

For solid state films, thin films of polymers **1** - **5** were deposited onto a Pt electrode from THF solution. When the films were dry, these were immersed in 0.1 M Bu_4NPF_6 electrolyte, in acetonitrile solution.

All measurements were done at room temperature and ferrocenium/ferrocene (Fc^+/Fc) redox couple was used as external reference ($E_{Fc^+/Fc}$ = 0.45 V/SCE). Pt wires were used as working and counter electrodes and an Ag wire as pseudo reference electrode. Potentials are given versus saturated calomel electrode (SCE).

3.2.4 Real-time electroactivity: assessing ionic transport

In this study light absorbance was chosen as a means of tracking the electroactivity of the polymers in real-time, which allowed a time resolution capability down to 1 ms. A sketch of the measuring setup is shown in Figure 3.2. The polymer films coated on ITO were washed with DI water and blow dried with air before any characterisation. A poly(dimethylsiloxane) (PDMS) well was placed onto the films and filled with 1 ml of 10 mM NaCl water electrolyte. An Ag/AgCl pellet electrode (E-205, Warner Instruments) was fully immersed in the electrolyte. The system was then placed under the focus of a bright-field optical microscope (Olympus

BX51 with 20X objective), using the illumination as light source for the fibre optic spectrometer (USB2000+ Miniature Fiber Optic Spectrometer, Ocean Optics, and data acquisition software SpectraSuite), which was aligned to the system as a light collector. The ITO and Ag/AgCl electrodes were connected to a DC voltage source (PL155 power supply, Aim-TTi Instruments). A reference spectrum was obtained using a bare ITO substrate and an equivalent PDMS well filled with electrolyte. Subsequently, absorbance spectra over the range of 350 - 750 nm were recorded every 100 ms while the sample was biased.

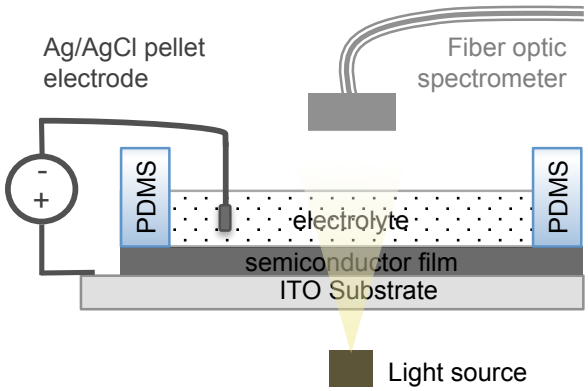


Figure 3.2: Schematic of the electrochromic measuring setup used to characterise the elctroactivity of materials. Fast real-time absorbance spectra (every 100 ms) were measured when a step voltage was applied.

Since polythiophenes can generally be *p*-doped, measurements were started with a positive bias V applied to the bottom ITO substrate with respect to the Ag/AgCl at time t = 0 s, which is called V_{ON}.[(1)] The bias V_{ON} was maintained for up to 28 s, before it was returned to 0 V and maintained for another 28 s (bias referred to as V_{OFF}). The voltage was then reversed to V_{REV} = -V with the intention of observing any dedoping (reduction) and to expel any remnant ions "trapped" inside the polymer, completing one full bias run.[(2)]

Full visible absorbance spectra were recorded during the characterisation. Generally, the raw absorbance data (arbitrary units) is represented versus the wavelength (nm) as a function of

[(1)]Note that the reference electrode in the system is the top electrode, Ag/AgCl, as opposed to the typical OECT setup in which the reference electrode is the Source, generally located at the bottom.

[(2)]Data recording for each bias section was always started 1 - 2 s before applying the bias, hence ensuring a few data points of constant signal that were later removed. Time $t = 0$ s was hence set a posteriori during data analysis.

time (s). Hence, the variable dependency of the absorbance is

$$absorbance = abs\ (\lambda, t) \tag{3.1}$$

where λ is wavelength and t is time. A sketch is presented in Figure 3.3 (left) of a hypothetical polymer oxidising over time upon an applied bias; the absorption reduces from $t = 0$ s (black curve) to a time t that can take any positive value depending on the experimental conditions (from red to pink curves).

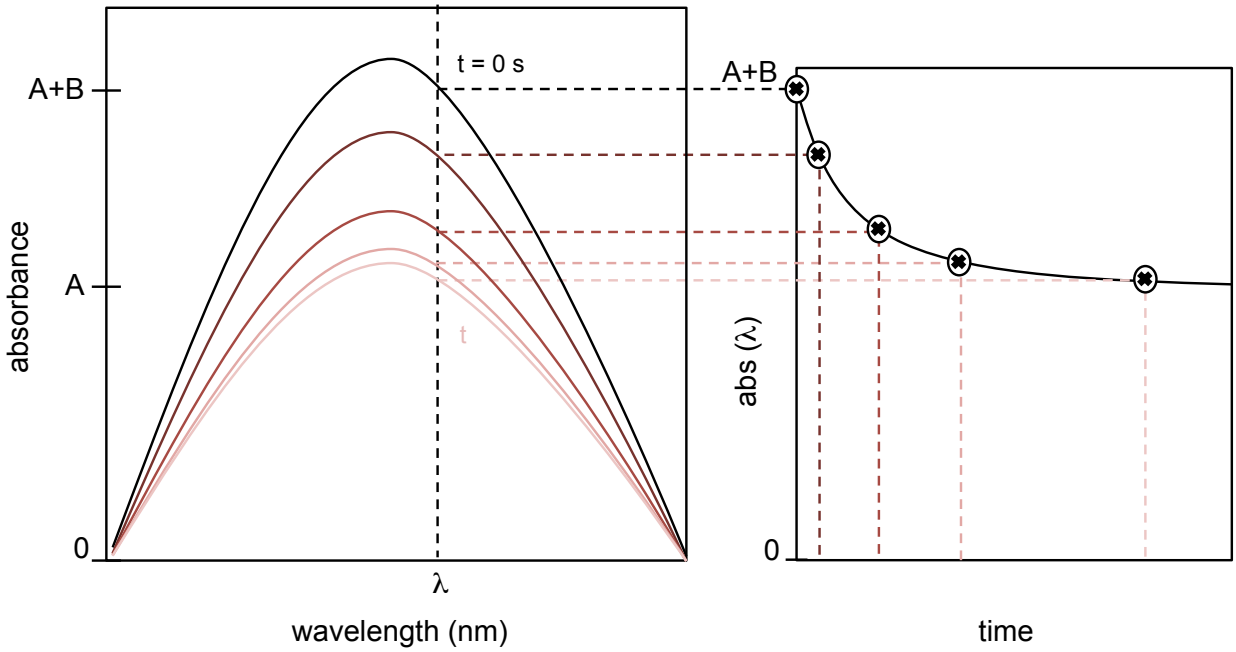


Figure 3.3: **Left:** Sketch of the absorbance spectra of a hypothetical polymer undergoing oxidation over time. **Right:** Representation of the absorption at a specific wavelength λ versus time.

However, the dynamics of the process can be more clearly pictured by tracking the absorbance at one specific wavelength over time (Figure 3.3, right). Since the absorbance of a film is a magnitude that depends on variables such a film thickness, the comparison of absorbance between systems is generally done after the data is normalised, either to the maximum or to a specific wavelength. In this case, the absorbance at a wavelength of 550 nm was selected to normalise the data at time $t = 0$ s. This is a common reference wavelength for normalising

the absorbance spectra of P3HT and its derivatives. Given that the interest is laid on tracking changes over time due to the oxidation of the material, the absorbance curves at time t were normalised to the absorbance at time $t = 0$ s at the selected wavelength. Note that $t = 0$ s is the reference time point and that the normalisation only affects the scale of the axis, as all values are divided by the same quantity.

Since all absorbance is normalised relative to that at $t = 0$ s, it will be called relative absorbance. The relative absorbance is plotted versus time and is calculated as

$$rel.\ abs._{\ [550nm]} = \frac{abs\ (550, t)}{abs\ (550, 0)} \tag{3.2}$$

where $abs\ (550, t)$ is the absorbance at a wavelength 550 nm and at a time t, and $abs\ (550, 0)$ is the absorbance at the same wavelength at time 0 s.

Analysis of the time dependency

As described above (Equation 3.2), the relative absorbance was plotted as a function of time. By this definition, the relative absorbance data starts at a value of 1 at time $t = 0$ s and, due to the expected oxidation of the material under the applied bias, decreases towards smaller values eventually reaching saturation or near-saturation (depending on the time-scale in which the experiments were performed).

In parallel with the time dependency analysis that is found in OECTs-related work,[61,86,87] one approach towards learning about the time dependency of the material systems would be to assume an exponential decay. A simplistic description of the typical decay model is presented here and also the small variations that can be encountered in the studied system in particular.

Figure 3.4 (left) depicts a sketch of a simple exponential decay of total amplitude B and decay time τ.

$$Abs(t) = Be^{-t/\tau} \tag{3.3}$$

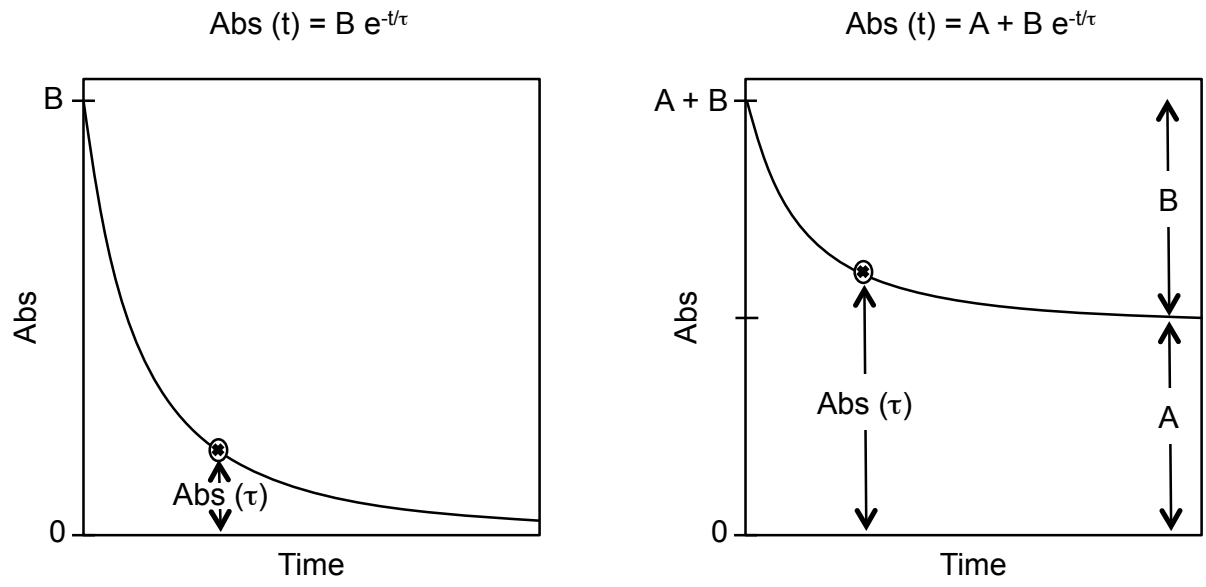


Figure 3.4: Exponential decay models. **Left:** exponential decay from an amplitude of B to 0. **Right:** general exponential decay starting at a value of A + B and decaying to a baseline of value A. Both decays have a maximum amplitude of B and characteristic decay time τ.

At the time point $t = \tau$, the absorbance takes a value of 1/e (0.37) times its amplitude B.

$$Abs(\tau) = \frac{B}{e} \tag{3.4}$$

Equivalently, *Abs* drops by a factor of $1 - 1/e$ (0.63) of its initial value.

A more general exponential decay is shown in Figure 3.4 (right) in order to depict a model closer to what the data looks like (refer to Figure 3.3 for comparison with a hypothetical polymer response during oxidation). The function plotted is

$$Abs(t) = A + Be^{-t/\tau} \tag{3.5}$$

The absorbance data of the systems tested was normalised as previously defined in Equation 3.2. Hence, for this case Equation 3.5 takes a value $Abs(0) = 1$, creating the condition $A + B = 1$. Under this condition, the variable *Abs* in the sketch (Figure 3.4, right) becomes relative absorbance *rel. abs*. When the experiment's data is plotted it looks like the case of Figure 3.5,

in which the conditions of *rel. abs.* are fulfilled.

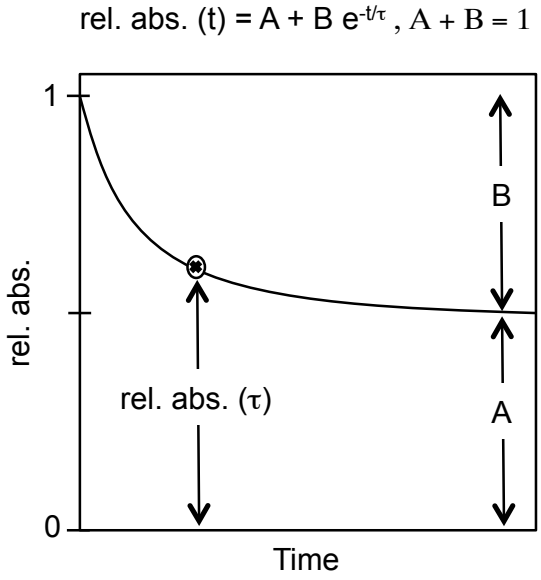


Figure 3.5: Exponential decay model for the normalised absorbance, as the experiment's data is presented.

Similarly to the simpler model (Figure 3.4, left), τ is the characteristic decay time and B the total amplitude of the decay. In this case the *rel. abs.* tends to a baseline of value A (when $t \to \infty$) instead of 0.

At the time point $t = \tau$, the *rel. abs.* reaches 1/e (0.37) times its amplitude B, over the baseline

$$rel.\ abs.(\tau) = A + \frac{B}{e} \qquad \rightarrow \qquad rel.\ abs.(\tau) - A = \frac{B}{e} \tag{3.6}$$

or equivalently dropping from 1 by a factor of $1 - 1/e$ (0.63) of the maximum amplitude B.

At the level of bias applied, the absorbance response of the system displays a behaviour close to a negative exponential vs. time (similar to that in Figure 3.5); however, deviations encountered in some of the systems to such a trend led to another approach to the data analysis which retained a similar concept to the one above but avoided fitting to an exponential function; these deviations from a single to a multi-exponential decay will be shown in further detail in Chapter 4, Sections 4.3.3 and 4.3.4.

In this approach, t_{80} was defined as the time required for the relative absorbance to be reduced by a factor of 0.8 (80 %) of the maximum amplitude of the decay (B in general decay model; in this approach, since the data was not fitted to a model, the last decay value during oxidation measured in the time-range 0 - 28 s, $rel.\ abs.\ (28\ s)$ was used).

$$\begin{aligned} t_{80} = \{t | rel.\ abs.(t) = 0.2(1 - rel.\ abs.(28s)) + rel.\ abs.(28s)\} \\ t_{80} = \{t | rel.\ abs.(t) = 1 - 0.8(1 - rel.\ abs.(28s))\} \end{aligned} \tag{3.7}$$

Equation 3.7 defines t_{80} as the time t when the condition on $rel.\ abs.(t)$ to the right-hand-side is fulfilled.

This definition poses a more restrictive drop of 80 % (0.8) in absorbance, compared to the drop by a factor of 0.63 that characterises the decay time τ. The reason behind choosing a more restrictive fraction of absorbance drop (from 0.63 to 0.8) is based in the attempt to compare all systems equally across the body of this thesis; in Chapter 4, Sections 4.3.3 and 4.3.4, it will become clearer how the longer decay time (more restrictive drop) ensures that it accounts for the possibly multiple characteristic decay regimes of every system.

In summary, t_{80} is a useful parameter to compare the time response of the different systems without resorting to inaccurate fitting to a decay model while retaining a similar physical meaning as the characteristic time τ. Maintaining a similar concept for the calculation of the decay time is important when comparing systems which saturate at different levels, since the time calculated considers relative changes to the maximum amplitude of each of them, hence allowing for fairer comparisons.

3.3 Results and discussion

3.3.1 Thiophene derivatives bearing -OH moiety: thin-film solid-state and polarity

The range of materials of interest in this study ranged from the more hydrophobic **1** to increasingly more -OH functionalised co-polymers **2** - **5** (Figure 3.1). Co-polymerisation was chosen as a versatile approach to achieve more polar materials without compromising the solubility and semi-crystalline nature of the solid state films. Achieving an appropriate microstructure that supports charge transport could be compromised if secondary components such as a crosslinker were added, which could be the case for materials easily soluble in water. Hence, controlling the level of functionalisation to ensure film integrity in water is vital. Additionally, this approach allowed to maintain the fewest free parameters across the systems and therefore to track back a more genuine effect of functionalisation on certain properties.

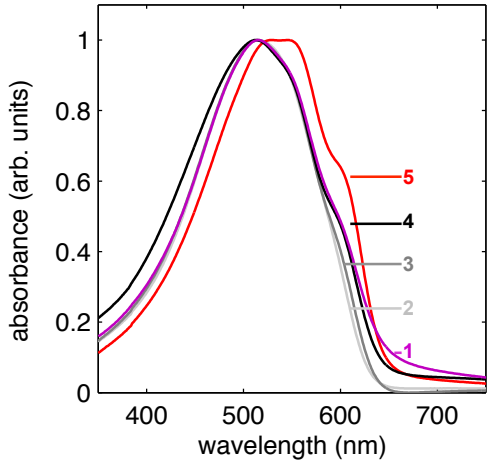


Figure 3.6: UV-Visible absorbance spectra of thin films. **1:** P3HT, **2:** P3HT(C6OH)$_{10\%}$, **3:** P3HT(C6OH)$_{20\%}$, **4:** P3HT(C6OH)$_{50\%}$ and **5:** P3HT(C11OH)$_{50\%}$.

It is observed that the addition of the small functional group -OH did not affect the short-range order of the polymers **2** - **4**, as seen by the similar absorbance spectra of thin films of these materials to that of **1:** P3HT (Figure 3.6). This suggests that the interactions of -OH groups do not affect the short-range packing of the polythiophene derivatives, which is highly relevant

to maintain charge transport.[37] Material **5** shows more pronounced peaks indicating enhanced short-range aggregation. This is not surprising since the presence of the longer alkyl chain is expected to have a larger effect on its supramolecular order; Section 3.3.4, later on in this chapter, will focus on this system.

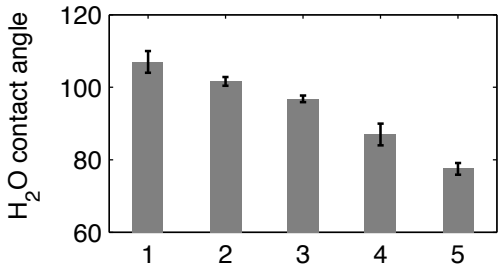


Figure 3.7: Contact angle of DI water measured on dry films. **1:** P3HT, **2:** P3HT(C6OH)$_{10\%}$, **3:** P3HT(C6OH)$_{20\%}$, **4:** P3HT(C6OH)$_{50\%}$ and **5:** P3HT(C11OH)$_{50\%}$. Functionalisation with -OH systematically reduced contact angle.

Functionalisation with -OH groups led to more hydrophilic films, as deduced from the fact that the contact angle of water is systematically reduced with increasing -OH number (from 103° on **1**: P3HT to below 80° on **5**: P3HT(C11OH)$_{50\%}$, Figure 3.7). This indicates that part of the -OH groups are being exposed at the surface, which has previously been exploited as a tool for biofunctionalisation of PEDOT surfaces.[60] More hydrophilic materials are expected to have better compatibility with aqueous environments, promising improved inter-diffusion of biological media through the system. This can include bioactive molecules or simply hydrated ions belonging the buffer/electrolyte.

3.3.2 Electronic transport

The charge carrier mobility of materials **2** - **4** was calculated by measuring the steady-state current - voltage characteristics of thin films in a hole-only device structure. Details of sample preparation and characterisation can be found in Section 3.2.1. The current density vs. voltage curves are displayed in Figure 3.8.

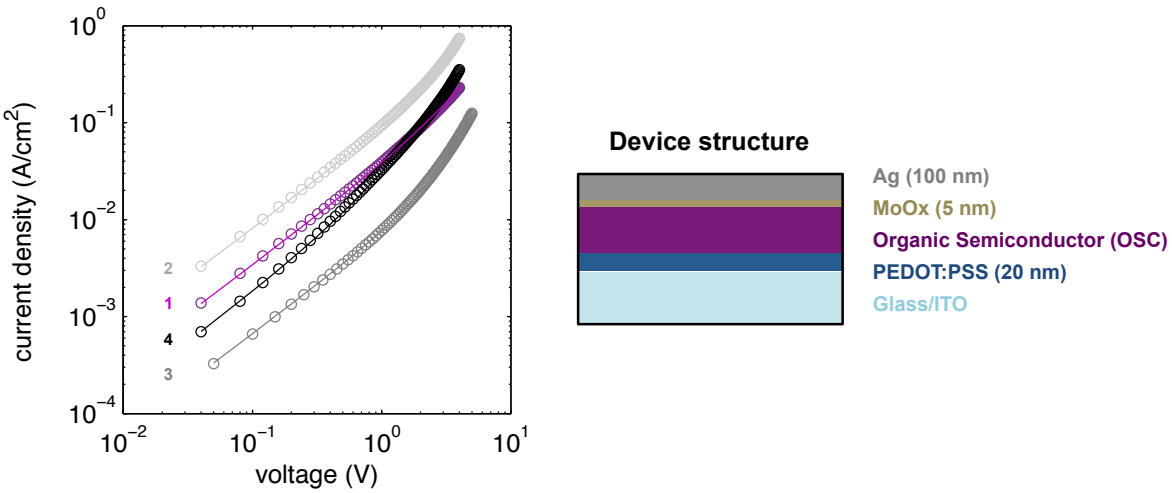


Figure 3.8: **Left:** Experimentally measured current vs. voltage data for materials **1** - **4** and fitted curves. **Right:** Schematic of the device structure used: ITO/PEDOT 20 nm/OSC/MoOx 5 nm/Ag 100 nm. Measurements were performed with device area of 0.01 cm^2 so that series resistance can be neglected. **1:** P3HT, **2:** P3HT(C6OH)$_{10\%}$, **3:** P3HT(C6OH)$_{20\%}$ and **4:** P3HT(C6OH)$_{50\%}$. *Experiment performed by Ardalan Armin at the Centre for Organic Photonics Electronics (COPE), The University of Queensland (Australia).*

The current density is given by

$$j = \mu_0 peE + \frac{9}{8}\epsilon_r\epsilon_0\frac{V^2}{d^3}\mu_0 e^{0.89\gamma\sqrt{E}} \tag{3.8}$$

where μ_0 is the zero-field hole mobility, p the equilibrium hole concentration in the dark, E ($= V/d$) the electric field, d the film thickness, ϵ the dielectric constant, γ the field dependence coefficient and V the applied voltage. In Equation 3.8 the first term corresponds to the Ohmic current and the second to the space-charge limited current (SCLC) represented by the Mott-Gurney equation, modified with Poole-Frenkel field-dependent mobility. In this description it is

considered that the carrier transport is limited by the space charge accumulated in the carrier transport layer at the injected side, as well as accounting for possible traps that affect the mobility at strong fields (Poole-Frenkel term).

Table 3.3.2 summarises the relevant fitting parameters for each material: mobility, field dependence coefficient and hole concentration in the dark.

Material	μ_0 [cm^2/(V s)]	γ [(m/V)$^{1/2}$]	p [cm^3]
1	3.0×10^{-4}	9.0×10^{-4}	2.0×10^{16}
2	5.0×10^{-4}	5.3×10^{-3}	3.3×10^{16}
3	5.0×10^{-5}	6.5×10^{-3}	2.9×10^{16}
4	3.1×10^{-3}	1.3×10^{-3}	1.5×10^{15}

Table 3.1: Mobility, field dependence coefficient and hole concentration of polythiophene polymers, as obtained from data fitted from Figure 3.8. **1:** P3HT, **2:** P3HT(C6OH)$_{10\%}$, **3:** P3HT(C6OH)$_{20\%}$ and **4:** P3HT(C6OH)$_{50\%}$. *Data fitting and parametres extraction performed by Ardalan Armin at the Centre for Organic Photonics Electronics (COPE), The University of Queensland (Australia).*

The mild level of functionalisation of **2** does not seem to affect charge transport, as seen by the similar mobility at zero bias of this material in comparison to **1:** P3HT. However, **2** has a larger field dependence, as measured by γ, which is an indication of an increase in the number of traps.

The next system with increasing number of -OH units, **3**, has an order of magnitude lower hole mobility. However, the similar value of γ suggests that the larger number of -OH units does not increase the number of traps. The lower mobility of **3** may be related to its lower mass-average molecular weight M_w compared to the other systems (M_w = 54200, 60000, 37000 and 63000 g/mol, for **1**, **2**, **3** and **4** respectively) rather than the functionalisation level; it has been previously reported that variations in the M_w of regioregular P3HT "causes the mobility to vary at least four orders of magnitude".[88] Although these abrupt changes in the mobility of P3HT were calculated in FET devices, bulk mobility derived from OPV devices has also been shown to decrease with decreasing M_w.[89]

An increase in mobility by an order of magnitude is observed in the case of **4** while maintaining similar field dependence to the rest of the functionalised materials. Although the fitting of the data is of similar quality to the rest, the mobility value should be considered with caution due to the poorer quality of the films prepared for the devices of this material. However, it is still possible to consider this data qualitatively based on the larger mobility calculated, concluding that the larger -OH density, if anything, does not hinder charge transport.

In summary, no major changes are observed in the charge transport properties of the functionalised materials. In addition, it is difficult to attribute the variations exclusively to the functionalisation level, since factors such as M_w and the processing conditions also play a role in semi-crystalline systems' charge transport. Nonetheless, similar charge transport is found for **1** and **2**, and a general increase of traps is found for the functionalised systems, although without a clear correlation to the density of -OH.

3.3.3 Ionic transport: an optical assessment

Ionic transport in mixed conducting polymers has been assessed qualitatively in the literature by means of monitoring the electrochemical doping/dedoping in devices and other simpler thin film structures.[18] Electrochemical doping involves the incorporation of ionic species in the bulk of the polymer acting as counter-ions whose function is to charge-compensate the removal of a hole or electron for *n* and *p*-doping, respectively. The materials act, effectively, as ion-to-electron converters and it is common in the literature to refer to the process as a transduction of ionic to electronic signal and vice-versa.

Simultaneously to the increase in conductivity of the organic semiconductor, other observable qualities can change during electrochemical doping/dedoping, for example colour (electrochromism) and volume (used for mechanical actuators).[18] Since all these changes happen as a response to an applied electric field (bias), these materials can also be referred to as electroactive. In the field of bioelectronics the electroactivity of this class of materials is highly relevant in order to produce functional interfaces.

Therefore the effect of the functional -OH group on ionic transport was scrutinised by testing the electroactivity of the series of conducting polymers **1** - **5**. A schematic of the electrochromic measuring setup employed for this purpose is shown in Figure 3.2 and full details of the measuring conditions can be found in Section 3.2.4.

In order to decide an appropriate voltage to perform the electrochromic tests, cyclic voltammetry of polymers **1** - **5** was measured in liquid, where polymers were dissolved in THF along with the common electrolyte tetrabutylammonium hexafluorophosphate (Bu_4NPF_6); details in Section 3.2.3. Figure 3.9 (top) shows the voltammogram covering the full voltage range (left), including a ferrocenium/ferrocene (Fc^+/Fc) redox couple. A close-up in the voltage range were oxidation takes place is also shown (Figure 3.9, top-right), where 0.75 V is marked as the voltage selected for the electrochromic experiments. It is observed that all polymers are starting to oxidise at that voltage in a common electrolyte, hence being of interest to test their behaviour when in contact with a water electrolyte.

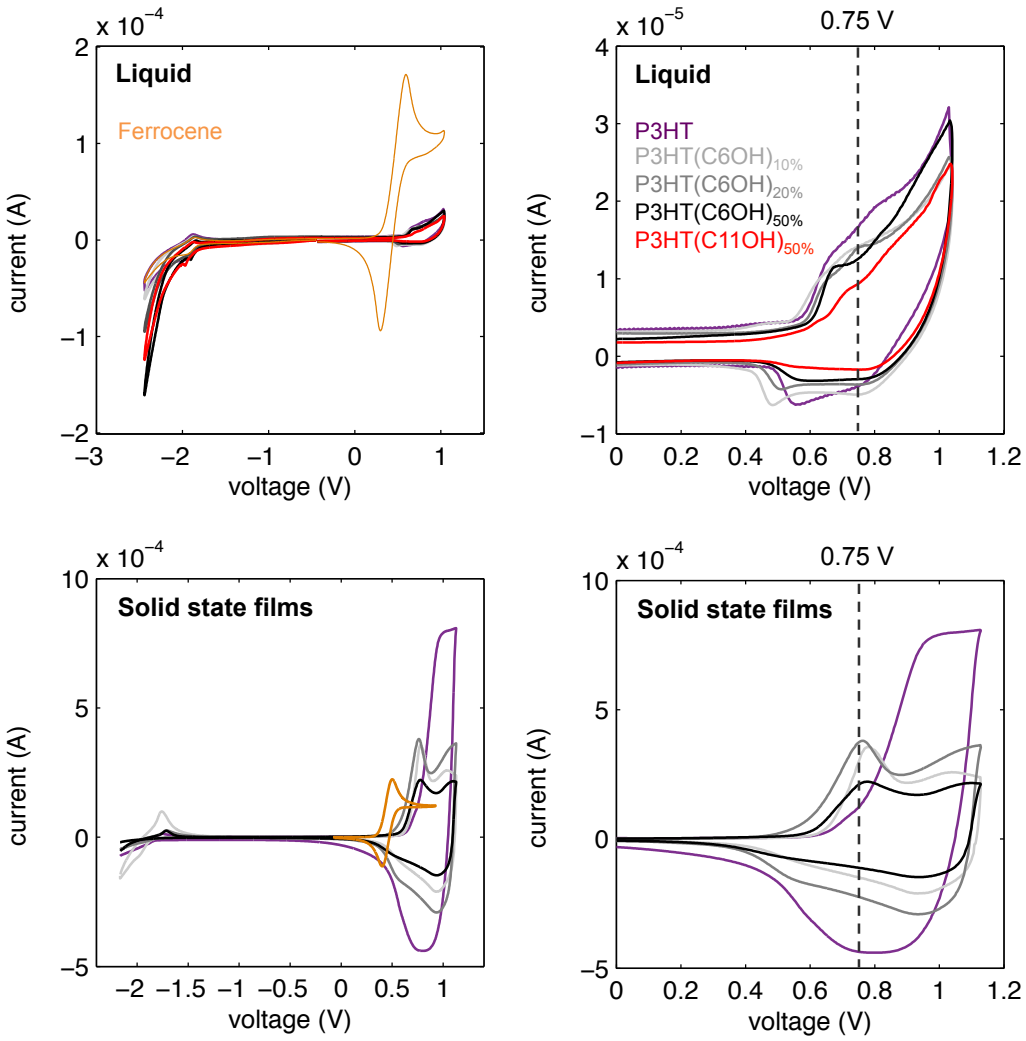


Figure 3.9: Cyclic voltammograms of polymers **1** - **5**. **Top:** polymers in solution, dissolved in THF. **Bottom:** polymers cast as thin film onto a conducting electrode (Pt) and immersed in an acetonitrile solution. In both cases, tetrabutylammonium hexafluorophosphate (Bu_4NPF_6) was used as electrolyte, and measurements performed at RT. On the right a close-up of the voltage range where oxidation takes place is shown, for liquid and solid state films.

Figure 3.9 (bottom) also displays the voltammograms of polymers when cast as thin films onto a Pt electrode. Differences are encountered in the shape of the curves, which may be related to the short-range ordering of the polymers when in solid state. Although no further explanations can so far be given, 0.75 V appears here also as a relevant voltage to test, particularly being around the oxidation peaks of the polythiophene derivatives and to a lesser oxidation extent for P3HT.

Using the electrochromic setup, materials **1** - **4** will be firstly compared; these differ chemically

from each other on the level of -OH functionalisation from 0 to 50 % of their monomer units while maintaining their alkyl chain length (6 carbons units) and their short-range order in the solid state (Figure 3.6). With the same measuring conditions for all systems, a bias run was performed starting at 0 V, followed by the subsequent application of bias V_{ON}, V_{OFF} and V_{REV}.

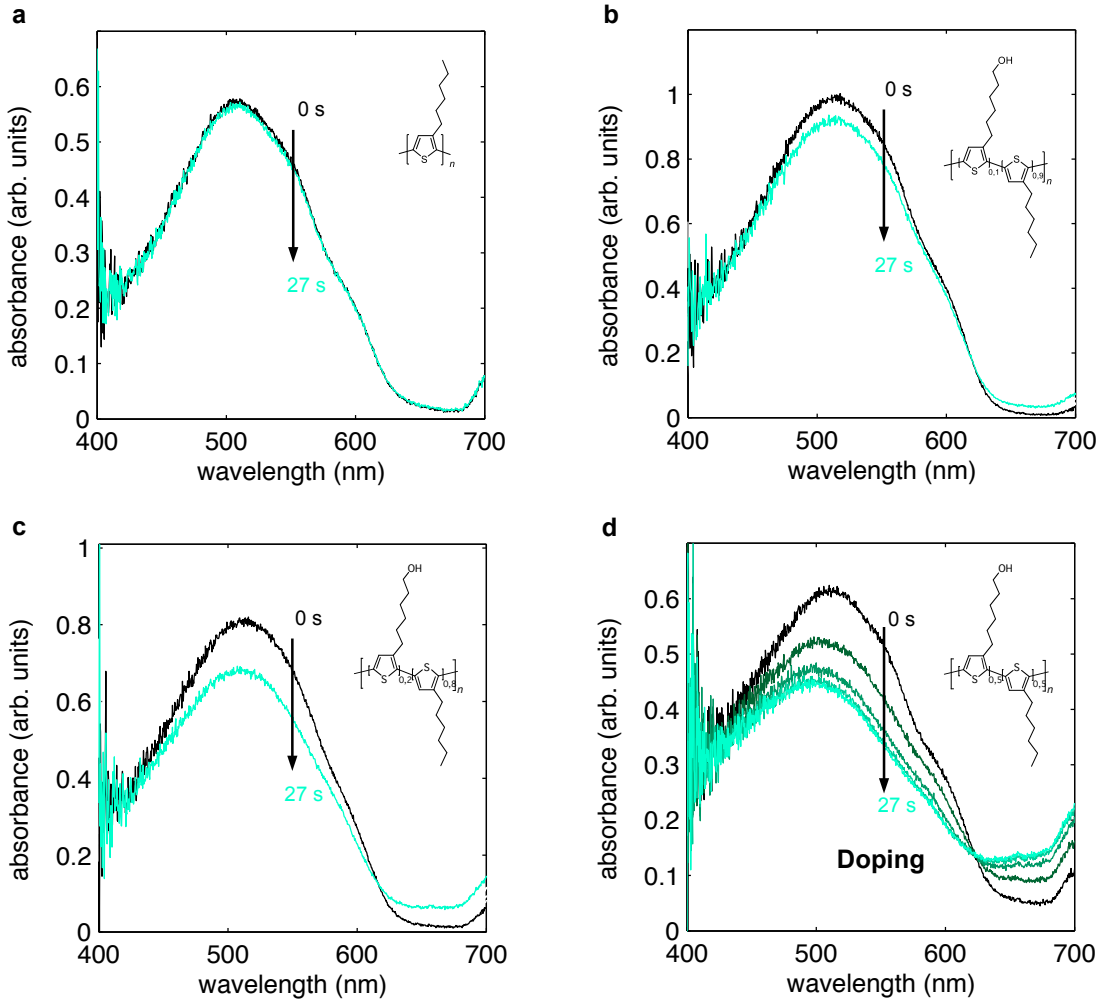


Figure 3.10: Real-time visible absorbance spectra of polymer thin films when bias $V_{ON} = 0.75$ V is applied in the setup displayed in Fig. 3.2. Spectra in **a**, **b** and **c** is shown at times 0 (black) and 27 s (light green); in **d** times 0, 1, 3, 9 and 27 s are displayed (from black to light green).

Figure 3.10 shows the absorbance spectra of materials **1** - **4** over time with the applied bias V_{ON} in the range between 400 - 700 nm. The oxidation of the semiconductor is clearly observed in the reduction of the absorbance peaks, with a clear trend from the near-nil response of **1**

to the larger response of **4** (panels **a** - **d**, respectively). Absorbance spectra are displayed as follows: for systems that show a nil or weak response (**1** - **3**, panels **a** - **c**, respectively), the initial spectra and the spectra after 27 s of applied bias are shown; for the one system that displayed a larger response (**4**, panel **d**), spectra are shown for times 0, 1, 3, 9 and 27 s of applied bias.

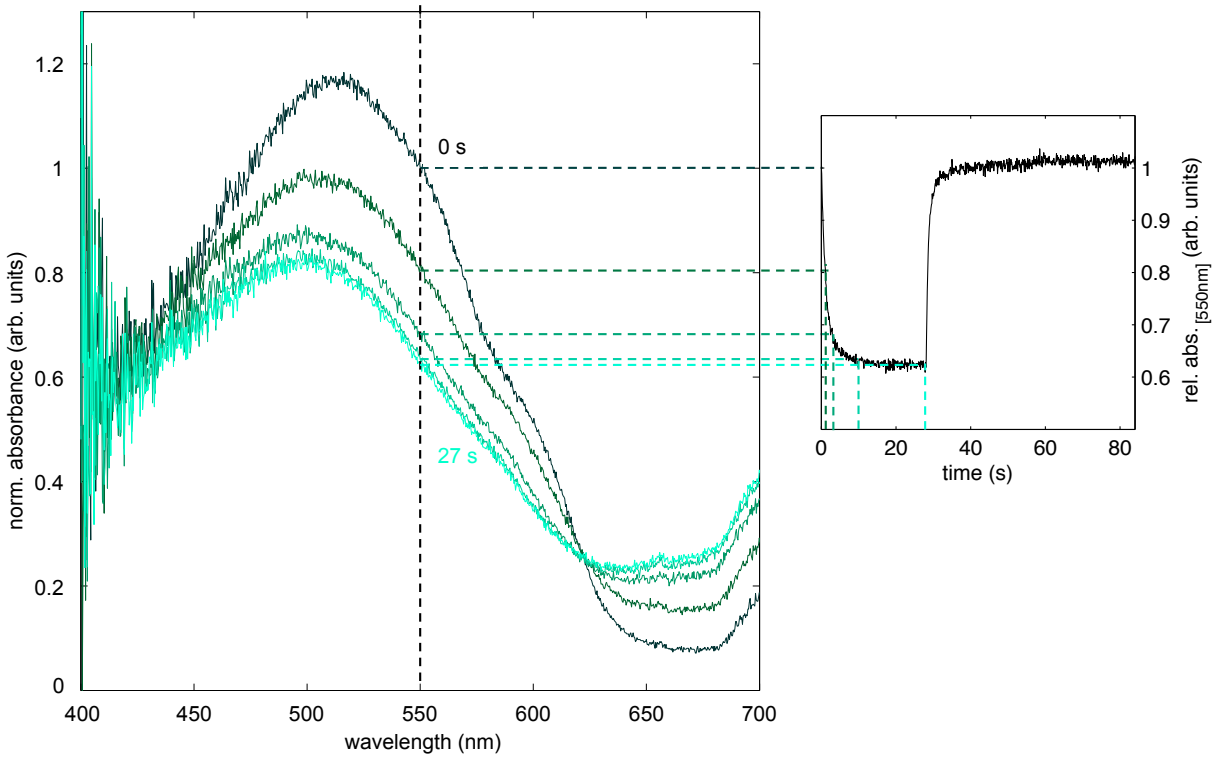


Figure 3.11: **Left:** Real-time visible absorbance spectra of polymer thin film of **4** when a bias of V_{ON} = 0.75 V was applied in the setup displayed in Fig. 3.2. Spectra at times 0, 1, 3, 9 and 27 s are displayed. **Right:** Time dependency of the relative (normalised) absorbance at 500 nm. It includes the response during V_{OFF} = 0 V (28 - 56 s) and V_{REV} = -0.75 V (56 - 84 s). Axes are aligned and to the same scale.

In order to show a comparative picture of the systems' time-response, the absorbance at 550 nm was plotted as a function of time. An example is shown of material **4** of the data transformation that takes place between the absorbance of the film (Figure 3.10, pannel **d**), its subsequent normalisation to the absorption at 550 nm at time t = 0 s (Figure 3.11, left) and the time dependency of such relative (normalised) absorbance at 550 nm (Figure 3.11, right). The last graph allows the comparison between systems' electroactivity, given that all are normalised to a starting value of 1, and hence is independent of variations in film thickness across samples.

Figure 3.12 shows the comparison of systems **1** - **4** after following equivalent transformations to those depicted for **4** in Figure 3.11. The increasing density of -OH groups from 10 % to 50 % (materials **2** - **4**) clearly accentuated the materials' electroactivity, as was observed during the oxidation in Figure 3.10 (V_{ON}, 0 - 28 s). In Figure 3.12, an empty circle indicates the point where t_{80} is reached for each of the responsive materials.

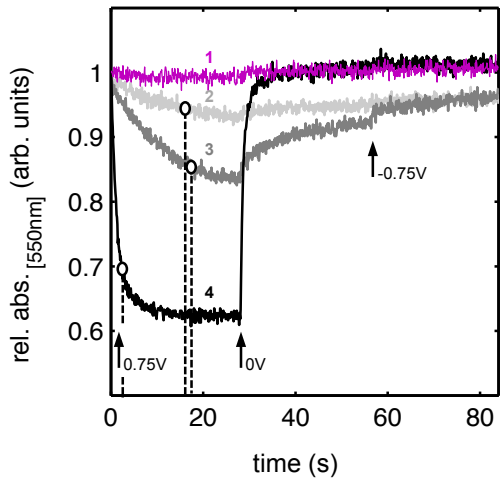


Figure 3.12: Relative absorbance spectra at 550 nm as a function of time with different applied bias: V_{ON} = 0.75 V (0 - 28 s), V_{OFF} = 0 V (28 - 56 s) and V_{REV} = -0.75 V (56 - 84 s). **1:** P3HT, **2:** P3HT(C6OH)$_{10\%}$, **3:** P3HT(C6OH)$_{20\%}$ and **4:** P3HT(C6OH)$_{50\%}$. The electroactivity increased as a function of density of -OH functional groups. An empty circle indicates the point where t_{80} is reached for each of the responsive materials.

Enhanced performance upon -OH loading was observed in the following relevant characteristics:

- *Extent of oxidation*: relative absorbance drop at saturation, or near-saturation. It is a positive quantity, calculated as the modulus of the absorbance drop from the baseline 1 (also referred to as amplitude of the response, details in Section 3.2.4)

- *Speed of reaction*: associated with its characteristic time in the change of absorbance (in this case the characteristic time of the oxidation reaction)

- *Stability over time*: percentage reduction of the extent of oxidation after multiple bias runs

- *Reversibility of the redox process*: how well it achieves returning to the initial absorbance after dedoping

Unless otherwise stated, these characteristics will be analysed based on the response over the oxidation reaction (0 - 28 s). It is important to remark that the absorbance spectra at different time points, such as those shown in Figure 3.10 for all systems, were normalised to the absorbance at 550 nm at time $t = 0$ s. Hence, the initial relative absorbance value is 1 for all cases and this changed to values < 1 during the oxidation reaction due to the reduction in absorbance upon oxidation, with larger changes indicating a larger response to the applied bias (details of the time response parameters in Section 3.2.4).

Extent of oxidation (EO)

The extent of the oxidation (EO), or (electrochemical) doping, during the positive step bias (0 - 28 s) was deduced from the drop of the relative absorbance between 0 to 28 s; hence, it was calculated as the difference in relative absorbance between these two time-points as follows

$$EO = |rel.\ abs.\ (0\ s) - rel.\ abs.\ (28\ s)| = |1 - rel.\ abs.\ (28\ s)| \tag{3.9}$$

The average EO of the materials became systematically larger with increased functionalisation level,[(3)] with a value of ≈ 0.37 for **4**, in contrast to a ≈ 0.17 and ≈ 0.8 for **3** and **2**, respectively. The larger drop in *rel. abs.* from **2** - **4** can be clearly observed in Figure 3.12. Material **1:** P3HT did not oxidise under the working bias (effectively EO = 0, no drop in *rel. abs.*), displaying a flat profile during the bias run. This result is itself a proof-of-principle that materials bearing more polar moieties may be required for applications in bioelectronics that benefit from electroactive interfaces.

[(3)]The average saturation (or near-saturation) values, referred to as *rel. abs.* (28 *s*), of materials **2** - **4** are 0.92, 0.83 and 0.63, respectively.

Speed of reaction

Based on observations of the relative absorbance change over time, it is clear that the oxidation reached its saturation (or near-saturation) value at a faster rate as the functionalisation increased from **2** - **4**, with the last material clearly showing a rapid response to the applied voltage (Figure 3.12). An estimate of the time before reaching 80 % of the total decrease, t_{80}, provides a comparison of the speed of reaction between systems (see Section 3.2.4 for a further description of t_{80}). For the electroactive (responsive) materials, the response time t_{80} decreased systematically upon -OH loading: from $t_{80,\ 2-3} \approx 15 - 17$ s to $t_{80,\ 4} \approx 3$ s. These values have been indicated in Figure 3.12 with an empty circle for each responsive material. This is an indication of improved ionic conductivity, based on the understanding that ionic species are slower carriers in the polymer bulk than holes, as previously reported.[80] Due to acting as the limiting factor in the redox process, an enhancement in the speed of the reaction can be attributed to faster transport of ionic species. Hence, it can be concluded that -OH loading positively contributes to ionic transport within the material's bulk.

Stability over time

Multiple bias runs, each of a total duration of 84 s, were performed in order to study the stability of films over time. As explained in further detail in Section 3.2.4, each run consisted of three voltages applied for 28 s each in turn, in the order V_{ON}, V_{OFF} and V_{REV}. The stability of each material was estimated as the percentage reduction of its extent of oxidation (EO) after 10 bias runs; the larger the reduction the less stable.

The percentage reduction in the EO was calculated by dividing the change in the EO from run 1 to 10 by the EO in run 1, as in equation(s) 3.10.

$$\% \; reduction = \left| \frac{EO \; run \; 1 - EO \; run \; 10}{EO \; run \; 1} \right| \times 100 \tag{3.10}$$

$$\% \; reduction = \left| \frac{rel. \; abs._{\; run \; 10} \; (28 \; s) - rel. \; abs._{\; run \; 1} \; (28 \; s)}{1 - rel. \; abs._{\; run \; 1} \; (28 \; s)} \right| \times 100$$

Figure 3.13 shows an example of the parameters considered in the calculation for material **3:** P3HT(C6OH)$_{20\%}$, from its relative absorption over time.

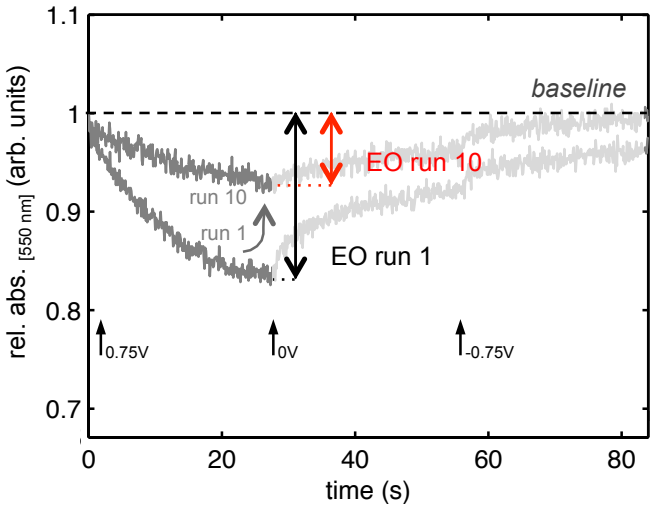


Figure 3.13: Estimation of polythiophene derivatives' stability by the reduction of the extent of oxidation (EO) in **3:** P3HT(C6OH)$_{20\%}$. Calculations of such relative reduction are done between run 1 and 10 for all materials of interest.

In Equation(s) 3.10, $rel. \; abs._{\; run \; 1} \; (28 \; s)$ and $rel. \; abs._{\; run \; 10} \; (28 \; s)$ are the relative absorbance values at 28 s during bias runs 1 and 10, respectively. A summary of these values under the columns $rel. \; abs._{\; 1}$ and $rel. \; abs._{\; 10}$ are presented in Table 3.2 for each of the responsive materials, along with the calculated EO for runs 1 and 10.

Material	rel. abs. $_1$	rel. abs. $_{10}$	EO run 1	EO run 10
2	0.92	0.98	0.08	0.02
3	0.83	0.90	0.17	0.10
4	0.63	0.66	0.37	0.34

Table 3.2: Saturating relative absorbance value at 550 nm during runs 1 and 10 for materials **2** - **4**, as measured at time $t = 28\ s$, and corresponding EO values.

The relative reduction of the EO was found to be 75 %, 41 % and 8 % for **2** - **4** respectively, suggesting that the stability of the materials during redox was also enhanced by the presence of -OH groups.

However, the reduction in the EO can also be given in absolute values, calculated as

$$\Delta EO = |EO\ run\ 1 - EO\ run\ 10| = |rel.\ abs._{\ run\ 10}\ (28\ s) - rel.\ abs._{\ run\ 1}\ (28\ s)| \quad (3.11)$$

Considering this description of stability across the spectrum of samples, reductions of 0.06, 0.07 and 0.03 for **2** - **4** respectively, do not appear as dramatic and materials can be understood to behave similarly during multiple bias runs. It is important to keep both representations of the picture in mind as these would be relevant in the application of these materials in different scenarios. For instance, if the material is used for sensing and an event is recorded with different intensity as measured by the EO, changes in the stability of the material will contribute to increasing the noise level, which could eventually lead to poor signal-to-noise ratio (SNR) and an unreliable sensor. Therefore, the relative reduction of the EO can be understood as a parameter in parallel to the SNR, which would become more relevant in a sensing application.

Figure 3.14 shows the response curves of the materials **1** - **4** during bias run 10. In comparison

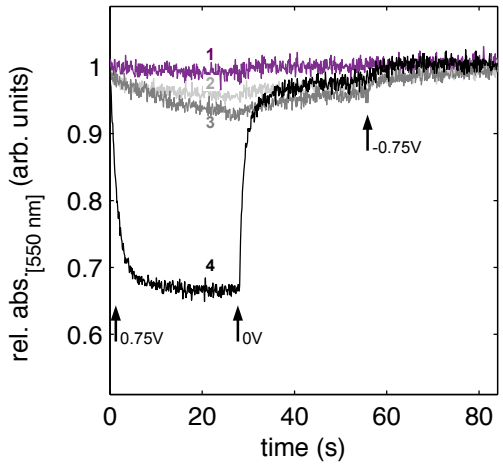


Figure 3.14: Relative absorbance spectra at 550 nm as a function of time with different applied bias: V_{ON} = 0.75 V (0 - 28 s), V_{OFF} = 0 V (28 - 56 s) and V_{REV} = -0.75 V (56 - 84 s) during the bias run 10 (to compare with run 1 in Figure 3.12). **1:** P3HT, **2:** P3HT(C6OH)$_{10\%}$, **3:** P3HT(C6OH)$_{20\%}$ and **4:** P3HT(C6OH)$_{50\%}$.

to the response curves in bias run 1 (Figure 3.12), it can be observed that materials **2** and **3** indeed reduced their EO greatly relative to their initial one, whereas the reduction of EO in material **4** is less apparent due to the larger background EO.

Reversibility of the redox process

Finally, when the bias was returned to 0 V (28 - 56 s), it can be observed that the reversibility of the signal also improved with increasing -OH content. The relative absorbance of **4** rapidly reached its starting value of 1 after the bias was set to 0 V, whereas **2** and **3** showed signs of over-oxidation by remaining at lower values even after 30 s (Figure 3.12).

These results indicate that rational chemical design can assist with controlling bulk ionic transport as more polar compounds showed improved performance, which could also prove promising for other bio-related functions, for example in protein adhesion.

3.3.4 Influence of alkyl chain length

Having demonstrated the profound effect of changing the -OH functionalisation density on ionic transport, a new material **5** was synthesised to investigate the influence of -OH/backbone distance on ionic transport when the material remained with a 50 % -OH loading (Figure 3.1, right). This was achieved by varying the side-chain length on the functionalised monomers from 6 to 11 carbons; the new random co-polymer contained 50 % of 3-(11-hydroxyundecyl)thiophene monomers.

Thin films of **5** displayed a more pronounced 0-0 peak around 602 nm (Figure 3.6), indicating a more aggregated system compared to the shorter side-chain counterpart **4**.

When the material was tested in the same electrochromic setup as the rest of materials (Figure 3.2), it showed a smaller oxidation compared to **4**, as seen in Figure 3.15. However, the doping time-dependency and dedoping profile were both very similar to those of **4**.

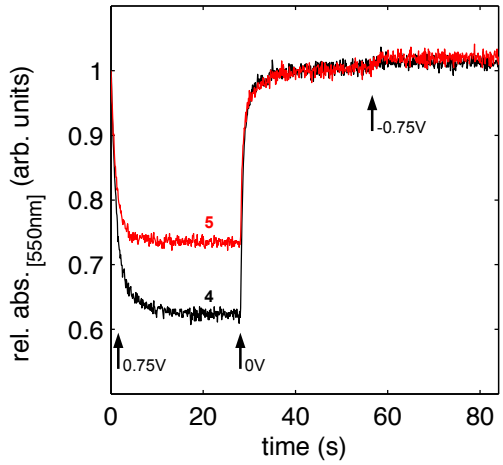


Figure 3.15: Relative absorbance spectra at 550 nm as a function of time during V_{ON} = 0.75 V (0 - 28 s), V_{OFF} = 0 V (28 - 56 s) and V_{REV} = -0.75 V (56 - 84 s). **4:** P3HT(C6OH)$_{50\%}$ and **5:** P3HT(C11OH)$_{50\%}$. The distance between -OH and main chain had an effect in the redox intensity.

The oxidation process time-dependency of **5** was characterised similarly to materials **2** - **4** by calculating t_{80}. Its characteristic time $t_{80,\,5} \approx 2.7\ s$ was comparable to that of **4**, with an associated $t_{80,\,4} \approx 3\ s$. These results suggest a stronger link between ionic transport, related to

oxidation speed, and -OH density than between ionic transport and -OH/backbone distance.

The reduction in the EO indicates that a smaller fraction of thiophenes were oxidised. In other words, a fraction of thiophenes seems to become inaccessible. Several hypotheses are presented here for why this behaviour may occur, but more experimenting is required to draw further conclusions.

The first hypothesis is that the more pronounced aggregation may reduce ionic transport, as there may be a reduction in the interstitial gaps existing in weakly bonded organic materials.[78] In this regard, further experiments in which the microstructure of **5** is manipulated to different degrees of aggregation would shed light to the extent of its influence in its oxidation.

A second possible scenario is that the shielding of thiophenes is related to a particular supramolecular organisation, such as micelles, formed due to the longer side-chains. On one hand, micelles formed by exposing OH-capped alkyl chains and enclosed thiophene backbones could render those (partially or totally) inaccessible to the ions. On the other hand, the exposure of polar -OH groups would explain why the contact angle of thin films of **5** is smaller than that of 4 (Figure 3.7), even though the former contains larger apolar alkyl chains and both contain the same level of -OH polar moieties. A distinction between accessible and completely inaccessible thiophenes may correlate with the unvaried oxidation characteristic time, in the assumption that accessible thiophenes in **5**, which do not belong to micelles and/or aggregates, would oxidise at the same rate as those in **4**.

Finally, there is the possibility that the increasing -OH/backbone length influences the material's ability to oxidise. Although inter-chain interactions (those between the functional group and backbones belonging to adjacent chains) would in principle remain constant, intra-chain -OH/backbone interactions may be hindered by their further distance apart, hence affecting the overall oxidation signal. In this hypothesis the proximity of -OH groups to the thiophene has a role in enhancing the ion-thiophene interaction.

The scenarios depicted above are not mutually exclusive and the possibility of complex interactions is considered, in both the molecular and supramolecular length-scales, playing a role in

the oxidation of the polythiophene derivatives.

3.3.5 Benchmarking with PEDOT:PSS

Material **4:** P3HT(C6OH)$_{50\%}$ displayed a fairly large electrochemical response (Figures 3.10 and 3.12), which seems promising for applications based on electroactive interfaces in aqueous media. In order to provide a benchmark for the results, the operation of P3HT(C6OH)$_{50\%}$ was compared with the material of reference, PEDOT:PSS. The same thin film configuration and measuring setup was used to test the response of PEDOT:PSS. Figure 3.16 displays the characteristic response of both materials and the bias conditions which were tested.

The first observation is that the two materials have different operation mechanisms. While PEDOT:PSS dedopes when a negative bias is applied (also known as depletion mode operation in OETCs), **4** dopes with an applied positive bias, opening new opportunities for a materials platform towards accumulation OECTs.[61]

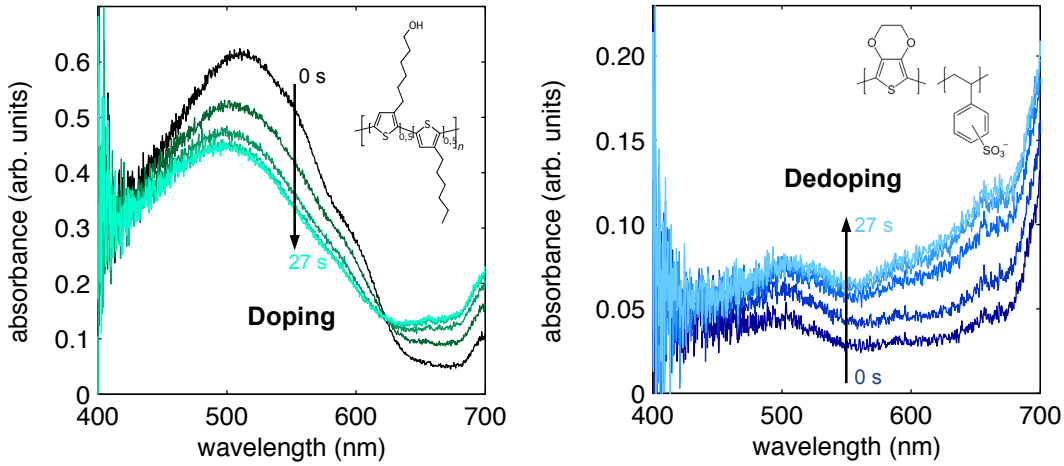


Figure 3.16: Time-resolved absorbance spectra recorded during application of a bias. **Left:** material **4:** P3HT(C6OH)$_{50\%}$. Bias applied +0.75 V. **Right:** PEDOT:PSS. Bias applied -0.75 V. *Spectra shown at times: 0, 1, 3, 9 and 27 s.*

This difference arises from the fact that both semiconductors can be *p*-doped, but the chemical state in which they were used was different. On one hand, PEDOT:PSS is degenerately *p*-doped; upon a negative bias in the setup of Figure 3.2 holes are extracted and the material dedopes. During this process Na^+ ions charge-compensate PSS^- making the material 'switch off' (decrease in conductivity) as described by Bernards et al.[22] This phenomenon is also

observed by the increase in its absorbance (Figure 3.16, right). On the other hand, **4** is initially intrinsic and it becomes electrochemically *p*-doped when a positive bias is applied, reducing its absorbance as this happens (Figure 3.16, left).[4]

The second observation is that the time-response of the two materials is similarly fast, in the order of seconds, which is an interesting feature for future device design employing alternative materials to PEDOT:PSS.

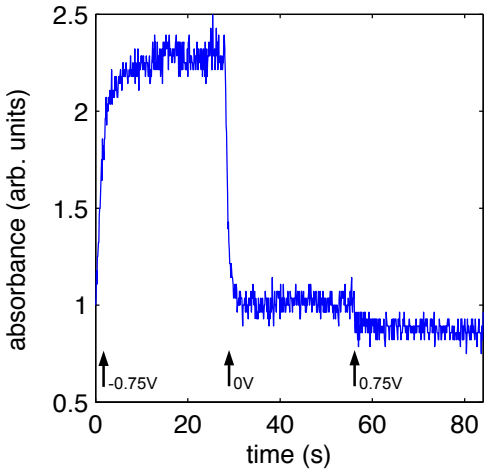


Figure 3.17: Relative absorbance spectra at 550 nm of PEDOT:PSS as a function of time during V_{REV} = -0.75 V (0 - 28 s), V_{OFF} = 0 V (28 - 56 s) and V_{ON} = -0.75 V (56 - 84 s).

A representation of the absorbance at a wavelength over time is shown in Figure 3.17 in order to provide a comparison of the response when the material dedopes initially (0 - 28 s) instead of doping (Figures 3.12 and 3.15).

[4]Note that in the electrochromic setup implemented (Figure 3.2) the Ag/AgCl electrode is grounded and bias steps are applied to the ITO, which is in contact with the semiconductor; this corresponds to a naming convention in similarity to the electrochemistry field. However, OECTs follow transistor devices naming conventions by placing their ground at the source and applying the (gate) voltage at the Ag/AgCl.

3.4 Conclusions

This chapter focused on the scrutiny of new instrinsic polymers as mixed ionic/electronic conductors, and has demonstrated their ability to act as ion-to-electron transducing interfaces in aqueous media. The approach taken in characterising systems functionalised with polar groups via co-polymerisation offers a versatile approach to the chemical design of materials for bioelectronics.

A range of co-polymers was screened and showed that the density of the covalently attached -OH groups affects the hydrophilicity of the polymer, as shown by water contact angle. Despite the strong effect observed in the polarity of the films, the choice of a small moiety maintained appropriate charge transport in the polymer derivatives. Most importantly, the electroactivity of the polymers in a water electrolyte was controlled by the number of polar -OH units, achieving highly responsive materials in suitable bias conditions with enhanced ionic transport. In fact, the response time of the more hydrophilic of the polythiophene derivatives was comparable to that of PEDOT:PSS.

As well as showing the effect of -OH group density on ionic transport, this work has also provided insight into further design rules that manipulate the response of such ion-to-electron transducing materials; the moiety-to-backbone distance was manipulated by changing the length of the alkyl chain to which -OH groups were attached, which affected the intensity of the oxidation. Increased distances caused the extent of the response to reduce.

The direct correlations observed between the number of -OH polar moieties and their position relative to the backbone with the electroactivity of such derivatives suggests a possible chemical design rule that could be extended to other materials possessing a range of functions interesting for bioelectronics. For example, having the means to tune the ion uptake and transport in materials based on the broad class of organic semiconductors designed for light-emitting diodes, solar cells and thin-film transistor applications may open up new avenues towards devices featuring new optoelectronic functions in the field of bioelectronics. Alternatively, -OH groups could be used to enhance ionic transport in ion-selective membranes, providing faster response

systems.[90] Other fields could also benefit, for instance optogenetics, from materials with specific optical properties of absorption/emission that are also responsive to the ionic cell signals, since these could provide cell-tailored responses.

Chapter 4

Semiconductor/insulator blends as mixed (electronic/ionic) conductors

4.1 Introduction

One of the most relevant characteristics that makes organic semiconductors highly appealing in bioelectronics is their capability to sustain ionic and electronic transport within their bulk.[78] In such complex conducting materials, engineering the contribution of each charge carrier type by means of new materials and/or processing strategies is of key importance for advancing the field. Furthermore, understanding which parameters affect ionic transport in model organic semiconductors can lead to breakthroughs in the rational design of new materials.

As has already been discussed, in the last decade PEDOT:PSS was the most broadly used organic semiconductor in the field of bioelectronics. PEDOT derivatives are the only systems in the literature whose ionic transport properties have been studied in more detail. Stavrinidou et al.[91,80] designed a model and calculated the ion mobility of various PEDOT systems and correlated enhanced mobilities with increasing swelling. In PEDOT:PSS swelling was manipulated by crosslinking with the aid of GOPS; crosslinked systems showed systematically reduced ion mobilities. In a different study, a hydrophilic phase consisting of gelatin was added during vapour phase polymerisation of PEDOT:TOS; gelatin increased the hydrophilicity and swelling capability of PEDOT:TOS, which translated into larger values of ion mobility.[81]

This last example, in which a secondary gelatin phase was added to the organic semiconductor, already points out that certain challenges cannot be fulfilled by a single material, including appropriate mixed transport. Multicomponent semiconducting polymer systems appear in the literature as a strategy to provide a wide range of functions.[92,93] Some examples of relevant added functions found in organic bioelectronics are:

- *Mechanical properties for closer matching to body tissues.* Although organic semiconductors represent a softer option than their inorganic counterparts, their relatively brittle nature and fragile surfaces still demand improved structures.[94] The general approach to improve such properties is to produce mixed architectures of hydrogel/conducting polymer, either in a blend or layered structure,[28] or elastomer/conducting polymer.[26]

- *Covalent attachment of relevant biomolecules.* Exposure of biological cues is of key importance for generating specific interactions at the polymer/cell interfaces. However, the modification of the semiconductor for such purpose can compromise its charge transport capabilities.[95] An example study bipassed this issue by incorporating a secondary matrix of PVA to PEDOT:PSS and using it as chemical anchor to surface-functionalise with a biomolecule.[60]

- *Enhanced charge transport.* In the case of PEDOT, the addition of a tertiary component (in which case PSS or TOS is considered the secondary phase) is very commonly found in the literature. Examples with PEG and PVP have been shown to enhance both electronic and ionic transport.[77,96] As previously mentioned, gelatin has been used as a tertiary component of PEDOT:TOS as a tool to enhance ionic transport.[81]

In Chapter 3, a new class of polythiophene derivatives was explored, which displayed desirable responses as ion-to-electron signal transducers, and which proved to be adequately controlled by means of co-polymerisation. In this chapter the incorporation of a polar insulator to the most responsive of the polythiophene derivatives, P3HT(C6OH)$_{50\%}$, is investigated. Blending of a polar phase with organic semiconductors, generally of very apolar nature, is by itself a challenge which can be in some cases overcome by means of suitable processing techniques. The structure formation and transport properties were studied, both electronic and ionic, of the multiple blends identifying specific transport components related to the addition of the insulator. Furthermore, this model semiconducting material was used to control its microstructure and gain insight in the influence of order (at specific length-scales) on ionic transport.

The experiments presented in Sections 4.3.1 and 4.3.5 were partly performed by Murielle Schreck as part of her master project, which I helped design and supervise. Figures and sketches were adapted from her work. The AFM experiments presented in the same section (4.3.1) were performed with the kind help of Nadav Ambdursky (Department of Materials, Imperial College London).

4.2 Materials and methods

Blends of P3HT(C6OH)$_{50\%}$ and a choice of two polar insulators, PVA and a PMMA acid derivative (MMAcoMAPC1), were prepared via solution processing (Figure 4.1). P3HT(C6OH)$_{50\%}$ (mass-average molecular weight M_w = 63000 g/mol, dispersity Đ = 1.82) was synthesised and provided by Dr Olivier Dautel (AM2N Laboratory, Charles Gerhardt Institute, France). High molecular weight PVA was purchased from Sigma-Aldrich (M_w = 146000 - 186000 g/mol, 87 - 89 % hydrolysed) and used as received. MMAcoMAPC1 was purchased from Specific Polymers (M_w = 18000 g/mol, reference SP-4P-1-003) and used as received.

All polymer solutions were prepared at a concentration of 8 mg/ml and heated while stirring at 58 °C on a hotplate for a minimum of 2 h until full dissolution; vials were fitted in a metal chuck in order to ensure homogeneous heating. All solutions were freshly prepared and used within a window of 3 h after dissolution.

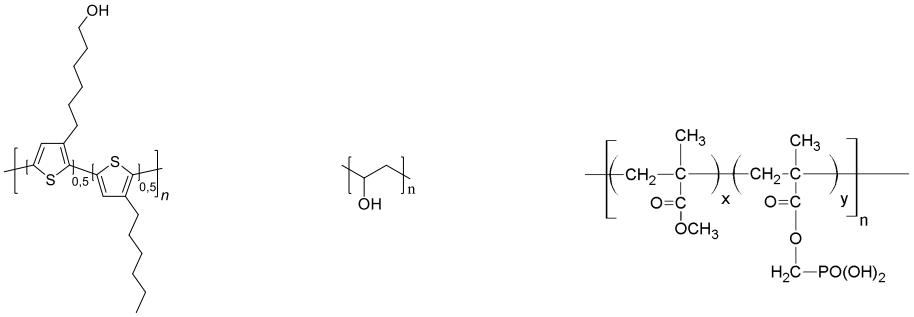


Figure 4.1: Chemical structures of polymers. **Left:** OH-containing derivative poly(3-hexylthiophene)-co-(3-(6-hydroxyhexyl)thiophene) (P3HT(C6OH)$_{50\%}$). **Centre:** poly(vinyl alcohol) (PVA). **Right:** PMMA phosphonic acid derivative (MMAcoMAPC1) (x = 0.9, y = 0.1).

4.2.1 Blends containing MMAcoMAPC1

A co-solvent was used for the preparation of P3HT(C6OH)$_{50\%}$:MMAcoMAPC1 blends. Both polymers were dissolved in tetrahydrofuran (THF) in separate vials. When full dissolution was achieved, blends of various ratios (wt%) were prepared by pipetting the appropriate volume ratios in a separate vial. Blends were kept being stirred on the hotplate until film deposition.

Blend thin films were prepared on glass or ITO substrates, depending on the characterisation required, following the protocol described in Section 2.1.

One experiment was performed to observe differences in the microstructure formation when P3HT(C6OH)$_{10\%}$ was blended instead of P3HT(C6OH)$_{50\%}$. In this case, in order to prepare blends of P3HT(C6OH)$_{10\%}$:MMAcoMAPC1 the solvent mixture toluene:cyclohexanone 1:3 v/v% was used. This solvent mixture was selected based on the affinity of both components to each solvent, P3HT(C6OH)$_{10\%}$ to toluene and MMAcoMAPC1 to the more polar cyclohexanone. Films were prepared on glass following the standard protocol described in Section 2.1, with the difference of higher casting temperature T_{cast} = 50 °C due to the higher boiling point of both mixture solvents.

4.2.2 P3HT(C6OH)$_{50\%}$:PVA blends - solvent choice

A solvent mixture was used for the preparation of P3HT(C6OH)$_{50\%}$:PVA blends. Two polar organic solvents, tetrahydrofuran (THF) and dimethylsulfoxide (DMSO), were selected to ensure full dissolution of both components independently prior to blending at various ratios. Solvent volume ratio was kept at 2:1 v/v% THF:DMSO for all blend ratios.

Polymer dissolution was done independently, initially dissolving each polymer in the better solvent for them: DMSO for PVA and THF for P3HT(C6OH)$_{50\%}$. PVA was firstly dissolved in the corresponding volume of DMSO; when the solution was transparent the according volume of THF was titrated ensuring no cloudiness appeared in the process. Similarly, P3HT(C6OH)$_{50\%}$ was firstly dissolved in THF, subsequently adding the corresponding volume of DMSO.

Blend thin films were prepared on glass or ITO substrates, depending on the characterisation required, following the protocols described in Section 2.1. Film thickness for blends of ratios 100:0 to 50:50 wt% ranged from 110 - 145 nm (relative error $<$ 15 %) when 1 layer was cast, and from 235 - 280 nm (relative error $<$ 18 %) when 2 layers were cast. Films of 100:0 wt% were on the thin end of the range, whereas 50:50 wt% were on the thicker end.

4.2.3 Sample preparation for DSC

Differential scanning calorimetry was performed on a Mettler-Toledo DSC 1 Star^e system. Films were prepared in a multi-layer fashion (up to 4 - 5 layers/sample) following the same casting protocol as for all other thin film characterisation of the blend system (Section 2.1). This approach of casting multiple thin films per sample instead of drop casting an equivalently thick one ensured the achievement of samples having a more similar microstructure as those used to characterise the blends' transport. Following 24 h in vacuum in order to remove residual solvent, films were scratched from the substrate and encapsulated into a DSC pan. Two samples of each material composition were measured in the same conditions (Section 2.3); one representative plot is presented in the results section (4.3.1).

4.2.4 Sample preparation for contact angle of top/bottom surfaces

In order to test the hydrophilicity of both top and bottom interfaces of P3HT(C6OH)$_{50\%}$:PVA blends, films were deposited on glass as described in Section 2.1. In order to delaminate the films, the samples were soaked overnight using distilled water contained in a PDMS well. After $\approx$ 20 h the water was removed and the PDMS stamps were swiftly lifted, peeling the films off the glass substrate. Figure 4.2 depicts a sketch of the delamination process. All samples were soaked for $\approx$ 20 h before measuring top-surface contact angle in order to ensure appropriate comparison between top/bottom measurements.

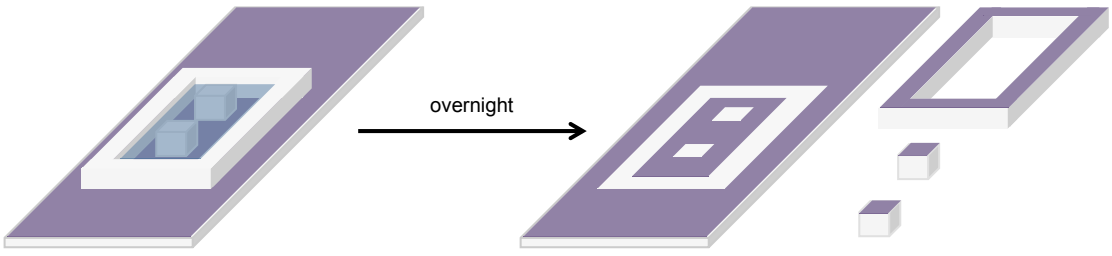


Figure 4.2: Sketch of polymer films on glass peeled off with the aid of a PDMS stamp. Water is contained in the larger PDMS stamp, acting as a well. Other smaller stamps were placed within the inside area, providing more samples for bottom interface contact angle. *Sketches adapted from Murielle Schreck's MSc thesis.*

4.2.5 Real-time electroactivity: advanced data handling

Details of the measuring setup and initial data handling/representation can be found in Section 3.2.4. Based on the understanding that oxidation processes typically show exponential dependency with time, the characteristic decay rate(s) were found.

Consider the simplest example in which the absorbance is described by a single decay. The absorbance as a function of time will be referred to as $y(t)$. The dependency of y with time in this case is

$$y = y_0 + y_1 e^{-k_1 t} \tag{4.1}$$

where y_0 and y_1 are fitting coefficients specific to experimental decays. In order to extract k_1 a typical approach is to plot the data on a semi-logarithmic scale, so that the data points can be fitted to a straight line of slope k_1. Alternatively, an appropriate transformation of the variables can move the non-linear regression to the linear domain. For the last case, the data handling process starts with the normalisation of y between 0 - 1. The dependency with time of the new variable defined, y', is

$$y' = \frac{y - y_0}{y_1} = e^{-k_1 t} \tag{4.2}$$

When its natural logarithm is plotted against time, the relation between the new variable and time is

$$ln\,(y') = -k_1 t \tag{4.3}$$

and so a linear behaviour with slope $-k_1$ can be observed on a plot of $ln\,(y')$ vs. t.

In the more general case of multiple exponential decays, the dependency with time of the absorbance is

$$y = y_0 + \sum_{i=1} y_i e^{-k_i t} \tag{4.4}$$

and the landscape becomes more complicated. However, the general observation after a similar variable transformation will be a multi-linear plot over time, in which faster decays, with steeper slopes, are visible at earlier stages, followed by slower ones.

Therefore, to find the time constant(s) characteristic(s) of the oxidation, the relative absorbance during the doping process (0 - 28 s) was transformed similarly to the example and plotted as a function of time. As shown in the example, the data was normalised between 0 - 1 (Equation 4.2) prior to applying the natural logarithm (Equation 4.3). Since the relative absorbance in the time range 0 - 28 s always started at 1 and decreased reaching its minimum (of ≈ 0.5) at t = 28 s, the maximum and minimum absorbance limits for normalising the data were taken at time points 0 and 28 s, respectively.

$$Ln\ (norm.\ abs) = ln\left(\frac{rel.\ abs._{\ [550nm]}\ (t) - rel.\ abs._{\ [550nm]}\ (28)}{rel.\ abs._{\ [550nm]}\ (0) - rel.\ abs._{\ [550nm]}\ (28)}\right) \tag{4.5}$$

The transformed variable $Ln\ (norm.\ abs)$ was then plotted as a function of time. When multi-linear regimes were observed, fitting to multiple straight lines was done by selecting the time range according to best fits.

4.3 Results and discussion

4.3.1 PVA blends: solid state structure

Crystallisation driven solidification

The ability of PVA to support ionic transport has been used to implement it as a solid state electrolyte in lithium ion batteries.[97,98] Along with its hydrophilic nature and swelling capabilities, these characteristics make of PVA an interesting material for systems aiming to sustain mixed transport in hydrous environments.

When working with binary systems, microstructure formation during solvent evaporation can be controlled by multiple phenomena. Some examples containing organic semiconductors have shown liquid-liquid phase separation[99] and the use of nucleating agents to control crystal formation[100] as strategies to achieve desirable length-scale phase separation. For materials systems that support mixed transport, aiming at a bicontinuous network of both polymer phases would support electronic/ionic transport within the bulk of the system, assisted by the semiconductor/insulator phases, respectively.

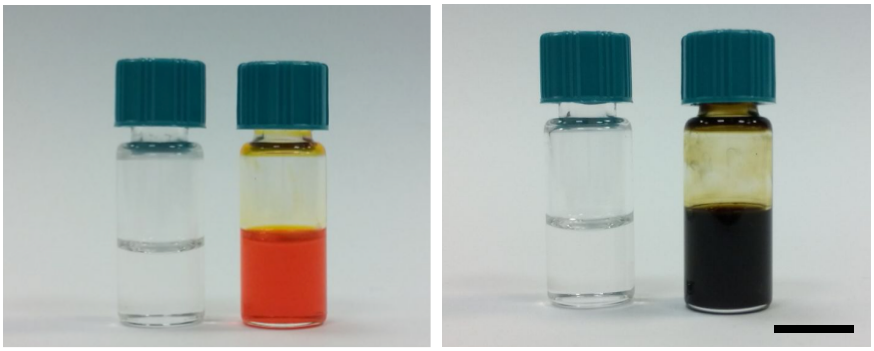


Figure 4.3: Pictures of vials containing solutions of PVA (left) and P3HT(C6OH)$_{50\%}$ (right), 8 mg/ml in THF:DMSO 2:1 v/v%. **Left:** At 58 °C, both solutions are clear showing dissolution of both materials. **Right:** At RT, PVA remains dissolved whereas P3HT(C6OH)50% becomes brown due to a solid solute phase appearing due to poorer dissolution. *Scale-bar*: 1 cm.

In order to achieve low-percolation blends, meticulous solvent selection is required to give preference to the insulator dissolution, allowing the crystallisation of the semiconductor to

occur in the first place.[101] By using THF:DMSO 2:1 v/v% as the solvent, PVA solutions remained as homogeneous single phase systems at room temperature, whereas P3HT(C6OH)$_{50\%}$ solutions resulted in two phases (crystalline solute and liquid solvent/solute phases) as clearly indicated by the dark brown colour of the solution (Figure 4.3). These observations point to the correct direction in order to achieve a percolating network of semiconductor during solid state formation.

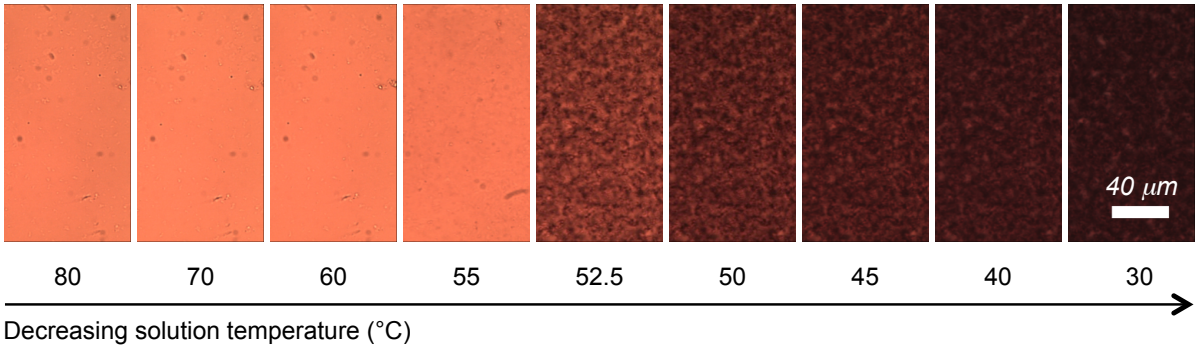


Figure 4.4: Optical micrographs of an encapsulated solution of P3HT(C6OH)$_{50\%}$:PVA (50:50 wt%) in THF:DMSO 2:1 v/v % (concentration c = 8 mg/ml total polymer content). The solidification process of the blend is dominated by the crystallisation of the semiconductor P3HT(C6OH)$_{50\%}$ as shown in the optical micrographs of the heated solution when the temperature decreases from 80 °C to 52.5 °C.

Similarly to Hellmann et al.,[99] the crystallisation process in a blend solution of 50:50 wt% ratio was analysed. The surfaces were optically examined while varying the temperature of the solution. The solution was fully dissolved at 80 °C and the temperature was decreased in a stepwise fashion, imaging after a few seconds on each temperature step when the microstructure showed no changes. As expected by the dissolution differences previously observed (Figure 4.3), the solidification process of P3HT(C6OH)$_{50\%}$:PVA blend was dominated by the initial crystallisation of the semiconducting phase P3HT(C6OH)$_{50\%}$ which takes place prior to PVA solidification (Figure 4.4). Such crystallisation phenomena is expected to also happen during film formation, when solvent evaporation takes place.

Influence of blending on the crystallinity of polymer blend

Differential scanning calorimetry (DSC) was used to provide quantitative information of the phase transitions of the materials based on their experienced thermal transitions. DSC was run on multi-layer thin film samples of varying blend ratios (P3HT(C6OH)$_{50\%}$:PVA wt%, Figure 4.5). Thermograms of the blends display two distinct melting peaks, which correspond to each individual blend component: $T_{m,PVA} \approx 195$ °C and $T_{m,P3HT(C6OH)_{50\%}} \approx 224$ °C (as obtained from the melting peak of each neat material). A peak around 55 °C is associated to remaining solvent THF, even though samples were stored in vacuum for ≈ 24 h. The amount of THF is correlated to the presence of PVA, as seen by the more pronounced peak, which suggests a stronger adsorption of THF to the polar insulating polymer than to P3HT(C6OH)$_{50\%}$.

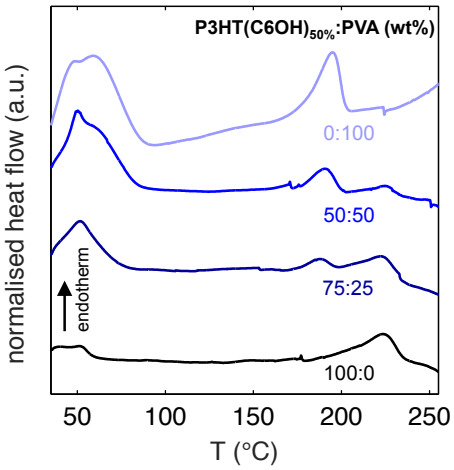


Figure 4.5: Differential scanning calorimetry (DSC) performed of P3HT(C6OH)$_{50\%}$:PVA blends, from multi-layer thin films. First heating cycle thermograms at varying wt% ratios display the melting of both P3HT(C6OH)$_{50\%}$ and PVA.

The melting enthalpies of each component (P3HT(C6OH)$_{50\%}$ and PVA) were calculated by integrating the area under the respective melting peak and normalising to the mass of each material component within the blend component mass (Figure 4.6, left). A decrease in the specific melting enthalpy was observed for both the semiconductor and the insulator as their fraction was lowered within the blend. This indicates a reduction in crystallinity of both polymers when in presence of a second component.

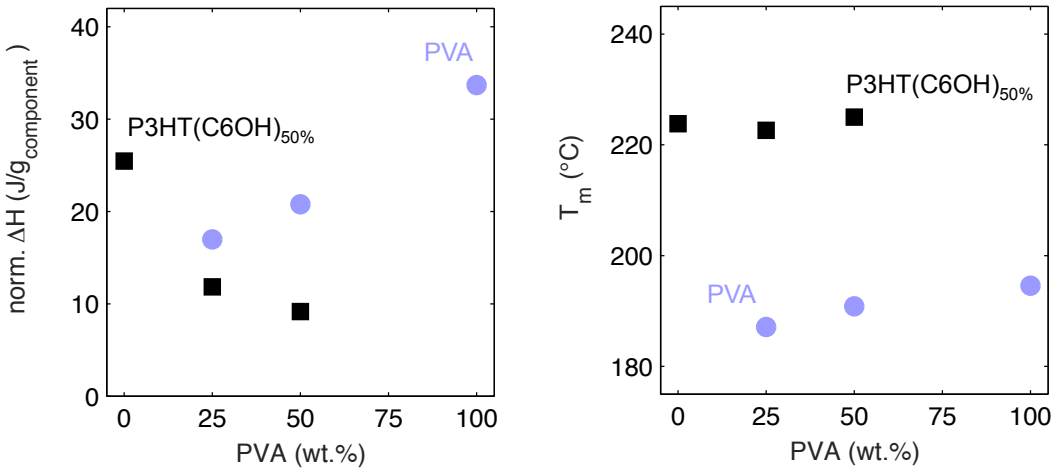


Figure 4.6: **Left:** Melting enthalpies of P3HT(C6OH)$_{50\%}$ and PVA in blend systems normalised to the mass of each polymer component within the blend. **Right:** Peak melting temperatures of P3HT(C6OH)$_{50\%}$ and PVA. Crystallinity of both components is reduced upon blending. Some interaction between the components is suggested by the melting peak depression of PVA.

The peak melting temperature was also calculated for each individual component and plotted as a function of blend ratio (Figure 4.6, right). Although the melting temperature of P3HT(C6OH)$_{50\%}$ remains constant at varying blend ratios, the PVA melting peak is depressed in the presence of P3HT(C6OH)$_{50\%}$. This observation suggests a certain degree of miscibility between both components, which is not surprising, as an interaction between the polymers is expected to take place between the polar moiety of P3HT(C6OH)$_{50\%}$ (-OH unit) and the polar PVA, potentially by means of H-bonding and other Van der Waals forces; this interaction would depress the melting temperature of PVA. The reason for not observing such an effect in P3HT(C6OH)$_{50\%}$ may be related to the fact that only the melting of the aromatic stacking part of the polymer contributes to its melting transition, since the alkyl chains melt at much lower temperatures. Hence any interactions affecting the alkyl part of the polymer will not contribute to the melting phase transition.

Vertical phase separation

Due to the inherently different polar nature of both polymers, certain vertical phase separation could not be excluded due to different affinity of the polymers to the substrate. In order to determine whether some enrichment of the insulating phase takes place at the bottom (or top) interface, assessment of the hydrophilicity of both interfaces was done by measuring water contact angle on them. Although this technique does not allow a quantitative analysis of the degree of segregation, it renders valuable information regarding the structure of the blends.

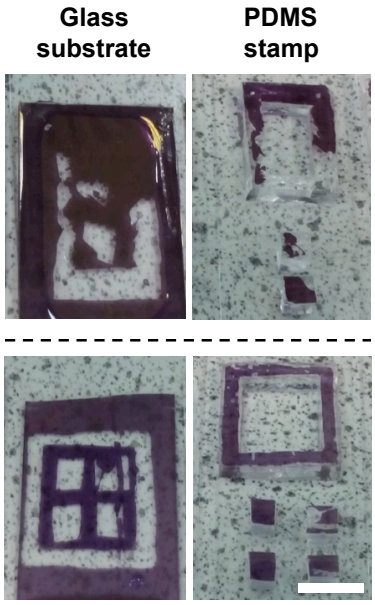


Figure 4.7: Examples of polymer films on glass peeled off with the aid of a PDMS stamp. **Top:** neat P3HT(C6OH)$_{50\%}$. **Bottom:** P3HT(C6OH)$_{50\%}$:PVA 50:50 wt% blend. *Scale-bar*: 1 cm.

Films were delaminated following the procedure described in Section 4.2.4; as shown by the sketch in Figure 4.2, films deposited on glass were peeled off using a PDMS stamp. One example of the peeled films is shown in Figure 4.7. Generally, blend films delaminated in larger areas, which may be related to hydrophilic PVA aiding the detachment from the glass upon swelling during the overnight soaking in water.

Contact angle measurements performed on the top and bottom interfaces of blend films suggested that more PVA was present at the bottom surface (Figure 4.10). The enrichment is evidenced by the decreasing contact angle upon PVA addition at the bottom surface, whereas a

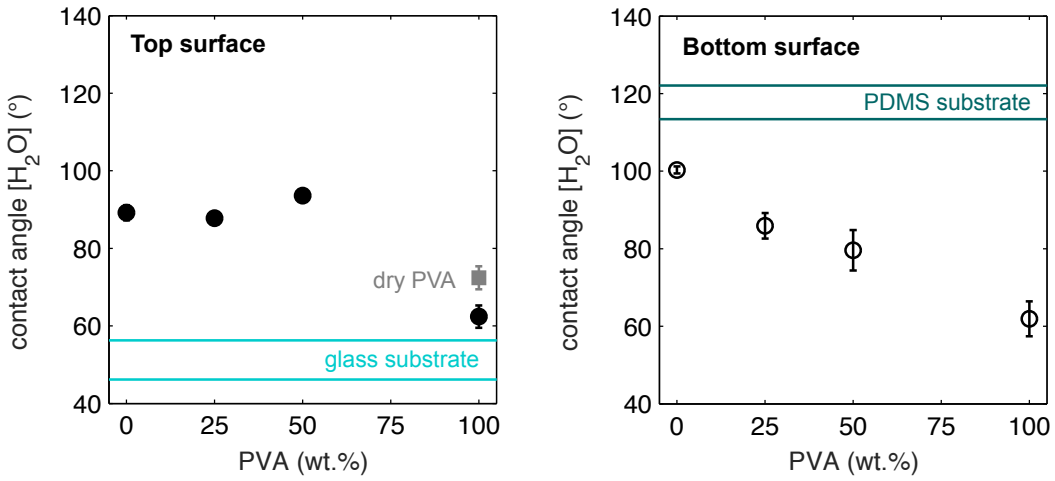


Figure 4.8: Contact angle of water on the top and bottom surface of blend films. **Left:** Top surface displayed a constant contact angle despite the addition of PVA. **Right:** Contact angle of the bottom surface decreased upon PVA loading, which indicates an enrichment of PVA at the bottom surface during solvent evaporation and drying. Data is presented along with the contact angle of the controls: glass and PDMS, which acted as substrates in each measurement. For completion, the contact angle of a dry PVA film (no soaking overnight) is shown.

constant trend is observed at the top surface as PVA loading increases. A similar behaviour had previously been observed in blends of P3HT with PMMA, where strong vertical phase separation produced a distinct PMMA/P3HT bilayer structure.[102] Nonetheless, less segregation is expected for P3HT(C6OH)$_{50\%}$:PVA blends, owing to closer surface tension values among the two; surface tension values from literature indicate γ(PVA) $\sim$ γ(PMMA) and γ(P3HT(C6OH)$_{50\%}$) $>$ γ(P3HT), which was evidenced by smaller water contact angle of the -OH functionalised polythiophene (Figure 3.7).[103]

Surface morphology in water

Since in any bioelectronics application films will be immersed in solution, it is of prime importance to characterise their microstructure in the wet state. Atomic force microscopy (AFM) was used to image the film morphology in air ('dry state', Figures 4.9 **a** and 4.9 **b**) in comparison to when it was immersed in water ('hydrated state', Figures 4.9 **c** and 4.9 **d**).

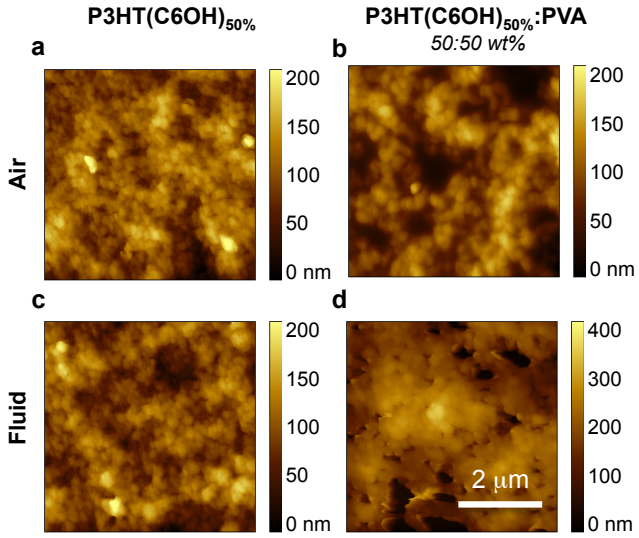


Figure 4.9: Atomic Force Microscope (AFM) images in air of: **a)** neat P3HT(C6OH)$_{50\%}$ and **b)** P3HT(C6OH)$_{50\%}$:PVA blend. Topography of films in fluid is also shown: **c)** neat P3HT(C6OH)$_{50\%}$ and **d)** P3HT(C6OH)$_{50\%}$:PVA blend. Clear swelling is observed in PVA-containing system (note the doubling on the scale, indicating an increase in the volume of PVA). Similar granular structures are observed in air for neat semiconductor and semiconductor:insulator blend systems, seemingly due to the solidification process dominated by the aggregation of the semiconductor.

In the dry state similar feature sizes were observed both in the neat and blend films, which correlated directly to the microstructure formed by the semiconductor solidification for all blend ratios (Figure 4.4). The roughness average, R_a, mildly increased upon addition of PVA, from (24 ± 3) nm of the neat film to (36 ± 9) nm of the blend. When the films were subsequently placed in water and fluid AFM was performed, remarkable swelling was observed only for the blend film (Figure 4.9 **d**), whereas the neat film did not show any change (Figure 4.9 **c**). Swelling can be visualised by the smoother and inflated features, but mostly from the dramatic increase in the scale of the image to twice the height upon wetting (from panel **b** to **d**).

Film stability in water

The use of semicrystalline polymers in blends has proven to enhance the system's stability, e.g. mechanically, in air and for longer-term device performance.[93] In this context, certain chemical features of PVA were selected to produce water stable blends with P3HT(C6OH)$_{50\%}$: relatively low levels of hydrolisation (87 - 89 % hydrolysed) in order to process it from organic - yet very polar - solvents which would also solubilise P3HT(C6OH)$_{50\%}$; and also high molecular weight (M_w = 146000 - 186000 g/mol) in order to promote polymer chain entanglements, with the vision of conferring stability to the blend system, primarily in aqueous media.

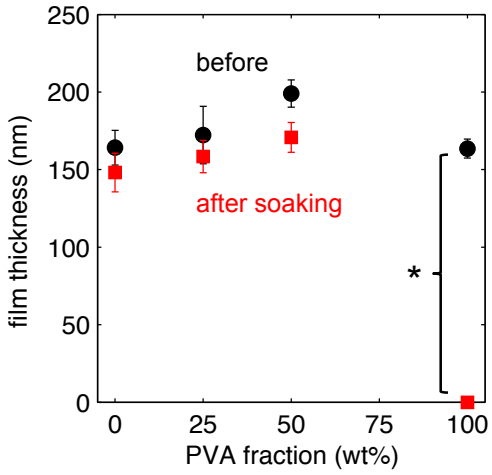


Figure 4.10: Film thickness of P3HT(C6OH)$_{50\%}$:PVA blends as cast and after 24 h immersed in NaCl water electrolyte. Film loss is significant for the neat PVA film, comparison made using paired student's t-test; $*$ significant at $p < 0.05$.

The stability of films was tested by measuring their thickness before and after 24 h soaking in a NaCl water electrolyte. The comparison between samples before-after soaking was done using paired student's t-test; differences are significant for $p < 0.05$. The mean film thickness showed reductions of 9.8 %, 8.1 %, 14.2 % and 100 %, for films containing 0, 25, 50 and 100 wt% PVA, respectively. These results show a trend of increasing dissolution with the load of PVA before-after soaking in the water electrolyte, however only neat PVA showed significant differences which may be due to the small number of samples tested (n = 2). Neat PVA films were the most extreme case, since no film was found after soaking even when attempting to

make new scratches at difference areas of the film.

In summary, the use of high molecular weight, low hydrolysation PVA resulted in blend films which remained stable in water within the limits of the stability test performed. The stability in blends including PVA, without the use of chemical crosslinking, outperform those in literature of water soluble polymers. For example, nanofibre membranes including 50 wt% of water soluble poly(vinyl pyrrolidone) (PVP) exhibited mass losses of 37 %, larger than the equivalent loss of our 50:50 wt% blend.[104]

4.3.2 Electronic transport

As explained in Section 4.3.1, the fabrication of percolating blends was one of the aims in order to maintain the functions of the semiconducting phase, which is highly reliant of connecting pathways in order to support charge transport. The films' ability to transport holes was scrutinised by measuring their conductivity in ambient conditions in a 4-point configuration for a range of blend ratios. The presence of an in-plane percolating path at different concentrations of PVA was evidenced by the conductivity of the system remaining almost independent of the blend ratio (Figure 4.11). Even at high PVA loading conductivity stays unchanged, which may be due to the formation of fibrils of P3HT(C6OH)$_{50\%}$ that interconnect within the volume of the blend. The 4-point measurements performed for 75 and 90 wt% PVA films showed a transient behaviour, being unstable to the test currents after a few seconds. Hence, further characterisation was focused on systems containing up to 50 wt% PVA.

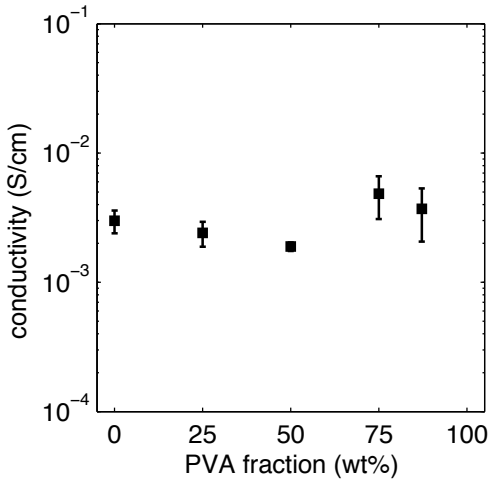


Figure 4.11: Conductivity of P3HT(C6OH)$_{50\%}$:PVA blends measured in a 4-point probe setup. Films were deposited on glass and measured in ambient conditions.

PVA is an insulating polymer and no measurement of its conductivity could be done within the measuring limitation of the 4-point setup. An attempt of 2-point measurement was done using an MMR probe station, with sensitivity in the pA, and separation between the measuring electrodes up to 2.5 μm; no measurable current was achieved, hence a nominal nil conductivity is considered for neat PVA.

4.3.3 Ionic transport

The role of organic semiconductors as interfaces that translate ionic-to-electronic signals, and vice-versa, is central in bioelectronic applications and it depends on their ability to sustain both ionic and electronic transport. Following the critical test confirming the blends' ability to transport holes (Figure 4.11), it was important to learn about ionic transport in the presence of the insulator PVA.

As presented in Chapter 3 (methods in Section 3.2.4 and results in Section 3.3.3), by tracking the real-time electrochemical doping/dedoping of the *p*-type polythiophene derivatives, the speed of ions that migrate from the electrolyte in order to compensate the extracted electrons could be qualitatively compared. In the same fashion, the effect of the electrically inert PVA phase in the blends' ionic transport was examined.

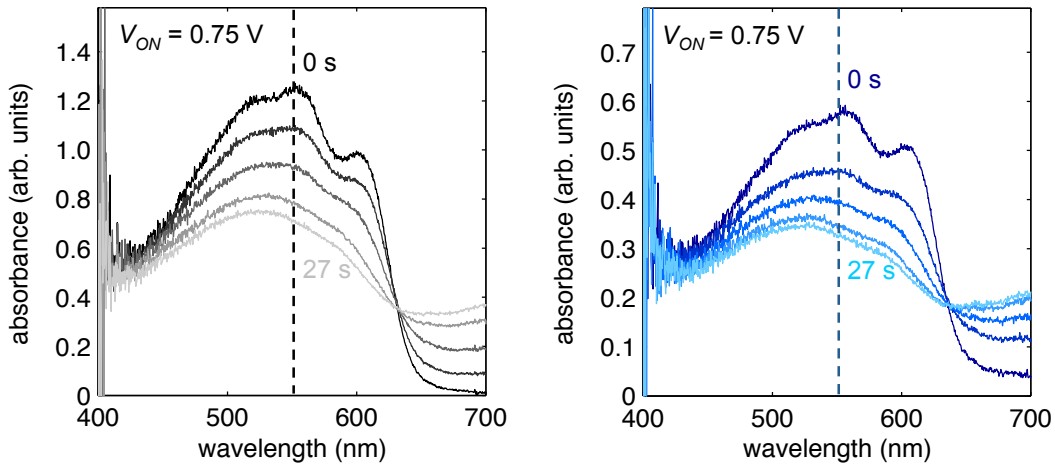


Figure 4.12: Real-time visible absorbance spectra of thin polymer films when a bias V_{ON} = 0.75 V is applied in the setup displayed in Fig. 3.2. **Left:** neat P3HT(C6OH)50%. **Right:** P3HT(C6OH)$_{50\%}$:PVA (50:50 wt%) blend, displaying a faster response. Spectra at times 0, 1, 3, 9 and 27 s are displayed.

As before, the measurements started at 0 V followed by: V_{ON} = 0.75 V (0 - 28 s), V_{OFF} = 0 V (28 - 56 s) and a reverse bias V_{REV} = -0.75 V (56 - 84 s). Fast full visible absorbance spectra (wavelength 400 - 700 nm) were recorded for the duration of each step voltage (V_{ON}, V_{OFF} and V_{REV}), every 100 ms. Upon application of V_{ON}, the doping of P3HT(C6OH)$_{50\%}$ was

observed by the change of its absorbance spectra over time (Figure 4.12, left). The addition of PVA appeared to make the oxidation process happen faster (Figure 4.12, right). The films tested were of similar thicknesses (see Section 4.2.2), hence the absorbance spectrum before oxidation was reduced approximately by half when the blend system contained 50 wt% PVA, as the latter is optically transparent.

In order to better compare the influence of PVA in the dynamics of the full doping/dedoping process, the relative absorbance at a wavelength of 550 nm was plotted as a function of time (Figure 4.13).

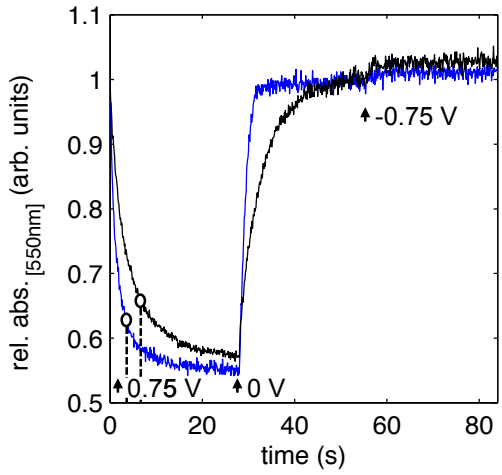


Figure 4.13: Relative absorbance spectra at 550 nm as a function of time during V_{ON} = 0.75 V (0 - 28 s), V_{OFF} = 0 V (28 - 56 s) and V_{REV} = -0.75 V (56 - 84 s) of (**black**) P3HT(C6OH)$_{50\%}$ and (**blue**) P3HT(C6OH)$_{50\%}$:PVA (50:50 wt%) blend. Faster response is observed for PVA-containing system; the exponential nature of the response can be clearly observed. An empty circle indicates the point where t_{80} is reached for each material.

Clearly, the incorporation of PVA accelerated the oxidation process, which occurred during the positive step voltage (V_{ON}, 0 - 28 s). When the system was returned to 0 V (V_{OFF}, 28 - 56 s), the semiconductor dedoped and the subsequent release of ions to the electrolyte was also much faster in the presence of PVA. In fact, for all the systems a faster behaviour was observed during dedoping (V_{OFF}) compared to doping (V_{ON}), which may be related to the fact that during the doping process, ions are required to travel from the electrolyte into and through the polymer bulk before reacting on a redox site; whereas during dedoping the sole detachment

from the redox site will provide the spectral signal, hence not accounting for the time required for the ion to fully return to the electrolyte. Hence, the study of the oxidation was considered to provide a closer indication of the ionic transport characteristics within the polymer bulk.

Remarkably, it was observed that for the blend most of the Cl^- ions were released within a few seconds, whereas for the neat P3HT(C6OH)$_{50\%}$ a small amount remained trapped and a reverse bias (V_{REV}) was needed as a driving force to expel them, which is evidenced by the step at the profile appearing in the transition from V_{OFF} to V_{REV} at 56 s.

To have a more quantitative comparison between the neat and blend system during the oxidation process, t_{80} was defined as the measured time for reaching 80 % of the maximum extent of oxidation during V_{ON} (further description in Section 3.2.4), which can give an indication of whether a systematic reduction in the time response takes place upon PVA loading (Figure 4.14).

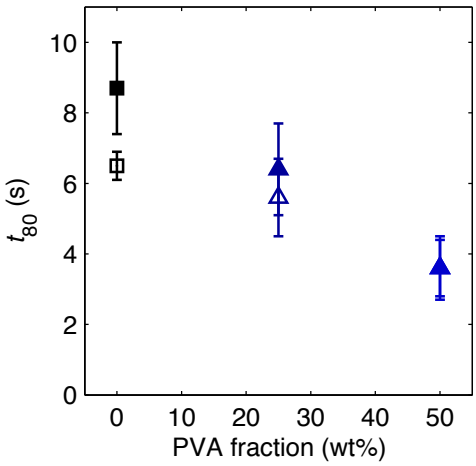


Figure 4.14: Oxidation time response, t_{80}, defined as the time to reach 80% of maximum oxidation attained by each sample. Time t_{80} during V_{ON} is displayed for (**black**, square) the neat P3HT(C6OH)$_{50\%}$ and (**blue**, triangular) P3HT(C6OH)$_{50\%}$:PVA blends. *Empty symbols:* first bias run. *Solid symbols:* tenth bias run.

Indeed, time t_{80} reduces consistently with the addition of PVA in blends (blue) compared to the neat P3HT(C6OH)$_{50\%}$ (black). This reduction is attributed to an increase in the ion mobility within the polymer bulk. Ion mobility in conducting polymers has previously been reported

to achieve values close to those in water when the system was highly swelled.[81] However, even for such efficient ion conductors, the ion mobility remained much lower than that of holes, meaning that the oxidation process was limited by the mobility of the ionic species and hence an increase in the oxidation rate can be related to faster ionic transport. Note that hole mobility for P3HT(C6OH)$_{50\%}$ was shown to be similar to that of P3HT (Figure 3.8).

All systems showed certain stability to multiple doping/dedoping, as seen by the equivalent trends of the response time t_{80} during the first (empty symbols) and tenth (solid symbol) bias runs (Figure 4.14). After ten runs, the oxidation process tends to slow down. However, PVA seems to render more stable systems and responses over time, reducing the differences in t_{80} between the first and tenth runs.

The differences observed in the shape of the profiles (Figure 4.13) prompted the study of the response time in further detail. The relative absorbance profile was normalised between 0 - 1 and its natural logarithmic was plotted as a function of time during V_{ON} (Figure 4.15; further details on the transformations can be found in Section 4.2.5).

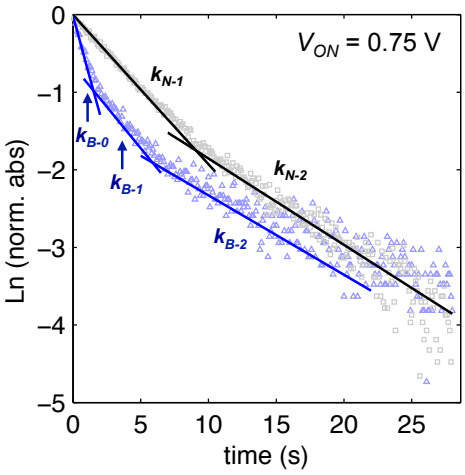


Figure 4.15: Semi-logarithmic relative absorbance spectra at 550 nm during applied bias of P3HT(C6OH)$_{50\%}$ (**black**) and P3HT(C6OH)$_{50\%}$:PVA (50:50 wt%) blend (**blue**). Multi-exponential decay characterises the redox process with rates k_N (neat P3HT(C6OH)$_{50\%}$) and k_B (P3HT(C6OH)$_{50\%}$:PVA blend). Each decay component seems to relate to various phase domains: range 0 (k_{B-0}) is specific to PVA-containing system; whereas ranges 1 - 2 (k_1 and k_2) have equivalent rates both in neat and blend systems.

Interestingly, after the variable transformation, it was observed that in both cases the decay was multi-exponential (Figure 4.15). Two of the exponential decays (labelled as k_1 and k_2) were found to be characteristic of both the neat semiconductor (k_{N-1} and k_{N-2}) and the blend (k_{B-1} and k_{B-2}), hence concluding that these are not dependent on the presence of PVA. Most intriguingly, a very distinctive fast regime K_{B-0} was observed in the blend within the first 1 - 2 s which did not appear in the neat P3HT(C6OH)$_{50\%}$. This suggests that this fast component is directly related to the presence of PVA, which potentially generates new pathways for ionic transport.

From AFM in fluid, it was observed that the addition of PVA aided swelling of blend systems (Figure 4.9). The water uptake clearly indicates the generation of new transport channels within the ion-conducting phase (PVA). Upon the swelling of the PVA phase by the electrolyte, readily available anions at the insulator/semiconductor interface would easily access a redox site, giving rise to the fast regime observed within the first seconds (corresponding rate k_{B-0}, Figure 4.15). The enhanced ionic transport observed in the P3HT(C6OH)$_{50\%}$:PVA system is in agreement with previous observations of improved ion mobility upon addition of hydrophilic gelatin to PEDOT, or the decrease in ion mobility in crosslinked (less swelled) PEDOT.[80,81]

4.3.4 A relation between aggregation and ionic transport

The existence of the two time components during the oxidation process (k_1 and k_2, Figure 4.15), which were independent of the presence of the insulator (PVA), was encouraging to further investigate which characteristics of the P3HT(C6OH)$_{50\%}$ determined them.

Similarly to the role of P3HT as model system in OPV,[63,105] the microstructure of the derivative semiconducting material (P3HT(C6OH)$_{50\%}$) was purposefully controlled in order to gain insight in the potential influence of order (at specific length-scales) on ionic transport. Since conducting polymers have complex microstructures where amorphous and ordered phases coexist, the volume fraction of each region can be controlled by means of processing methods.[37,101]

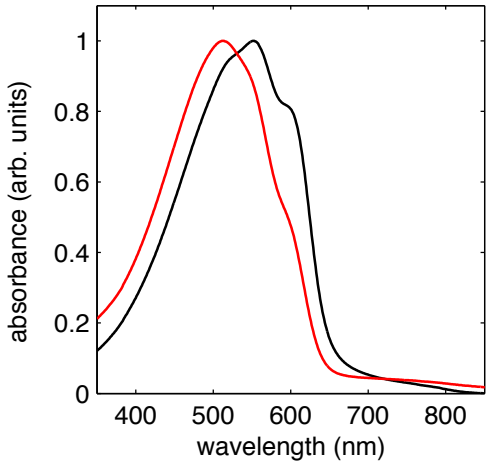


Figure 4.16: UV-Visible absorbance spectra of P3HT(C6OH)$_{50\%}$ thin films processed from a good solvent (THF, **red**) and compared to films processed from solvent mixture (THF:DMSO 2:1 v/v%, **black**). The addition of DMSO generates molecular aggregates, evidenced by the more pronounce 0 - 0 vibration transition at around 600 nm.

In order to combine the polar insulator into the blend during solution processing, a carefully selected mixture of THF:DMSO (2:1 v/v%) was needed (see Section 4.2.2). With the purpose of producing a range of microstructures, the neat P3HT(C6OH)$_{50\%}$ was also processed into films using THF, which can be considered as a better solvent compared to the previous solvent mixture and has a lower overall boiling point, highly affecting the solidification rate and subsequently the film's microstructure. In this respect, it was observed that solutions of equivalent

concentration remained fully dissolved at room temperature in THF, whereas they turned dark brown for THF:DMSO (Figure 4.3).

UV-Vis absorbance spectra of films cast from both solvents showed clear differences between the two (Figure 4.16). Films prepared from THF displayed weaker vibronic peaks (at approximately 520, 550 and 602 nm), which indicates a diminishing contribution of the aggregates fraction. The addition of DMSO seems to favour the formation of P3HT(C6OH)$_{50\%}$ molecular aggregates during film cast. This effect is in agreement to previous reports where a poor solvent, ethyl acetate, promoted the formation of highly aggregated P3HT in solution.[106]

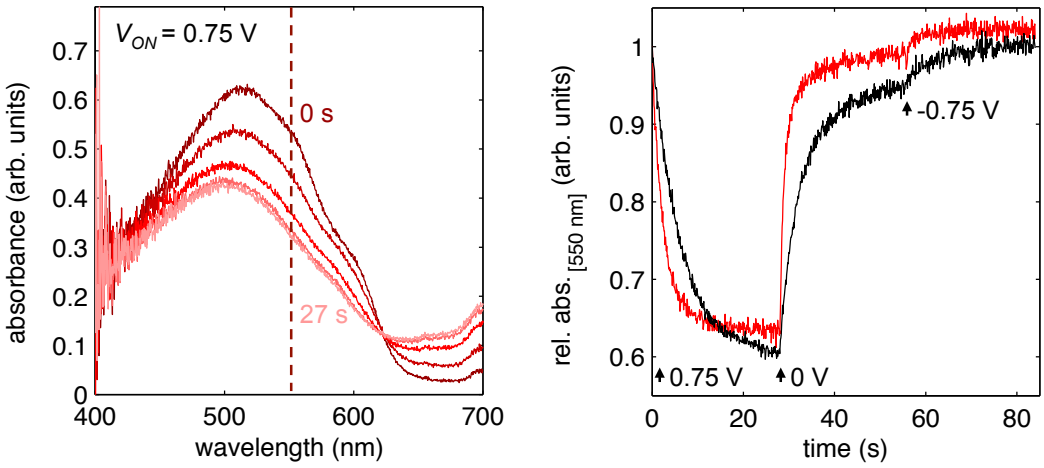


Figure 4.17: Comparison between P3HT(C6OH)$_{50\%}$ processed from THF and THF:DMSO 2:1 v/v%. **Left:** Real-time visible absorbance spectra when a bias V_{ON} = 0.75 V is applied to P3HT(C6OH)$_{50\%}$ processed from THF in the setup displayed in Fig. 3.2. Refer to Figure 4.12 (left) for the spectra of P3HT(C6OH)$_{50\%}$ processed from THF:DMSO 2:1 v/v%. **Right:** Relative absorbance spectra at 550 nm as a function of time during V_{ON} = 0.75 V (0 - 28 s), V_{OFF} = 0 V (28 - 56 s) and V_{REV} = -0.75 V (56 - 84 s) of P3HT(C6OH)$_{50\%}$ processed from THF (**red**) and THF:DMSO 2:1 v/v% (**black**). Electroactivity of the less aggregated material (cast from THF) shows to be faster during the full bias run.

Films were tested in the same electrochemical setup as for the blends, i.e. absorbance spectra were obtained as a function of time. The oxidation taking place during V_{ON} = 0.75 V is shown in Figure 4.17 (left). As can be observed from the absorbance decay of these films (Figure 4.17, right), the oxidation rate of P3HT(C6OH)$_{50\%}$ cast from THF was fast in comparison to the one cast from THF:DMSO. Similarly to the blend, the signal of the THF-cast films (**red**) rapidly

reached saturation during V_{ON} (0 - 28 s), as well as during V_{OFF} (28 - 56 s), meaning that the ions involved in the oxidation were more effectively released in the less aggregated system.

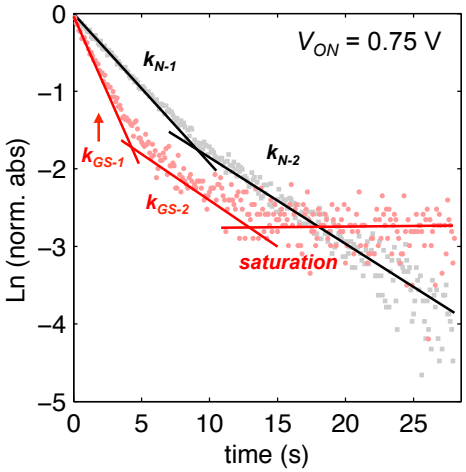


Figure 4.18: Semi-logarithmic relative absorbance spectra at 550 nm during applied bias of P3HT(C6OH)$_{50\%}$ processed from THF (**red**) and THF:DMSO (**black**). Both films were made of unmixed P3HT(C6OH)$_{50\%}$, however those cast from THF are referred to as "good solvent" (rates k_{GS}) and those from THF:DMSO as "neat" (rates k_N). Multi-exponential decay characterises the redox process. Rate k_1 was larger in the less aggregated system ($k_{GS-1} > k_{N-1}$), suggesting a link to the difference in aggregation found between systems; however, rate k_2 is equivalent in both unmixed as well as the blend systems ($k_{GS-2} \approx k_{N-2} \approx k_{B-2}$).

Notably, the semi-logarithmic data representation was fitted in both cases by two exponential decays before the signal saturated (Figure 4.18). While the first exponential rate constant k_1 was larger (faster) for the good solvent case (THF) than in the neat case (i.e. $k_{GS-1} > k_{N-1}$), the second rate constant k_2 was remarkably similar in all three cases (these two plus the blend).[(1)] A summary of the decay rate constants for the systems is presented in Table 4.1, along with their correspondent time constants ($\tau = 1/k$).

Based on the structural and transport data gathered in this work, a phenomenological explanation of the observations is proposed as follows. Both amorphous and ordered regions coexist in semicrystalline polymers, giving them a high level of complexity in the solid state. First, the fact that the addition of PVA did not influence k_1 or k_2 (Table 4.1, compare *Blend* and *Neat*)

[(1)] Although both films were cast of unmixed P3HT(C6OH)$_{50\%}$, those from THF are referred to as "good solvent" (rates k_{GS}) and those from THF:DMSO as "neat" (rates k_N).

Table 4.1: Summary of decay rates and corresponding time constants of P3HT(C6OH)$_{50\%}$, processed from THF (*GS*) and THF:DMSO (*Neat*), and P3HT(C6OH)$_{50\%}$:PVA blend (*Blend*). Data includes all decays 0 - 2, as seen in Figures 4.15 and 4.18. Errors shown for decay rates k are standard deviations calculated from multiple samples (n $\geq$ 3).

Material	k_0 (s^{-1})	k_1 (s^{-1})	k_2 (s^{-1})	τ_0(s)	τ_1 (s)	τ_2 (s)
Blend	0.64 ± 0.16	0.21 ± 0.03	0.10 ± 0.01	1.6 ± 0.4	4.7 ± 0.6	9.8 ± 1.4
Neat	-	0.19 ± 0.04	0.11 ± 0.01	-	5.2 ± 1.1	9.0 ± 0.9
GS	-	0.40 ± 0.10	0.12 ± 0.01	-	2.5 ± 0.6	8.4 ± 0.6

clearly points to hydration playing a separate role that manifests in a fast oxidation rate k_0. In addition, a decrease in the degree of crystallinity of P3HT(C6OH)$_{50\%}$ was noted as a result of the addition of PVA (Figures 4.5 and 4.6, as measured by DSC), hence suggesting that ionic transport may not be influenced by changes in the long-range order of the semiconductor ($k_{N-1} \approx k_{B-1}$ and $k_{N-2} \approx k_{B-2}$).

Secondly, when P3HT(C6OH)$_{50\%}$ was processed to exhibit decreased aggregation using a good solvent (THF), a faster first oxidation rate ($k_{GS-1} > k_{N-1}$) was observed, whereas the slower oxidation rate k_2 remained unvaried compared with both previous systems (*Blend* and *Neat*). This suggests that k_2 might be an intrinsic decay rate of the semiconducting polymer, while k_1 is linked to the degree of short-range order. The picture depicted by Noriega et al.[37] where hole transport takes place in the aggregate fraction of high molecular weight polymers but not within the amorphous regions contributes to our observations as well. It can be interpreted that the initial oxidation rate k_1 can be assigned to the oxidation in the short-range ordered regions of the polymer (aggregates), which largely represent the fraction of polymer responsible for hole transport. This link is not surprising considering that ionic transport in the observed redox process is directly related to hole transport, since the generation of a hole requires charge compensation by a Cl^- ion from the electrolyte due to charge neutrality within the bulk,.

Finally, in order to complete the picture, DSC of P3HT(C6OH)$_{50\%}$ processed from THF and THF:DMSO 2:1 v/v% were measured (Figure 4.19). Thermograms revealed similar crystallinity independently of solvent choice, with values of the enthalpy of fusion of 28.9 J/g and 25.5 J/g

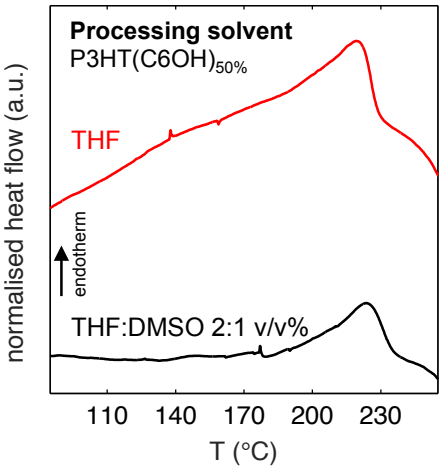


Figure 4.19: Differential scanning calorimetry (DSC) of P3HT(C6OH)$_{50\%}$ processed from THF and THF:DMSO 2:1 v/v%, from multi-layer thin films. Thermograms display similar crystallinity independently of solvent choice.

for THF and THF:DMSO, respectively. This is a further indication that long-range order does not influence ionic transport: from these results it is observed, if anything, a more crystalline material for THF system, even though it exhibited faster transport ($k_{GS-1} > k_{N-1}$).

In summary, k_1 seems to originate from the oxidation of the aggregated fraction of the polymer, since it was shown to be directly linked to the extent of this ordered phase created during processing ($k_{GS-1} > k_{N-1}$). The second oxidation rate k_2, which has a similar value for all the samples [*Blend* and both unmixed, *Neat* and *GS*], can be associated to the redox process taking place within the amorphous regions. Two observations support this interpretation: 1) the disordered amorphous phase is similar for all the samples (as there is no such thing as a degree of amorphism); and 2) this second oxidation rate is significantly slower than the first one ($\approx$ 2-fold), which is characteristic of amorphous phases.[37]

4.3.5 Influence of ion size on ionic transport

Ionic transport in the bulk of P3HT(C6OH)$_{50\%}$ was investigated through the material's electrochromic response, on the assumption that its oxidation (removal of an electron / injection of a hole) was compensated for by the injection of a Cl^- anion. Previous studies involving the oxidation of conjugated polyelectrolytes (in contact with a water electrolyte) have suggested the possibility of the native cation being involved in the process by being injected/ejected during redox; the only arguments ruling out such an effect were steric limitations.[61] However, since the only ionic species existing in the neat P3HT(C6OH)$_{50\%}$ and the PVA blend systems belong to the electrolyte, ionic transport was most certainly directly related to the transport of Cl^- anions during their injection into/ejection from the polymer bulk.



Figure 4.20: Chemical structures of salts used to prepare aqueous electrolytes of equivalent concentration (10 mM). **Left:** sodium chloride (NaCl). **Centre:** potassium chloride (KCl). **Right:** sodium p-toluenesulfonate (NaTOS).

Nonetheless, KCl was used as an alternative electrolyte salt to verify that Cl^- is directly involved with the redox (Figure 4.20, left and centre). Since only the cation K^+ is different (larger) than before (Na^+), no differences are expected in the dynamics of the redox process should it be linked only to the unvaried species (Cl^-).

Bias runs for neat P3HT(C6OH)$_{50\%}$ and PVA blends were performed using KCl under equivalent conditions as previously for NaCl (Figure 4.21). A comparison of results for the two electrolytes for both neat (left) and blend (right) systems interestingly revealed differences in the extent of oxidation, as a larger oxidation signal was observed when KCl was used compared to NaCl. Although the mechanism behind such behaviour is not clear, a relation to the solvation shell

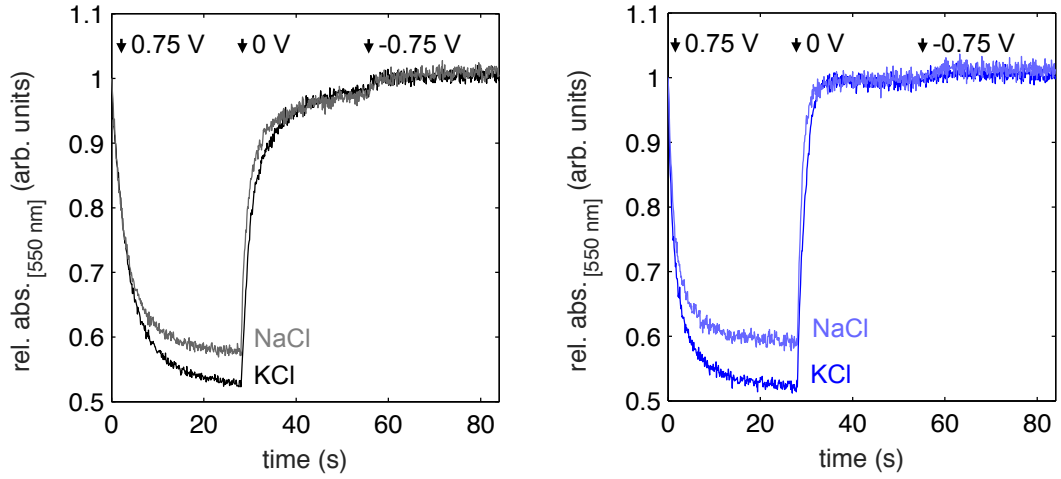


Figure 4.21: Relative absorbance spectra at 550 nm as a function of time during V_{ON} = 0.75 V (0 - 28 s), V_{OFF} = 0 V (28 - 56 s) and V_{REV} = -0.75 V (56 - 84 s) in 10 mM electrolytes of NaCl and KCl. **Left:** P3HT(C6OH)$_{50\%}$. **Right:** P3HT(C6OH)$_{50\%}$:PVA (50:50 wt%) blend. Stronger oxidation signal is observed for KCl in both systems, although time dependency remains unaffected.

size and capability to dehydrate of each cation (Na^+ and K^+) is proposed, as larger ions present lower charge density, leading to smaller and less stable solvation shells. Since K^+ is larger than Na^+, it is speculated that this difference could lead to K^+ being able to accumulate at a larger density at the Ag/AgCl electrode during oxidation, providing an overall larger signal.

Similarly to the time characterisation of the oxidation process performed when using NaCl, t_{80} was calculated for the range of P3HT(C6OH)$_{50\%}$:PVA when KCl was employed (Figure 4.22). Comparing the time response when using NaCl and KCl electrolytes (Figures 4.14 and 4.22), similar trends are observed with close values of t_{80} for equivalent blend ratios. The unvaried dynamics of the process indicates that Cl^- corresponds to the ion involved in the oxidation process. Compared to previous experiments, larger variability in t_{80} was observed in the 75:25 wt% blend system after 10 bias runs, as seen by the error bars. Its relation to either the electrolyte (KCl) or other factors could not be confirmed with the experiments performed within this thesis.

Since the active role of the anion (Cl^-) during oxidation was confirmed, it was interesting to learn about the influence anion size has on ionic transport in the polymer bulk. For this

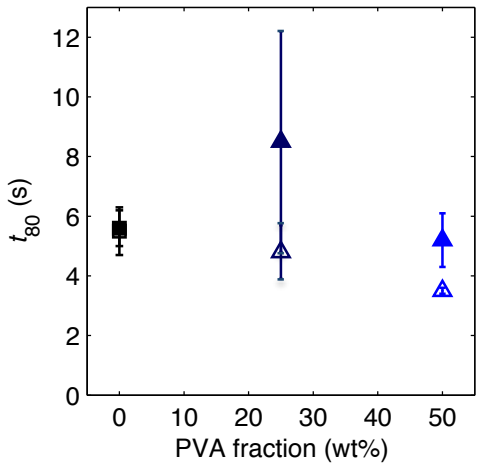


Figure 4.22: Oxidation time response, t_{80}, defined as the time to reach 80 % of maximum oxidation attained by each sample using a KCl electrolyte. Time t_{80} during V_{ON} is displayed for (**black**, square) the neat P3HT(C6OH)$_{50\%}$ and (**blue**, triangular) P3HT(C6OH)$_{50\%}$:PVA blends. *Empty symbols:* first bias run. *Solid symbols:* tenth bias run.

purpose, NaTOS (Figure 4.20, right) was used as an alternative salt, which provided the larger tosylate anion (TOS^-) for comparison.

Interestingly, equivalent characterisation of blend thin films revealed a reduction in ionic transport of TOS^- compared to Cl^- (Figure 4.23). The decrease in the speed is evidenced in each of the bias steps, although it becomes more apparent during $V_{OFF} = 0$ V when no electric field is applied and diffusion becomes the only driving force. In Figure 4.23 (left) a neat and a blend system are deliberately compared, since the addition of PVA also showed clear enhancement in ionic transport with the bulkier TOS^-. Not only the dedoping process (28 - 56 s) happens much faster, the extent of the dedoping almost reaches the neutral state within the first $\approx$ 10 s, which is a large difference in relation to the neat material.

Remarkably, during reverse voltage (56 - 84 s) the relative absorbance of the blend system went over its initial value (which is equal to 1, since relative absorbance is plotted). This behaviour reminds of the dedoping process previously observed for PEDOT:PSS (from 0 - 28 s in Figure 3.17) and suggests a similar operation. Although further investigation is required to understand the process, it could lead to interesting applications, for instance as an ambipolar system (due

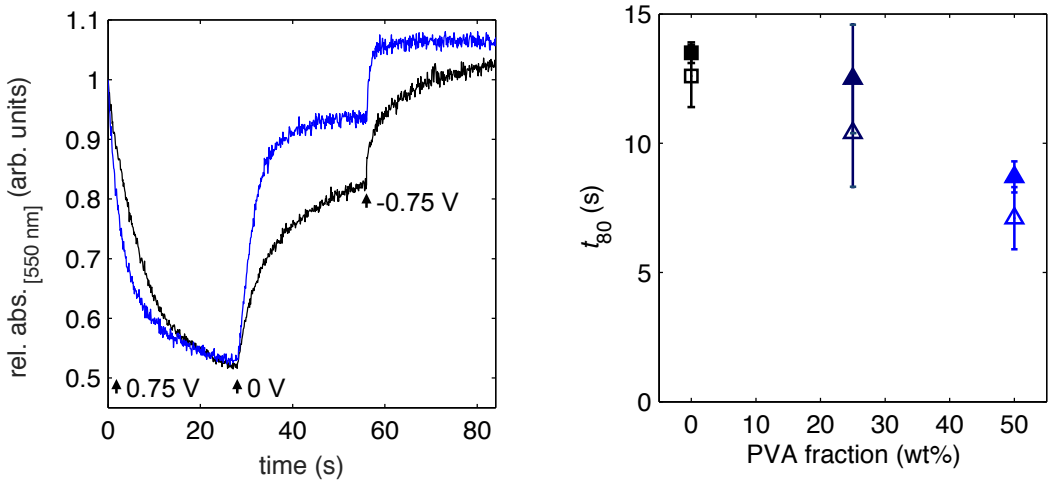


Figure 4.23: Response of (**black**) P3HT(C6OH)$_{50\%}$ and (**blue**) P3HT(C6OH)$_{50\%}$:PVA (50:50 wt%) blend using a 10 mM NaTOS electrolyte. **Left:** Relative absorbance spectra at 550 nm as a function of time during V_{ON} = 0.75 V (0 - 28 s), V_{OFF} = 0 V (28 - 56 s) and V_{REV} = -0.75 V (56 - 84 s). **Right:** Oxidation time response, t_{80}, during V_{ON}. *Empty symbols:* first bias run. *Solid symbols:* tenth bias run. Overall oxidation at 0.75 V and release of ions during 0 V is slower than the NaCl and KCl cases (Figure 4.21). As previously, faster response is observed for PVA-containing system (Figures 4.13 and 4.22 for NaCl and KCl, respectively).

to the material's response to both positive and negative bias) or a memory device (due to the dependence of the film's absorbance with its bias history, being more remarkable in the neat material, P3HT(C6OH)$_{50\%}$).

Finally, the characteristic time t_{80} shows again a decreasing trend of t_{80} upon PVA addition and relatively small hysteresis during 10 bias runs (Figure 4.23, right). It is interesting to note the differences in the characteristic time t_{80} between Cl^- and TOS^- for the neat system, as an increase factor of $\approx$ 2.3 is observed from the small to the larger anion. The faster ionic transport observed for Cl^- correlates with previously reported mobility of TOS^- in PEDOT(TOS):gelatin, which was 5 times lower than that of inorganic cations in PEDOT:PSS.[81]

4.3.6 Blends with other polar insulators

Encouraged by the general trend of improved ionic transport with the addition of polar PVA, studies with a different insulator were initiated. A PMMA derivative with a phosphonic acid moiety was used for this purpose (Figure 4.1, right). The phosphonic acid moiety is relevant because with a large enough functionalisation density it could render the derivative an effective macro-molecular dopant. However, for the purpose of this study, the derivative with low functionalisation level (10 mol%) was used. The typical selection criteria, similarly to that followed with PVA, was:

- to be bio-innert and/or bio-compatible
- to be polar or contain some polar units
- to be insoluble or partially insoluble in water

MMAcoMAPC1 was soluble in THF, hence blends were done using it as co-solvent.

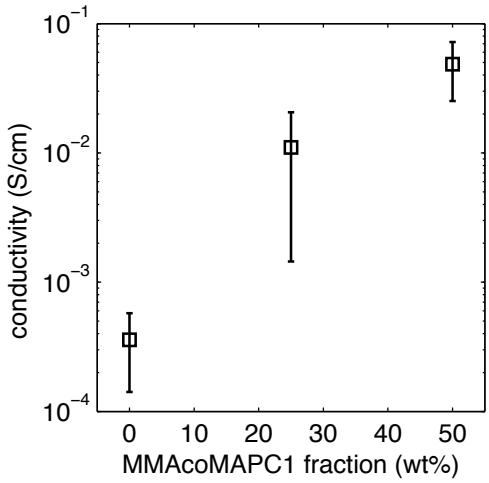


Figure 4.24: Conductivity of P3HT(C6OH)$_{50\%}$:MMAcoMAPC1 blends measured by 2-point setup. MMAcoMAPC1 dopes P3HT(C6OH)$_{50\%}$ increasing its conductivity by $\approx$ 2 orders of magnitude. Films were measured in ambient conditions.

The electrical conductivity revealed that even at low levels of functionalisation with the phosphonic acid, the insulator doped P3HT(C6OH)$_{50\%}$ increasing its conductivity by $\approx$ 2 orders

of magnitude (Figure 4.24). Compared to small acid dopants, which tend to easily leach out, using acid-functionalised polymers (such as MMAcoMAPC1) point out to a superior strategy in order to achieve non-toxic stable dopants.

The use of P3HT(C6OH)$_{50\%}$, containing a large density of polar -OH units also enhanced the mixing with MMAcoMAPC1. This effect became more apparent when comparing a 50:50 wt% blend of MMAcoMAPC1 with a derivative of lower -OH functionalisation; P3HT(C6OH)$_{10\%}$ blend clearly displayed larger phase separation domains (Figure 4.25).

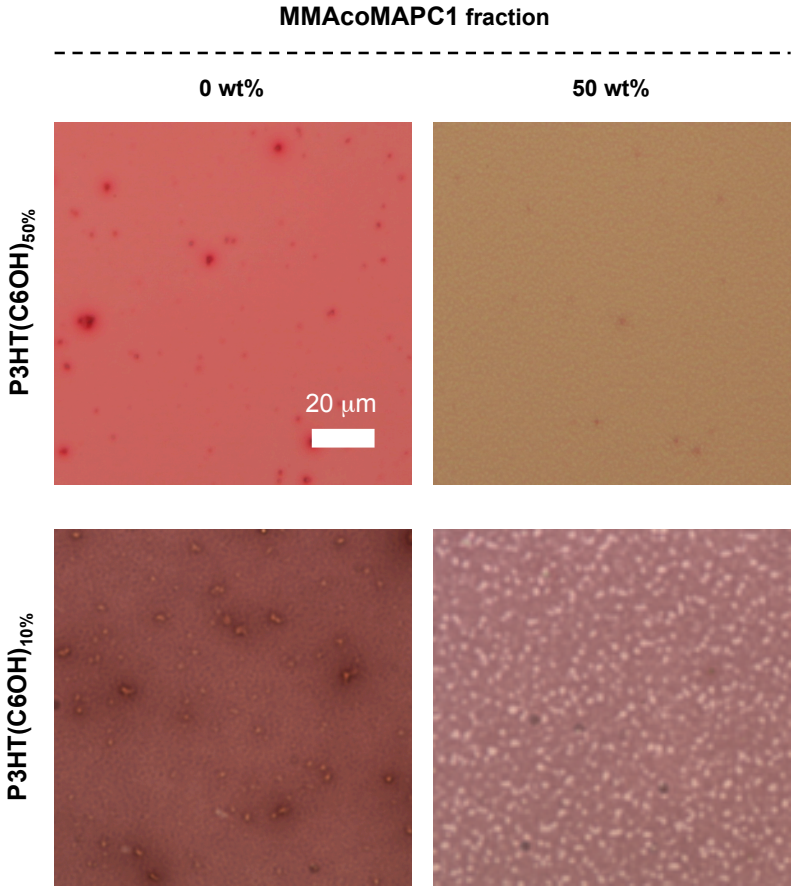


Figure 4.25: Optical micrographs of thin films of P3HT(C6OH)$_{10\%}$ and P3HT(C6OH)$_{50\%}$ and their corresponding 50 wt% blend with MMAcoMAPC1. The more polar nature of P3HT(C6OH)$_{50\%}$ contributes to improved mixing with MMAcoMAPC1; clear phase separated domains are observed in the P3HT(C6OH)$_{10\%}$:MMAcoMAPC1 blend.

The electroactivity of the new blends was also tested using a NaCl electrolyte (Figure 4.26). As previously seen when PVA was added, MMAcoMAPC1 also enhanced the ionic transport within the polymer bulk, despite it being to a lesser extent. A decreasing trend in t_{80} can be

clearly observed for the first bias run (Figure 4.26, right). However, upon multiple measurement runs 50:50 wt% blend samples showed a larger performance dispersion, which is reflected in the larger error associated to the corresponding t_{80}.

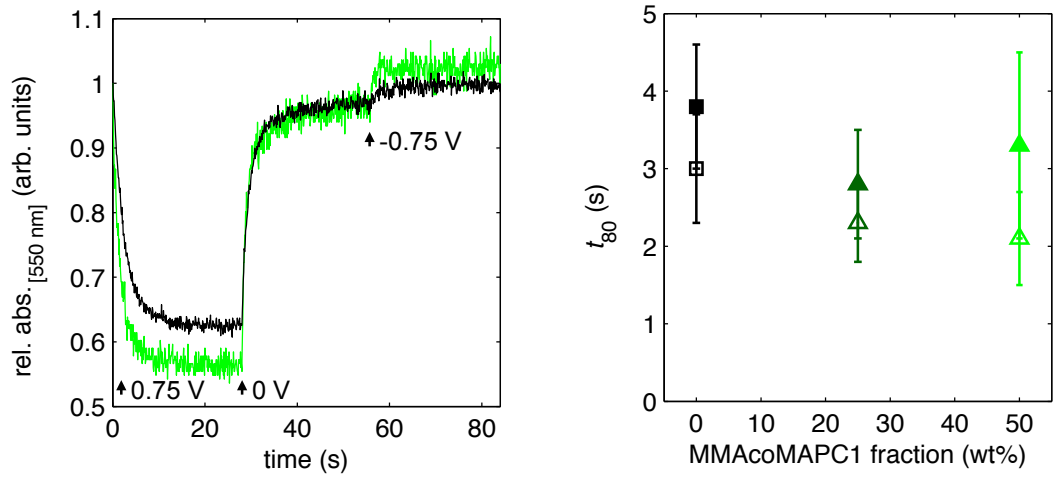


Figure 4.26: Response of neat P3HT(C6OH)$_{50\%}$ (**black**) and P3HT(C6OH)$_{50\%}$:MMAcoMAPC1 (50:50 wt%) blend (**green**). **Left:** Relative absorbance spectra at 550 nm as a function of time during V_{ON} = 0.75 V, V_{OFF} = 0 V and V_{REV} = -0.75 V. **Right:** Oxidation time response, t_{80}, during V_{ON}. *Empty symbols:* first bias run. *Solid symbols:* tenth bias run. Faster response is observed for MMA-containing systems.

Furthermore, it is interesting to note that MMAcoMAPC1-containing system also showed an increased absorbance signal during V_{REV} (56 - 84 s), as it was observed when NaTOS salt was employed (Figure 4.23). Previously, the possibility of TOS^- doping the semiconductor was speculated, and hence providing the chance of further dedoping it upon a reverse bias. However, in this case, based on conductivity data (Figure 4.24) it is clear that P3HT(C6OH)$_{50\%}$ is doped in the presence of MMAcoMAPC1, and hence the signal may corresponds to the further dedoping of the semiconductor until it reaches its original 'neutral' state (intrinsic).

4.4 Conclusions

There is a clear interest in the field of bioelectronics to create mixed ion/electron transport systems akin to PEDOT:PSS. After demonstrating the ability of P3HT(C6OH)$_{50\%}$ to act as an ion-to-electron transducing interface (Chapter 3), the more polar nature of this derivative was exploited to realise the first blend of this kind of material with PVA by carefully selecting a solvent that ensured appropriate transport properties. Accordingly to the interest of this new system as a mixed conductor within water environments, the ionic transport properties were measured in contact with an aqueous electrolyte. The addition of PVA has a direct effect on enhancing the ionic transport in the bulk, which seems to be related to enhanced inter-diffusion of the electrolyte through the material upon swelling. This simple blending approach to enhance ionic transport could become a powerful tool that may be extended to other functional semiconductors and insulators, allowing improved versatility on ionic transport in akin systems. Indeed, the use of an alternative insulator was demonstrated, a PMMA derivative, which showed the potential of general use of blending with polar polymers.

Most importantly, this is the first report to the best of our knowledge of a phenomenological description of ionic transport taking place in different regions of semicrystalline polymers, with distinctive associated decay rates. This new insight on the effect of short-range molecular order on ionic transport could give rise to improved rational design of materials with controlled mixed transport for bioelectronics.

I foresee further relevant roles of the insulating phase, for example to enhance cell attachment due to favourable moiety exposure or to target it as attachment point for specific biofunctionalisation.[60] Further opportunities could also arise from the interesting ambipolarity observed in certain systems as well as new directions in the design of more stable, multi-function dopants.

Chapter 5

Charge transport properties of polymer thin films under controlled hydration

5.1 Introduction

It is usually found that the operation of devices based on semiconducting polymers, or more generally, π-conjugated materials, are heavily affected by ambient conditions.[107] Generally, devices are tested in an inert atmosphere (N_2) and the research community has dedicated much effort to find solutions to the longer-term stability of such devices, for example by encapsulating them.[108] There is also an interest in understanding which parameters influence the 'state' of conducting polymers in ambient conditions and multiple studies have shown that molecular oxygen (O_2) affects the devices operation by *p*-doping the conjugated backbones.[109,110,111,112]

Few reports exist that have presented a comprehensive study of the influence of water moisture, decoupled from other species, on the charge transport of conducting polymers.[112,113,114] Even fewer have been dedicated to elucidating transport in hybrid conducting materials as a function of hydration.[115] Distinguishing between ionic and electronic charge entities has proven troublesome, since the transport of both species is dominated by hopping.[116]

The work presented in this Chapter is a collaboration with Prof. Paul Meredith (University of Queensland) and aims to further the understanding of mixed transport in material interfaces suspected to sustain both ionic and electronic transport. The body of work on charge transport in polythiophene derivatives presented in this thesis is complemented in this Chapter with the fabrication and testing of devices with structures suitable for hydration studies. The experimental setup is of interest, since the modulation of humidity using a vacuum line system avoids contamination with any salt species and allows good control over the vapour pressure of water. Additionally, hybrid devices that include the proton conductor Nafion® were fabricated as multi-component bilayers and studied under hydrated conditions, shedding light on the interaction between dissimilar charged species (ions and electrons/holes) at the semiconductor/Nafion® interface.

This Chapter starts with the assessment of the influence of moisture on the charge transport of polythiophene derivatives, which is highly relevant for the application of such systems in bioelectronics. The metals used as electrodes also showed some interactions with the semicon-

ductors, influenced by the hydrophilic nature of the polymers themselves, as well as the humid atmosphere. Finally, the study of multi-layered structures involving Nafion® showed interesting memristic behaviour that could be switched by varying humidity levels. The transport processes in hybrid conducting materials is complex and the results here presented could serve as an inspiration to further explaining and optimising device performance.

The experiments presented in this Chapter were performed with the assistance of Dr Bernard Mostert (University of Queensland) who helped in preparing the setup, measuring and data interpretations; and the assistance of Dr Ester Buchaca-Domingo (Imperial College London) who helped in measuring and in the design and preparation of Nafion®/P3HT bilayers.

5.2 Materials and methods

Chemical structures of the materials used are shown in Figure 5.1. Poly(3-hexylthiophene) (**1:** P3HT) was purchased from Merck (mass-average molecular weight $M_w = 54200$ g/mol, dispersity Đ = 2.29, regioregularity RR = 94.2 %; stock SAP No EE99202) and used as received. Polythiophene derivatives poly(3-hexylthiophene)-co-(3-(6-hydroxyhexyl)thiophene) of varying molar ratios **2:** P3HT(C6OH)$_{10\%}$ ($M_w = 60000$ g/mol, dispersity Đ = 1.45), **3:** P3HT(C6OH)$_{20\%}$ ($M_w = 37000$ g/mol, Đ = 1.30) and **4:** P3HT(C6OH)$_{50\%}$ ($M_w = 63000$ g/mol, Đ = 1.82) were synthesised and provided by Dr Olivier Dautel (AM2N Laboratory, Charles Gerhardt Institute, France). Nafion® was purchased from Sigma-Aldrich (117 solution, ≈ 5 % in a mixture of lower aliphatic alcohols and water) and used as received.

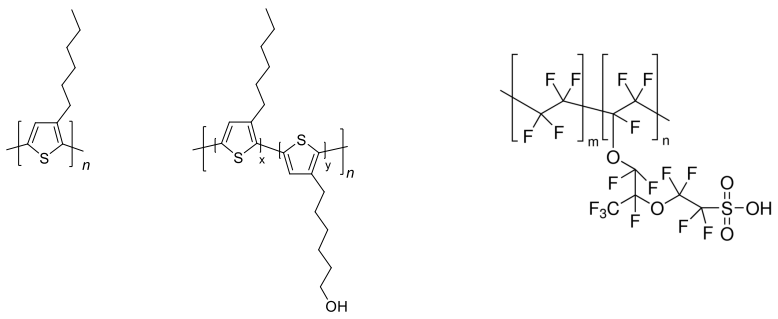


Figure 5.1: Chemical structures of polymers. **Left:** poly(3-hexylthiophene) (**1:** P3HT). **Centre:** OH-containing poly(3-hexylthiophene)-co-(3-(6-hydroxyhexyl)thiophene) of varying ratios: $x = 0.9$, $y = 0.1$ (**2:** P3HT(C6OH)$_{10\%}$); $x = 0.8$, $y = 0.2$ (**3:** P3HT(C6OH)$_{20\%}$); $x = 0.5$, $y = 0.5$ (**4:** P3HT(C6OH)$_{50\%}$). **Right:** Nafion®.

All polymer solutions (materials **1** - **4**) were prepared at a concentration of 8 mg/ml and heated while stirring at 58 °C on a hotplate for a minimum of 2 h until fully dissolved. The vials were fitted in a metal chuck in order to ensure homogeneous heating and avoid partial solidification of material close to the solution/air interface. All solutions were freshly prepared and used within a window of 3 h after dissolution.

Thin films of materials **1** - **4** and Nafion® were prepared on glass substrates following the protocols described in Section 2.1. The bilayer structure was similarly prepared by wire-bar coating in a layer-by-layer deposition fashion. Layers were left to fully dry before the deposition

of the subsequent polymer layer. No additional treatment was done to the bottom film before deposition of the top one.

5.2.1 Van der Pauw configuration: sample preparation

Current-voltage (I-V) measurements were performed on a four-electrode geometry according to the configuration described by van der Pauw.[117] This device structure allowed us to calculate the conductivity of a wide range of systems at varying levels of humidity inside a controlled vacuum system. The open channel configuration ensured the equilibrium of the sample with the humid atmosphere during the measurement, as opposed to a sandwich structure which would only expose the lateral area of the film.

Thin film samples were contacted by thermally evaporating the metal electrodes (either *Au* or *Al*, ≈ 80 - 100 nm thickness) through an in-house made shadow mask (Figure 5.2, left), which was placed onto the thin films. The geometry of the electrodes once evaporated onto the thin film can be seen in the top view sketch on Figure 5.2 (right) - note that electrodes are not to scale.

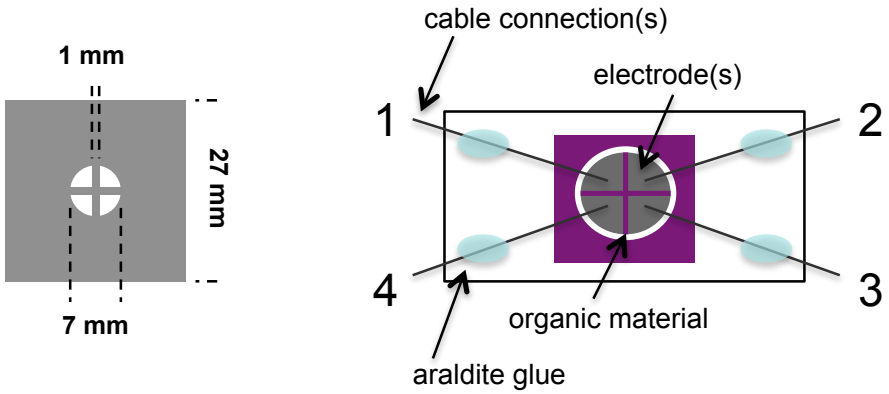


Figure 5.2: Sample preparation for van der Pauw tests. **Left:** Shadow mask used to evaporate the metal electrodes. **Right:** Sketch depicting all components of a prepared sample. *Electrodes are larger than scale to ease their view.*

Once the sample electrodes were evaporated, the samples were glued onto a glass slide using araldite epoxy. Cables were similarly secured with the epoxy in order to ensure that the connection did not come loose during the experiment. Subsequently, careful removal of the

thin film surrounding the electrodes was done by scratching with a fine scalpel; this is observed in Figure 5.2 (right) as a white circular rim.

Four copper cables were attached to the surfaces of the metal electrodes with silver epoxy conductive adhesive (RS Components Ltd.), which was carefully spread out to cover most of the electrode area. Figure 5.3 shows a sample ready to be placed in vacuum and tested.

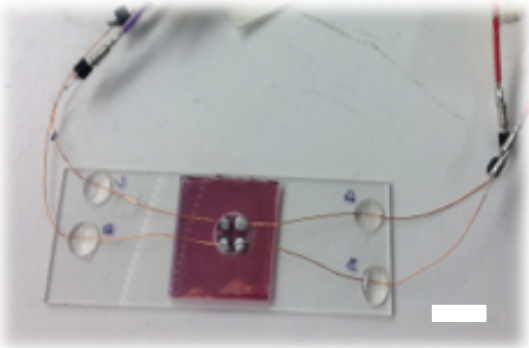


Figure 5.3: Example of a sample prepared for van der Pauw tests. *Scale-bar: 1 cm.*

After the sample was connected with the cables, it was placed onto the sample holder and wired in a 4-cable configuration to the Source-Measure Unit (SMU). The four cables were connected to a vacuum-sealed connection line on the inside of the chamber that had a female Fisher 9-pin plug on the outside. A male Fisher 9-pin plug wired to a shielded cable was attached to an aluminium electrical box which had four terminals, which closed the circuit by connecting to the SMU using coaxial cables. The aluminium chamber where the sample was placed was connected to the vacuum line, to which a degassed water flask and a pressure gauge were also connected and subsequently used to control the vapour pressure of water in the chamber. The full setup with a close up of the pressure pump, water flask and vacuum chamber, is shown in Figure 5.4.

Once the sample was located in the chamber and all the connections were tested to ensure they were correctly connected and had not shorted, the vacuum line was evacuated using a rotary pump for ≈ 30 min. The chamber was then isolated from the pump and remained under vacuum for 30 - 40 min before any I-V measurements were taken, unless otherwise stated. Samples were allowed to stabilise for 40 min between hydration levels, before measurements were resumed.

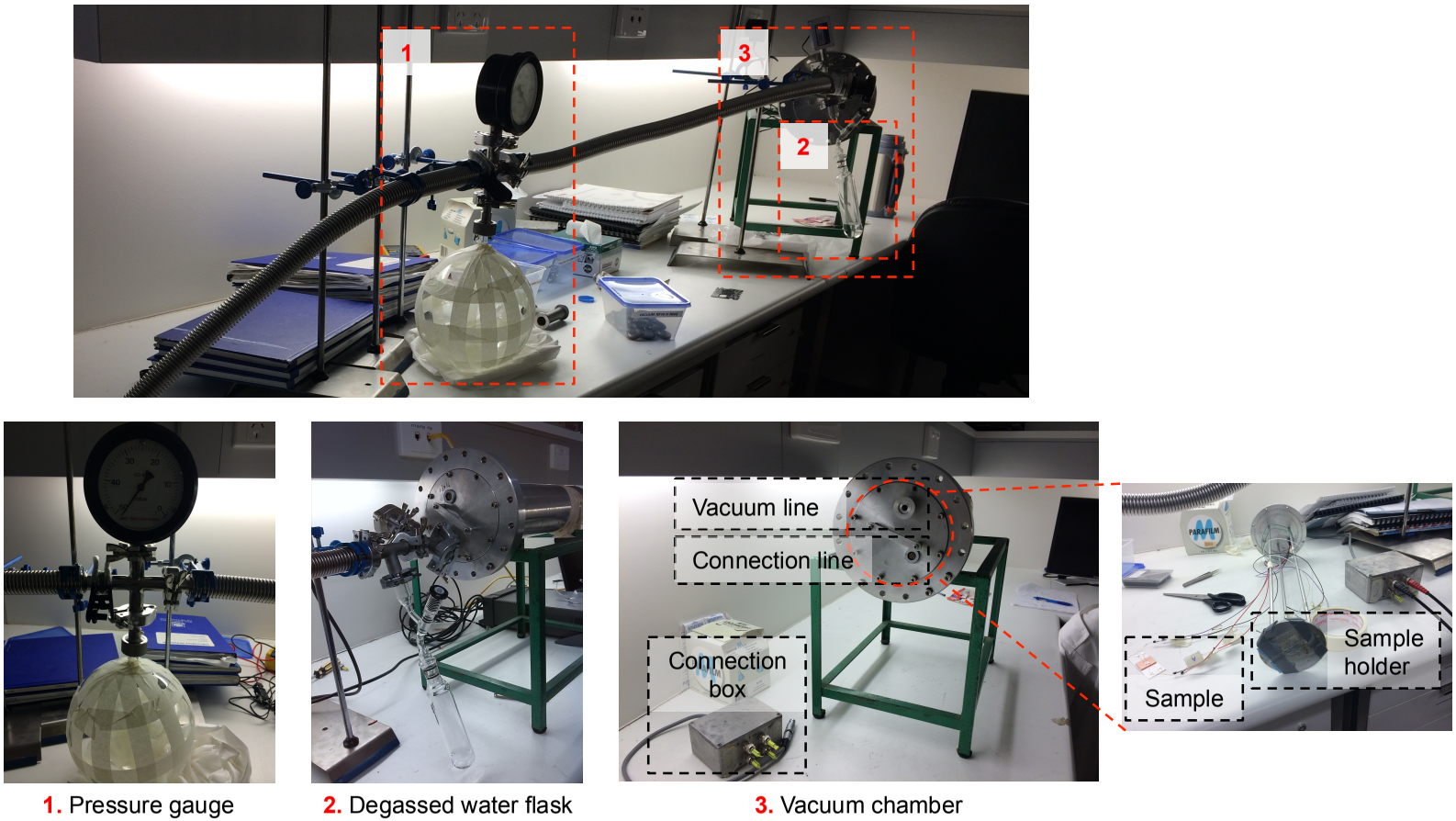


Figure 5.4: Experimental setup displaying the vacuum line, chamber and other components used to perform hydration-controlled van der Pauw tests. *Images taken by Dr Ester Buchaca-Domingo (Imperial College London) at the laboratories of the University of Queensland.*

5.2.2 Van der Pauw configuration: tests and data handling

The use of van der Pauw configuration eliminates the interference of contact resistance with the measured data, since it is a 4-terminal probe setup. As previously mentioned, the open channel also maximises the exposure of the semiconductor to the chamber atmosphere, ensuring the equilibrium of the material with the humidity level. The permanent connection of the cables to the four electrodes in van der Pauw configuration is also desirable for the experiment, providing stable contacts as opposed to typical 4-point probe, where the contact between the electrodes and the film relies on the pressure exerted on the probes against the film.

Current-voltage (I-V) measurements were taken at varying hydration levels. The humidity inside the aluminium chamber was controlled by bleeding water vapour from the flask containing Milli-Q water (freeze-pump-thawed three times), which was visualised at the pressure gauge (BOC-Edwards Pressure Gauge GK series, 0 - 50 mbar). The precision of the analog pressure gauge was 0.5 mbar and a nominal value of 0 mbar is given when the chamber was under vacuum. In all graphs presented in Chapter 5, a value of 0 mbar corresponds to the gauge reading and hence a vacuum under 0.25 mbar, and effectively no humidity. During the bleeding of water vapour, some condensation of water took place on the surfaces of the chamber within the first 5 - 10 min, decreasing the effective vapour pressure. This was corrected with further bleeding of water vapour after $\approx$ 10 min of stabilisation. The condensation process affected the chamber pressure more when the humidity level got closer to the saturating vapour pressure of water, which was experimentally found to be between 24 - 25 mbar.

I-V data was obtained using a Keithley 2400 SMU (internal impedance 1 GΩ), set to 4-wire measurement configuration. Voltage was ramped from -5 V to 5 V in a single linear sweep, taking 51 points/scan with a delay of 0.1 s/point. For each of the eight van der Pauw configurations (Figure 5.5), three sweeps were made and averaged to one for fitting the data.

The average resistances across the horizontal and vertical configurations (Figure 5.5, top and bottom, respectively), R_H and R_V, were used to calculate the conductivity of the thin films. These were calculated by fitting the linear (ohmic) regime of the I-V curves to a straight line,

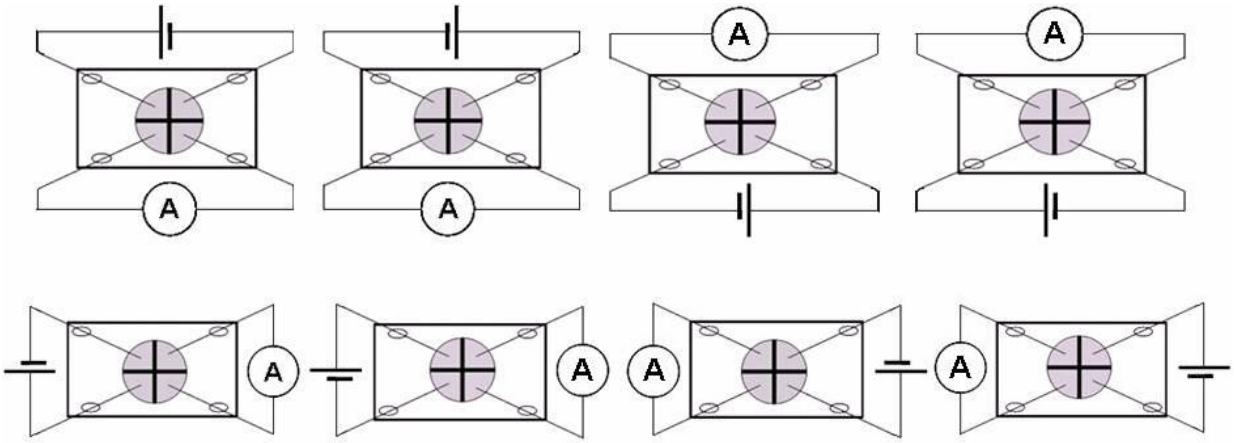


Figure 5.5: Sketch of the eight van der Pauw configurations to perform I-V measurements. **Top:** Horizontal series. **Bottom:** Vertical series. *Figure taken from Mostert.*[118]

following Ohm's law ($V = IR$).

For circular sample/electrode geometry, the van der Pauw technique relates the measured resistances to the conductivity as:

$$1 = e^{-\pi R_H d\sigma} + e^{-\pi R_V d\sigma} \tag{5.1}$$

where R_H is the average resistance for the four horizontal configurations, R_V is the average resistance for the four vertical configurations, d is the sample thickness and σ is the material's conductivity.

Equation 5.1 cannot be solved analytically when $R_H \neq R_V$. However, initial testing showed that the polymer samples were homogeneous in both directions with good reproducibility. Hence, for samples that have symmetry it can be assumed that $R_H = R_V$ and the conductivity can be calculated as:

$$\sigma = \frac{ln2}{\pi R d} \tag{5.2}$$

where R is the average resistance for all eight configurations, or equivalently $\langle R \rangle = \frac{\langle R_H \rangle + \langle R_V \rangle}{2}$.

The random error associated to the conductivity for the van der Pauw configuration is:

$$\Delta\sigma^2 = \left(\frac{ln2}{\pi R^2 d}\right)^2 \Delta R^2 + \left(\frac{ln2}{\pi R d^2}\right)^2 \Delta d^2 \tag{5.3}$$

where ΔR is the uncertainty due to inhomogeneity in the sample and the noise in the measurements and Δd is the error associated with the sample thickness.

The uncertainty ΔR was considered as the maximum of the noise in the data, ΔR_{noise}, and the standard deviation of R, SD_R. Considering the SD_R ensures any inhomogeneities across the eight configurations are taken into account as a random error.

Since the purpose of this experiment is capturing the qualitative behaviour of the polymer in the presence of humidity, the use of random errors as described above was relevant because systematic errors do not affect the trends. Hence no further calculations of the systematic error due to the van der Pauw electrode configuration/size were performed in this thesis.

5.3 Results and discussion

5.3.1 Thiophene derivatives with -OH moieties: transport vs. hydration

The implementation of organic semiconductors in bioelectronics generally involves the direct contact of the material with water or, alternatively, functioning at high levels of humidity.[56] Hence, it is important to understand the influence of such chemical environments to the charge transport characteristics on the materials of interest.

P3HT and its co-polymer derivatives functionalised with -OH moieties were tested in vacuum and increasing humidity conditions, while other oxidising species such as O_2 were excluded from the chamber where measurements were performed.

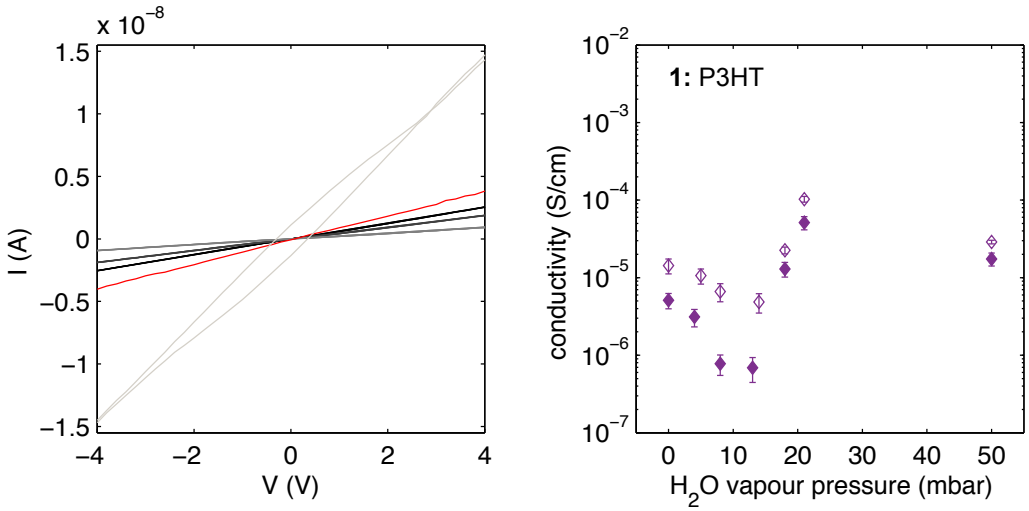


Figure 5.6: **Left:** Representative I-V curves of **1:** P3HT thin films measured by 4-point van der Pauw setup as a function of hydration (controlled by the H_2O vapour pressure). *Red*: ambient. From *black*-to-*lighter grey*: subsequently 0, 5, 14 and 21 mbar. **Right:** Conductivity of two P3HT samples calculated from van der Pauw measurements. Ambient conditions are represented in the graph as H_2O vapour pressure of 50 mbar. Chamber was pumped for ≈ 30 min for both samples. Error bars calculated using Equation 5.3 (see Section 5.2.2).

P3HT samples were placed in the chamber and the vacuum pump operated for the same evacuation time (≈ 30 min, until the gauge went to 0 mbar) before current-voltage (I-V) curves

were measured in the van der Pauw configuration at varying hydration levels. A representative set of curves is shown in Figure 5.6 (left) in ambient and H_2O vapour pressures of 0, 5, 14 and 21 mbar. The conductivity of two samples, calculated for these conditions, is shown in Figure 5.6 (right). Upon placing the samples in vacuum, dedoping takes place as observed by the decrease in the conductivity from ambient (50 mbar in graph) to 0 mbar. Conductivity decreases further, by up to an order of magnitude, as the pressure rises from 0 - 14 mbar, only showing signs of doping at pressures $>$ 14 mbar. In addition, the increase in conductivity to a value larger than at ambient, which is only observed at a pressure of 22 mbar, is accompanied by a change in the shape of I-V curve which presents signs of hysteresis. This may be a sign of ionic transport contributing to the overall current; similar behaviour in perovskite-based solar cells has previously been speculated as migration/transport of ionic species.[119] The measurements were reproducible, although variations are observed between the two tested samples of each material, the trends observed with increasing humidity are equivalent.

The -OH moieties in the P3HT derivatives **2** - **4** may enhance the adsorption of water and O_2 molecules during their time exposed to ambient conditions and, as a consequence, slow down the removal of such dopant species during the chamber evacuation. Hence, OH-containing polymers were kept for longer times in vacuum before any measurements were taken. Conductivity vs. hydration curves of the derivative polymer samples, placed in vacuum for longer and shorter periods of time, are compared in the following figures.

P3HT(C6OH)$_{10\%}$ (Figure 5.7, right) showed a conductivity profile upon hydration different to that of P3HT (Figure 5.6, right). Despite presenting a similar decreasing trend up to 13 - 14 mbar, the doping observed at high hydration in P3HT seemed to be more notably reduced by the presence of -OH groups. It is unclear what is the mechanism behind this trend; a hypothesis is that -OH sites act as traps for water molecules, hence decreasing their interaction with the polymer backbone. Changing evacuation times from 30 min to 2.5 h seemed to make no difference to the dedoping of the material in vacuum and the overall conductivity profile upon hydration, indicating that vacuum times around 30 min are suitable for stable bulk dedoping and charge transport measurements of thin films of **2**, at least for the conditions and device structure tested here.

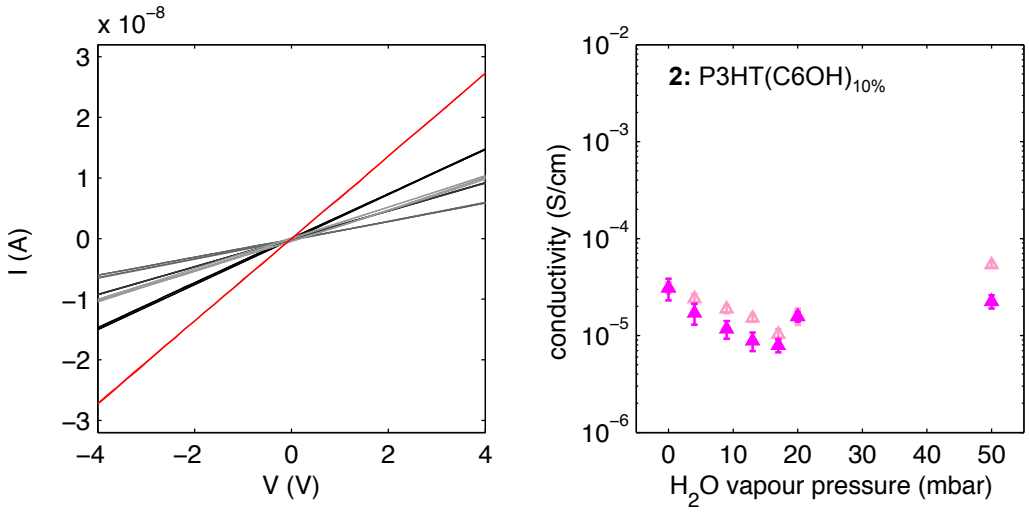


Figure 5.7: **Left:** Representative I-V curves of **2:** P3HT(C6OH)$_{10\%}$ thin films measured by 4-point van der Pauw setup as a function of hydration (controlled by the H_2O vapour pressure). *Red*: ambient. From *black*-to-*lighter grey*: subsequently 0, 5, 13 and 22 mbar. **Right:** Conductivity of two P3HT(C6OH)$_{10\%}$ samples calculated from van der Pauw measurements. Ambient conditions are represented in the graph as H_2O vapour pressure of 50 mbar. Chamber was pumped for *empty symbols:* $\approx$ 30 min and *solid symbols:* $\approx$ 2.5 h. Error bars calculated using Equation 5.3 (see Section 5.2.2).

I-V curves in Figure 5.7 (left) showed ohmic behaviour for the full vapour pressure range, showing no signs of hysteresis, and also all current values were below that at ambient. This seems to indicate that no ionic transport contribution is measured, in contrast to the observations of P3HT.

Material **3**, which contains 20 % OH-functionalised monomers, was tested after applying vacuum for 1.5 h and 2.5 h, i.e. longer than for **2**. Similarly to P3HT, material **3:** P3HT(C6OH)$_{20\%}$ dedoped from 0 - 14 mbar, showing signs of doping at pressures $>$ 14 mbar (Figure 5.8, right). An equivalent trend is observed for the two samples of **3** kept under vacuum for 1.5 h and 2.5 h. As in the case of P3HT (Figure 5.6, left), the I-V curve at 22 mbar shows signs of ionic transport adding up to the overall current, as inferred by the hysteresis observed (Figure 5.8, left; light-grey curve). Furthermore, conductivity at 22 mbar also surpassed that at ambient, which suggests that an extra contribution to charge transport exists other than the free charge carriers resulting from the expected *p*-doping due to water molecules, which are also present in ambient conditions.

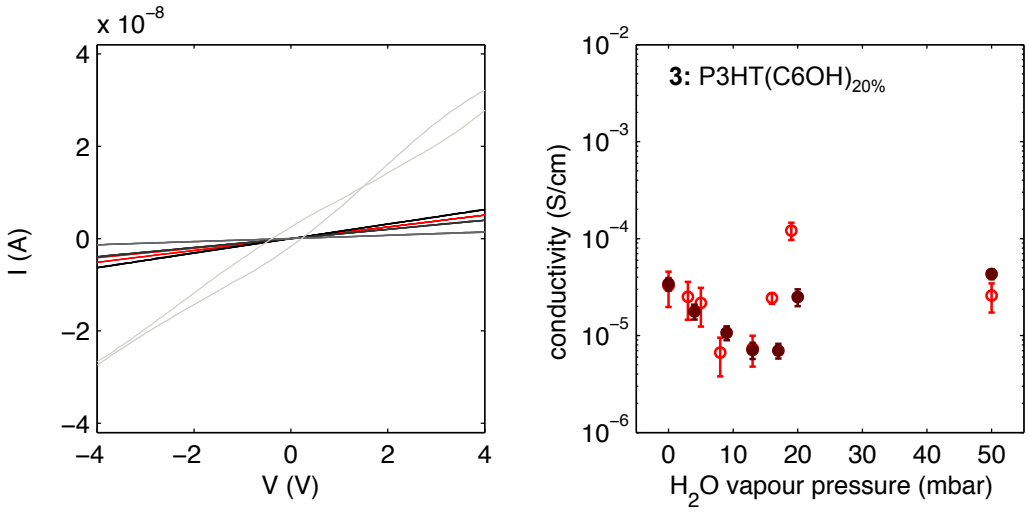


Figure 5.8: **Left:** Representative I-V curves of **3:** P3HT(C6OH)$_{20\%}$ thin films measured by 4-point van der Pauw setup as a function of hydration (controlled by the H_2O vapour pressure). *Red*: ambient. From *black*-to-*lighter grey*: subsequently 0, 5, 13 and 22 mbar. **Right:** Conductivity of two P3HT(C6OH)$_{20\%}$ samples calculated from van der Pauw measurements. Ambient conditions are represented in the graph as H_2O vapour pressure of 50 mbar. Chamber was pumped for *empty symbols:* $\approx$ 1.5 h and *solid symbols:* $\approx$ 2.5 h. Error bars calculated using Equation 5.3 (see Section 5.2.2).

The unexpected behaviour of **3**, with a trend differing from that of **2**, indicates increasing -OH may have a different effect to the material's hydration profile as a function of H_2O pressure, and hence displaying different current-voltage profiles at the same water vapour pressures.

A very different scenario is observed for material **4:** P3HT(C6OH)$_{50\%}$ in Figure 5.9. Since the -OH loading is greater than in previous derivatives, this material was evacuated for even longer times (up to 14 h) to ensure dedoping was fully achieved for all systems, as well as to learn if dedoping time-scales differed depending on -OH loading.

First, the conductivity of **4** was over one order of magnitude larger than that of materials **1** - **3** in ambient conditions (Figure 5.9, right). This suggests that the high load of -OH turned **4** into a self-doped polymer. The conductivity of samples in vacuum did not decrease with respect to that in ambient, indicating that dedoping of **4** was not possible even after vacuum times as long as 14 h. An equivalent trend is observed for samples kept in vacuum for 1.5 h and 14 h.

In addition, the conductivity decreased with increasing H_2O vapour pressure in the full range

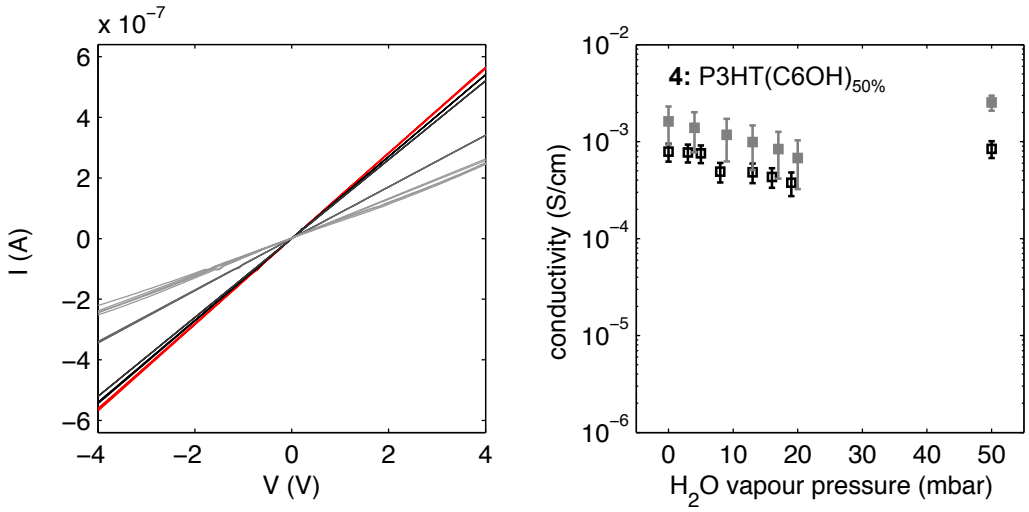


Figure 5.9: **Left:** Representative I-V curves of **4:** P3HT(C6OH)$_{50\%}$ thin films measured by 4-point van der Pauw setup as a function of hydration (controlled by the H_2O vapour pressure). *Red*: ambient. From *black*-to-*lighter grey*: subsequently 0, 5, 13 and 22 mbar. **Right:** Conductivity of two P3HT(C6OH)$_{50\%}$ samples calculated from van der Pauw measurements. Ambient conditions are represented in the graph as H_2O vapour pressure of 50 mbar. Chamber was pumped for *empty symbols:* $\approx$ 1.5 h and *solid symbols:* $\approx$ 14 h. Error bars calculated using Equation 5.3 (see Section 5.2.2).

of 0 - 22 mbar. This trend is opposite to the doping observed, at varying degrees, for materials **1** - **3** at 22 mbar. I-V curves (Figure 5.9, left) showed no signs of ionic conductivity, as seen from the highly linear behaviour at all H_2O vapour pressures.

A comparison of the full range of samples tested **1** - **4** is shown in Figure 5.10. In this plot it is clear that the conductivity of **4** is over an order of magnitude larger than the rest of the systems, which is attributed to the presence of -OH moieties acting as (self-)dopants. The addition of -OH functionalised monomers seemed to have a varying effect on charge transport with increasing moiety density. No functionalisation (**1**) or mild levels of it (**3**) proved to support ionic transport in the thin films, as observed by the corresponding hysteresis of their I-V curves at high hydration levels and the larger current levels compared to those at ambient conditions, which are an indication of the ionic current contribution. It is unclear why **2** or **4** did not show signs of ionic transport, nor their conductivity increase at high humidity levels. Further experiments are required to achieve a better understanding of such behaviour.

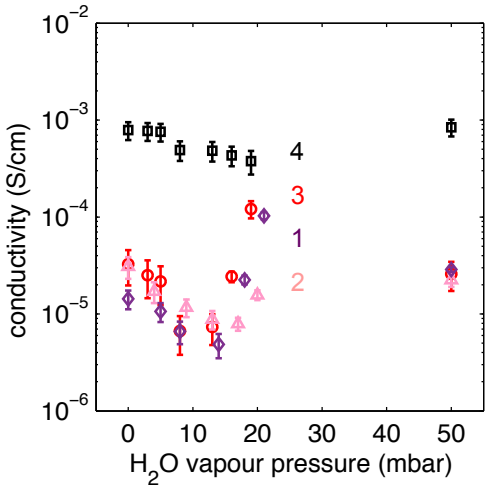


Figure 5.10: Comparison of conductivity of **1:** P3HT (purple *diamonds*) and derivatives **2:** P3HT(C6OH)$_{10\%}$ (pink *triangles*), **3:** P3HT(C6OH)$_{20\%}$ (red *circles*) and **4:** P3HT(C6OH)$_{50\%}$ (black *squares*), calculated from van der Pauw measurements. Ambient conditions are represented in the graph as H_2O vapour pressure of 50 mbar. Chamber was pumped for an approximate time of 1.5 h $<$ t $<$ 2.5 h for all samples.

Overall, it was observed that longer evacuation times did not further dedope any of the P3HT derivatives, even when the system (**4**) was in vacuum for up to 14 h. Samples made of the same materials followed the same trends upon increasing hydration, which is a good indication of reproducibility within the experimental conditions tested. I-V curves showed highly ohmic behaviour, with the only deviations taking place at high hydrations levels (20 - 22 mbar) for the systems that showed hysteresis (**1** and **3**).

Many questions regarding the hydration process still remain unanswered. Does water adsorb within the volume or predominantly on the surface? Does this depend on the functionalisation level? The packing of the semiconductors was shown to be similar for **1** - **4**, as seen by their short-range foot-print provided by their UV-Vis spectra (Figure 3.6). Hence, density packing differences between the materials is expected to have no or little effect on the hydration.

Normalising the vapour pressures to the sample hydration (as measured by gained weight) would also be of interest in future experiments and may help understanding some of the unexpected differences betweens derivatives **2** - **4**.

5.3.2 Influence of metal as electrode material

The selection of a suitable metal to be used as electrodes is important in order to control the injection of carriers and alignment of the metal's Fermi level to the energy levels of the contacted materials. Additionally, the environment in which a device is expected to operate also imposes conditions on which materials, including electrode materials, will suit the device's operation lifetime.

Previous studies of melanin's charge transport in hydrated conditions were performed using *Au* as electrode material.[115] Thick pellets of melanin were employed and most of the evaporated *Au* electrode area was covered by the silver paste that attached the wiring to the pellet.

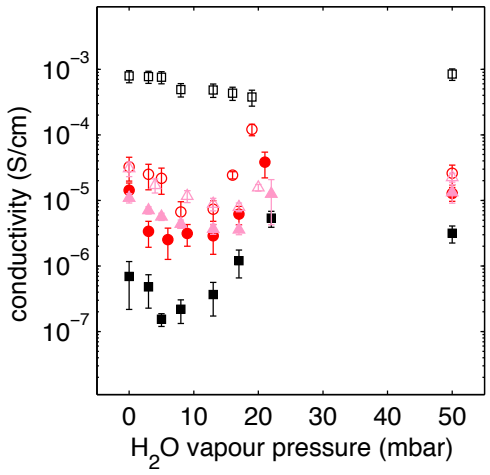


Figure 5.11: Comparison of conductivity of **2:** P3HT(C6OH)$_{10\%}$ (pink *triangles*), **3:** P3HT(C6OH)$_{20\%}$ (red *circles*) and **4:** P3HT(C6OH)$_{50\%}$ (black *squares*), calculated from van der Pauw measurements. *Empty symbols: Au* electrodes. *Solid symbols: Al* electrodes. Ambient conditions are represented in the graph as H_2O vapour pressure of 50 mbar. Error bars calculated using Equation 5.3 (see Section 5.2.2).

Al was chosen as a comparison metal to use in the van der Pauw setup to measure charge transport of P3HT derivatives. Due to the full (or near-full) coverage of the silver paste on the top surface of the electrode, isolation from the hydrated atmosphere was expected to occur, avoiding the long-term formation of a passivation oxide layer.

The conductivity of materials **2** - **4** with *Au* and *Al* electrodes is presented in Figure 5.11.

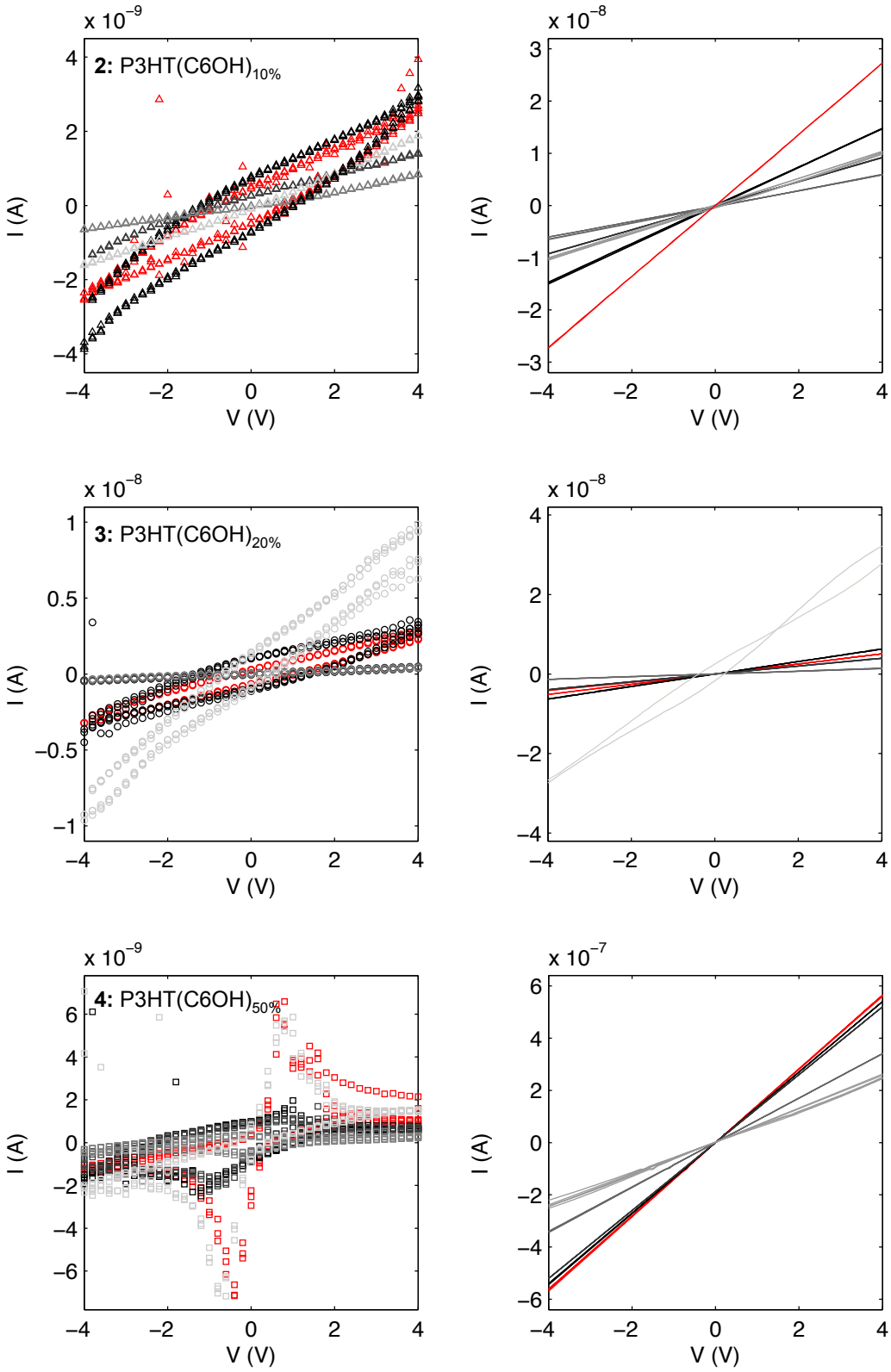


Figure 5.12: Representative I-V curves of thin films measured by 4-point van der Pauw setup as a function of hydration (controlled by the H_2O vapour pressure). *Red*: ambient. From *black*-to-*lighter grey*: subsequently 0, 5, 13 and 22 mbar. **Top-to-bottom: 2:** P3HT(C6OH)$_{10\%}$, **3:** P3HT(C6OH)$_{20\%}$ and **4:** P3HT(C6OH)$_{50\%}$. **Left:** *Al* electrodes. **Right:** *Au* electrodes (from Figures 5.7, 5.8 and 5.9 - left, for materials **2**, **3** and **4**, respectively).

A general overlap of the conductivity data for samples of **2** and **3** is observed for both *Au* and *Al* electrodes. However, approximately three orders of magnitude lower conductivity is measured for the 50 % -OH functionalised derivative **4** when *Al* electrodes were employed, which indicates a strong influence of the chemical environment of the semiconductor on the electrode material.

Despite the similarity of the conductivity trends of **2** and **3**, a comparison of I-V curves when both metals were employed shows an increased hysteresis in the curves' shape for *Al* electrodes (Figure 5.12, top and centre rows). This suggests potential migration of *Al*-oxide species under the applied bias, species which could be generated at the semiconductor/electrode interface.

The extreme differences in conductivity of **4** using *Al* and *Au* show a much more surprising scenario when I-V curves are compared between both metals (Figure 5.12, bottom row). I-V curves using *Al* closely resemble a cyclic voltammogram, where clear faradaic current peaks emerge as H_2O vapour pressure increases. Redox peaks appear at ambient conditions, where H_2O and other molecules are present, reducing their intensity in vacuum and up to 13 mbar. Their reappearance at 22 mbar, with equivalent intensity as in ambient, suggests that the redox reactions are directly related to the presence of water, as well as the nature of the material in contact to the *Al* electrodes (**4**).

Although these findings reassure the fact that **4:** P3HT(C6OH)$_{50\%}$ is an electroactive material in water environments, it is still unclear whether *Al*-oxides, or rather *Al*-hydrates, are active species in the water-assisted electrochemical reaction observed.

Figure 5.13 shows the I-V curves at 22 mbar of two P3HT(C6OH)$_{50\%}$ samples prepared and measured in equivalent conditions. The plots represent all four van der Pauw configurations [(1)] and show that the redox process is genuine and does not depend on the direction (sample orientation) in which current is measured.

[(1)]Notice the positive and negative sweeps here shown are considered as two different configurations in Figure 5.5, whereas here they are clustered and named under one configuration in order to better observe the 'voltammograms'.

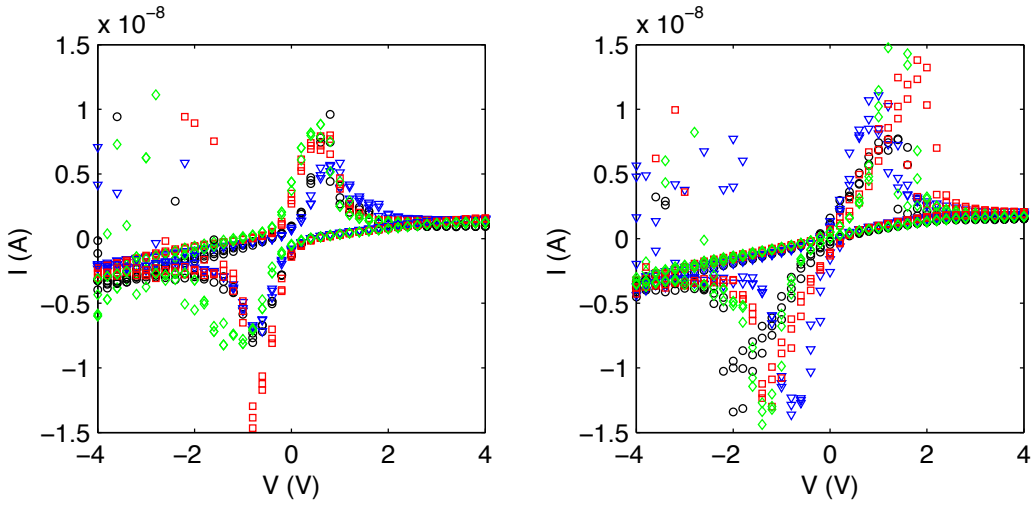


Figure 5.13: I-V curves of material **4:** P3HT(C6OH)$_{50\%}$ at 22 mbar H_2O vapour pressure using *Al* electrodes. Each of the four van der Pauw configurations is shown in a different colour/symbol. **Left:** Sample A. **Right:** Sample B. *Both samples were fabricated and measured in equivalent conditions.*

The calculated cathodic (oxidation) and anodic (reduction) peak voltages are presented in Table 5.1. There is a shift in the redox potentials measured for samples A and B, which may be related to differences in the contact resistance. Sample A presents redox voltages closer to the testing value $V_{ON} = 0.75$ V used during the electrochromic tests in Chapters 3 and 4.

Sample	E_{pc} (V)	E_{pa} (V)
A	0.68 ± 0.2	-0.82 ± 0.2
B	1.3 ± 0.4	-1.4 ± 0.5

Table 5.1: Cathodic (E_{pc}) and anodic (E_{pa}) peak voltages of material **4** at 22 mbar H_2O vapour pressure using *Al* electrodes.

5.3.3 Proton/Electron bilayer conductors

The combination of both ions and electrons as signal (charge) carriers is highly relevant in humid, biological environments. The combination of an ion (proton) conducting solid electrolyte, such as Nafion®, with an electron/hole conducting material, such as P3HT, is studied in the simplest structure that allows scrutinising the interaction between both components (bilayers).

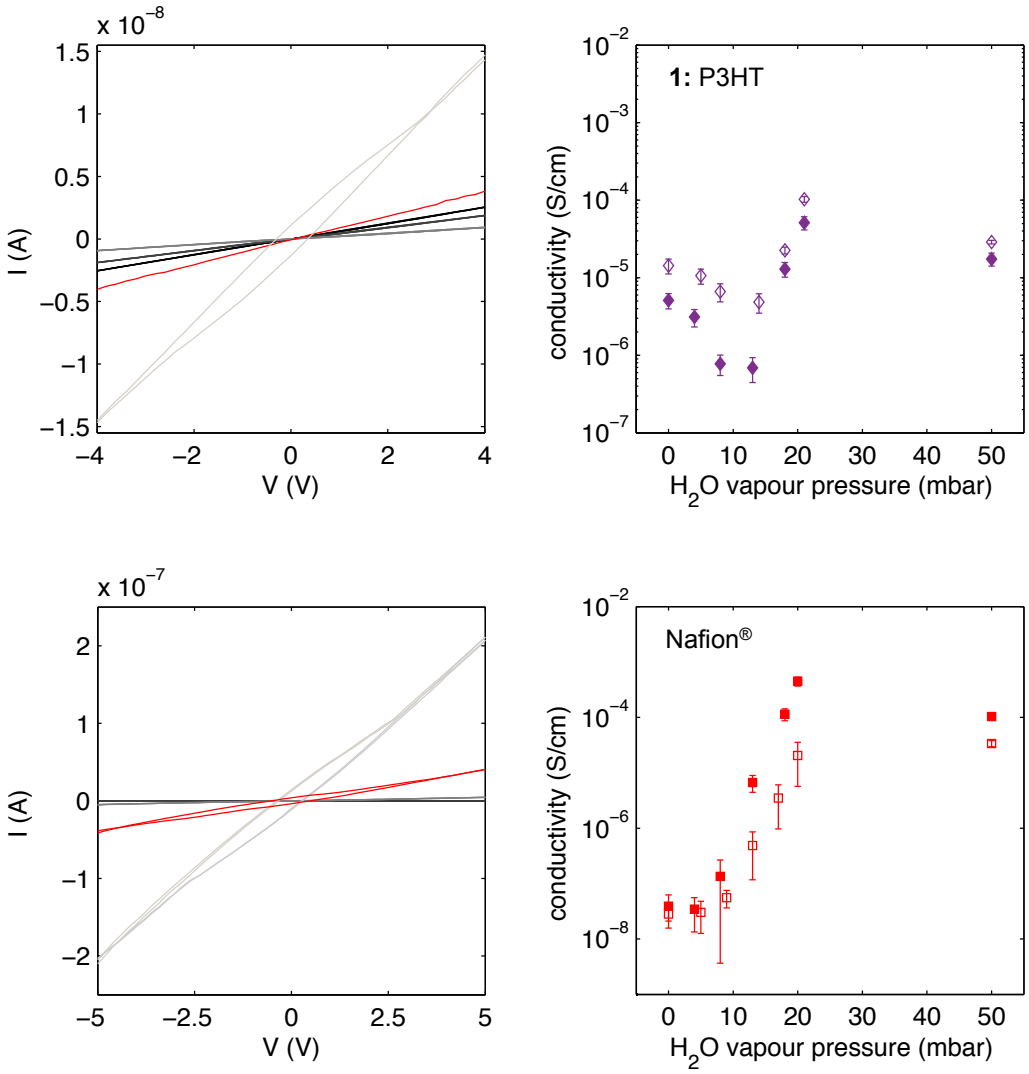


Figure 5.14: Comparison of thin films of samples of **Top:** P3HT and **Bottom:** Nafion®. **Left:** Representative I-V curves measured by 4-point van der Pauw setup as a function of hydration (controlled by the H_2O vapour pressure). *Red*: ambient. From *black*-to-*lighter grey*: subsequently 0, 5, 13 and 22 mbar. **Right:** Conductivity of both materials calculated from van der Pauw measurements. Ambient conditions are represented in the graph as H_2O vapour pressure of 50 mbar. Error bars calculated using Equation 5.3 (see Section 5.2.2).

Figure 5.14 shows the charge transport properties of neat P3HT and Nafion® when tested under controlled humidity conditions (P3HT data (top) correspond to those from Figure 5.6). I-V curves of both systems were ohmic in the full humidity range, displaying hysteresis signs only at 22 mbar. Since Nafion® is a purely proton conductor, it is understood that the increase in conductivity is due to the increase in water content within its bulk, which enhances the mobility of protons as described by the Grotthuss mechanism.[120] Both P3HT and Nafion®'s conductivity increased with H_2O vapour pressure, which can be understood as a signal transduction from humidity to current, or simply as a humidity sensor. It is surprising that ohmic behaviour is observed for Nafion® with no blocking of the protons by the *Au* electrodes.

One Nafion®/P3HT bilayer structure showed promising results; enhanced signal transduction was achieved when the proton conductor was added at the bottom interface (Figure 5.15, top). While increasing current is measured when Nafion® is placed at the bottom interface and P3HT is contacted with *Au* electrodes, a reduction in the current is observed in the inverted bilayer structure (Figure 5.15, bottom). These results clearly indicate that there is a donation/migration of protons from the Nafion® to the P3HT, enhanced by the presence of H_2O vapour, with the subsequent contribution of such ionic charge carriers to the measured current. This contribution is positive when a P3HT top layer is used and the migrated protons sum to the free (mobile) charge carrier present in the semiconductor, hence enhancing the current measured across the *Au* electrodes. However, the contribution is negative when Nafion® is contacted by the *Au* electrodes and the migration of protons is towards the bottom interface (P3HT), producing an effective withdrawal of free charge carriers.

Interestingly, the hysteresis behaviour observed in the Nafion®/P3HT (top) bilayer closely resembles that of a memristor. A memristor is a resistive component whose resistivity depends on its previous I-V history. It was hypothesised by Leon Chua in 1971 as a missing component in circuit theory and an example of a device displaying memristic behaviour was first published by Strukov et al. in 2008.[121,122] In this study the authors proposed a model which connected the mathematical description of a memristor to the physical properties of a practical system. The system was described as containing a charged dopant that could drift within the material, the motion of which, coupled to that of electrons, forms a current-(or voltage-)controlled mem-

ristor. They tested for such behaviour with a nm-scale TiO_2/TiO_{2-x} device, where the oxygen vacancies acted as charged dopants, showing that the hysteresis curves closely resembled the theoretically derived ones.

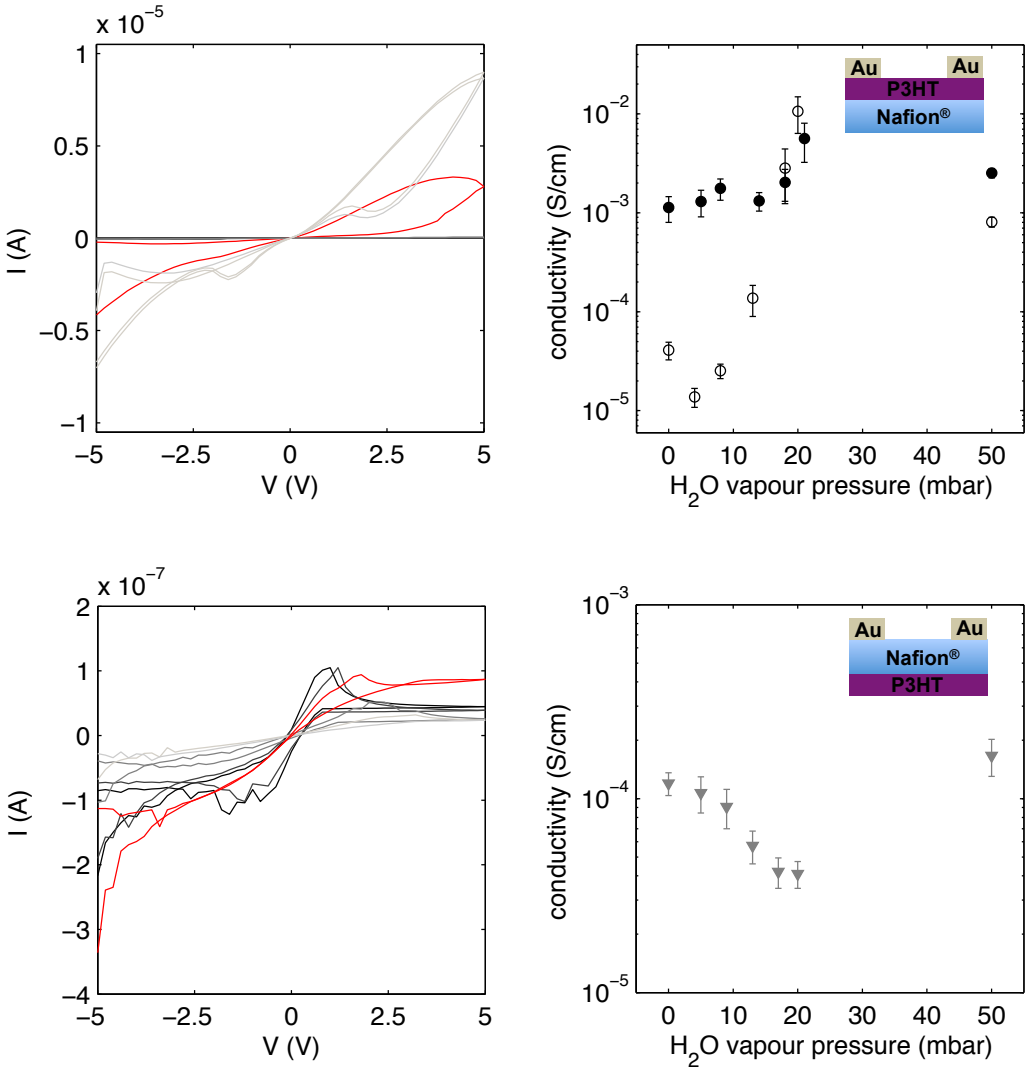


Figure 5.15: Comparison of thin film samples of **Top:** Nafion®/P3HT (top) and **Bottom:** P3HT/Nafion® (top). **Left:** Representative I-V curves measured by 4-point van der Pauw setup as a function of hydration (controlled by the H_2O vapour pressure). *Red*: ambient. From *black*-to-*lighter grey*: subsequently 0, 5, 13 and 22 mbar. **Right:** Conductivity of both bilayers calculated from van der Pauw measurements. In top-right, *empty* and *solid* symbols correspond to two repetitions of equivalent samples. Only one sample was performed in bottom-right. Ambient conditions are represented in the graph as H_2O vapour pressure of 50 mbar. Error bars calculated using Equation 5.3 (see Section 5.2.2).

In a recent report on memristic devices, the I-V characteristics of a mixed ion/electron conductor (GaO_x, x$\sim$ 1.1) showed memristic behaviour, which was explained as being due to the mobility of oxygen at room temperature, and was seen on devices between 50 - 90 nm thick.[123]

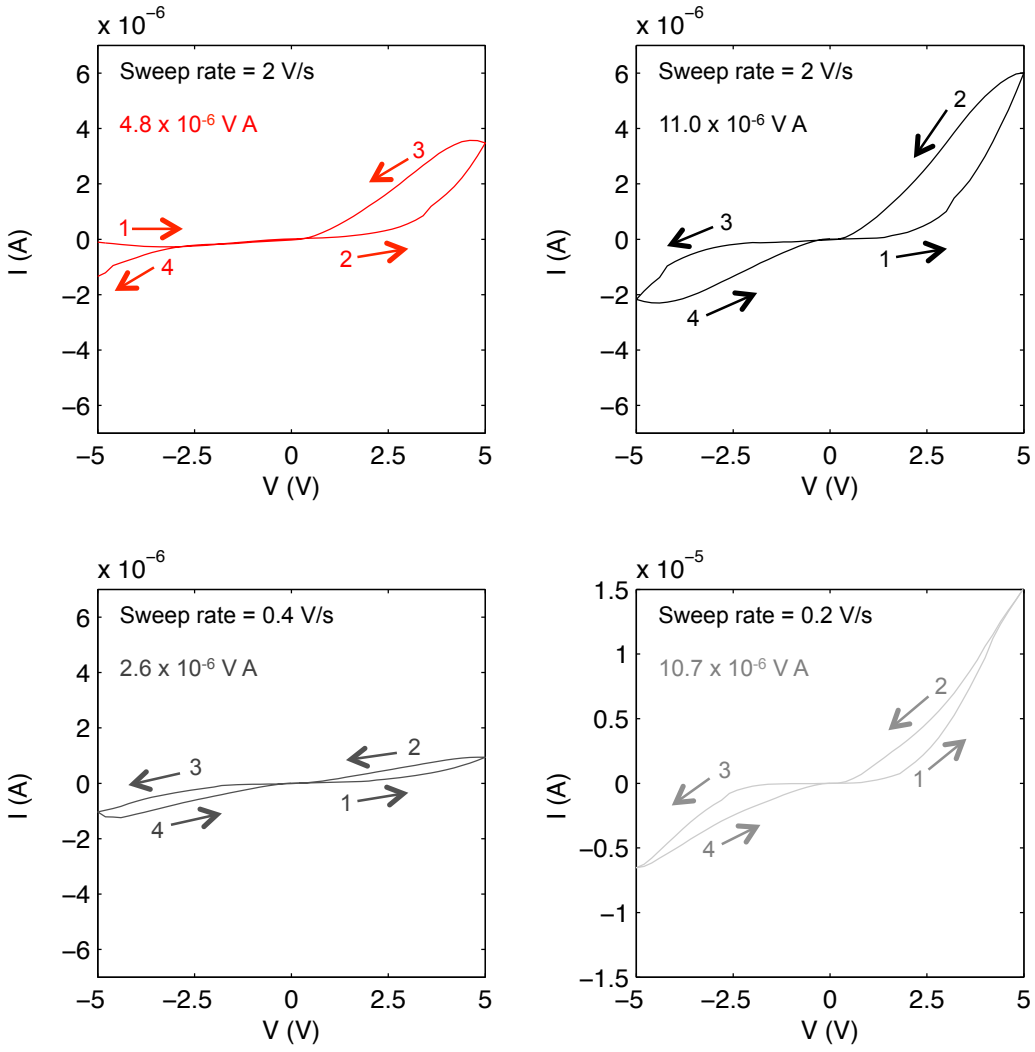


Figure 5.16: I-V curves of Nafion®/P3HT (top) bilayers at 18 mbar H_2O vapour pressure at varying voltage-sweep rates as measured by the van der Pauw method. **Top-left:** bias cycle -5 $\rightarrow$ 5 $\rightarrow$ -5 V. Voltage-sweep rate 2 V/s. **Top-right:** 0 $\rightarrow$ 5 $\rightarrow$ 0 $\rightarrow$ -5 $\rightarrow$ 0 V. Voltage-sweep rate 2 V/s. **Bottom:** Bias cycle starting at 0 V with varying voltage-sweep rates (left - 0.4 V/s, right - 0.2 V/s). *Numbers inside the plot indicate the integrated area of the loops of each graph (hysteretic area).*

It is interesting that the description of the physical properties by Strukov, proved by Aoki, relates to the Nafion®/P3HT bilayer system, since it is observed that the system is mixed

conducting (ionic/electronic) and protons (charged dopants) migrate from the Nafion® into the P3HT layer.

Figure 5.16 (top-left) shows the hysteresis curves at 18 mbar, the humidity onset to the observed loop. Notice that all the previous I-V curves, including this one, have followed a voltage sweep -5 V → 5 V → -5 V (see the four numbered sections of the sweep and direction of the arrows), whereas the above memristor studies[122,123] always performed voltage loops starting at 0 V, followed by: positive bias, negative bias and returning to 0 V. Since a memristor's resistive state depends on its history, it was interesting to test the sample with a voltage cycle resembling those in literature. Figure 5.16 (top-right) shows the I-V curve when the voltage sweep was modified to start from 0 V and suggests that the device has a memristic behaviour, since the loops here obtained closely resemble those from Aoki's work.[123] Memristors hysteretic area in the I-V has previously been shown to decrease with increasing voltage-sweep rates. Some preliminary investigations were done on the behaviour of the Nafion®/P3HT (top) devices when the voltage-sweep rate was changed. Although the area of the curves changed with the voltage-sweep rates, the trend was somewhat unclear (Figure 5.16, compare top-right, bottom-left and bottom-right). Another observation is the direction of the loops, which differs from those previously published.

It is most remarkable, however, that what is observed in the Nafion®/P3HT system (orders of magnitude switch of conductivity with humidity along with displaying large hysteresis at vapour pressures $>$ 18 mbar), takes place in device structures with transport channels in the mm-scale, four orders of magnitude larger than the nm-scale devices previously reported. Hence, further optimisation and experimenting would be of great interest to prove (os disprove) the potential of these bilayers as memristic devices.

Finally, Figure 5.17 summarises the results of the neat materials (P3HT and Nafion®) and their corresponding bilayers. The conductivity of Nafion®/P3HT (top) at high hydration conditions (22 mbar) is larger than the addition of the protonic (from Nafion®) and the electronic contribution (from P3HT). Whereas Nafion® is an order of magnitude more conducting than P3HT, the bilayer presents an increase in conductivity of three orders of magnitude. The intimate in-

teraction between the charge carriers of Nafion® (of protonic nature) and P3HT (of electronic nature) is encouraging for further optimisation of what seems like a promising sensing system.

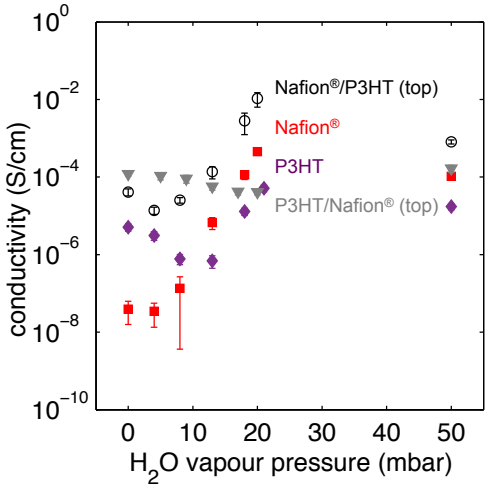


Figure 5.17: Comparison of conductivity of **1:** P3HT (purple *diamonds*), Nafion® (red *squares*) and bilayers Nafion®/P3HT (top) (black *circles*) and P3HT/Nafion® (top) (grey *triangles*), calculated from van der Pauw measurements. Ambient conditions are represented in the graph as H_2O vapour pressure of 50 mbar.

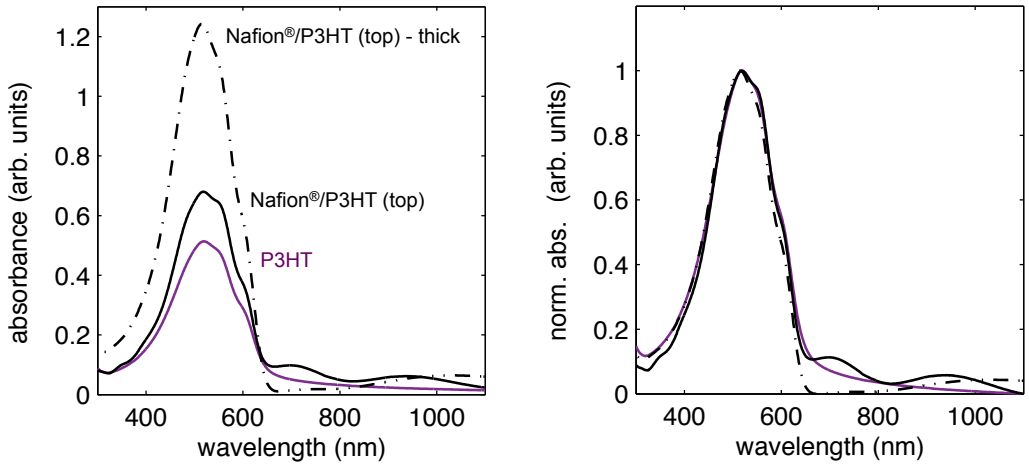


Figure 5.18: UV-Visible absorbance spectra of thin films of P3HT and Nafion®/P3HT (top) bilayers. **Left:** raw absorbance. **Right:** normalised to maximum absorbance. *A thicker bilayer film is also shown (approx. twice as thick, as observed by the doubled absorbance strength).*

At ambient conditions, it is observed that the conductivity of P3HT/Nafion® (top) is equivalent to that of Nafion®, whereas the addition of an underlying Nafion® layer in the Nafion®/P3HT (top) bilayer structure leads to larger conductivity than P3HT. This suggests that the migration of protons takes place at room temperature (RT) and ambient conditions of humidity.

UV-Vis absorbance spectra revealed that bilayers of Nafion®/P3HT (top) appear doped, as observed by the polaron and bi-polaron peaks around 700 nm and 950 nm of the thin bilayer (Figure 5.18, left). Thicker structures, also shown in the plot, displayed a broad tail at high wavelengths, also characteristic of the presence of free charge carriers. The normalised absorbance spectra (Figure 5.18, right) clearly show that the presence Nafion® does not affect the short-range order of P3HT and only an effective protonation of the semiconductor is observed.

5.4 Conclusions

Materials that support mixed transport have become of great interest in many fields, but it has also proven difficult to even distinguish between ionic and electronic charge species.[116] In previous chapters the ability of a certain P3HT derivative to act as an ion-to-electron transducing interface was demonstrated (Chapter 3) and its ionic transport further enhanced by carefully blending it with polar insulators (Chapter 4). The electrochemical doping of the material played a central role in the study of such mixed transport properties.

In this Chapter the influence of moisture on the charge transport of the same range of thiophene-based polymers, from P3HT to the more hydrophilic P3HT derivative containing 50 % OH-functionalised monomers, was studied under controlled hydration levels. Although the trends of the doping profile, as a function of hydration, with OH-content were unclear, some interesting observations could be made for P3HT and P3HT(C6OH)$_{20\%}$. At high humidity level, these two systems had higher conductivity than at ambient, and also showed some hysteresis in their I-V curves, which may be an indication of ionic transport. A distinct behaviour was observed for the 'self-doped' system P3HT(C6OH)$_{50\%}$, the conductivity of which was an order of magnitude larger than any other polymer and whose charge transport was negatively affected by the presence of vapour water. This system also showed interesting redox behaviour when contacted by *Al* electrodes; water vapour, as well as the density of -OH moieties of the polymer, seems to assist the redox reactions. Further research is required to learn about the specific chemistry which takes place in such specific conditions.

Finally, a bilayer system composed of Nafion®/P3HT showed interesting memristic behaviour. This hypothesis is based on the modulation of the hysteretic area observed with voltage-sweep rate as well as changes in the I-V curves shape with the starting voltage of the bias cycle. Previous reports describe memristic devices with a transport model of mixed charge carriers, ions (protons) and electrons/holes, that resembles some of the conditions of the bilayer system. Overall, the system was highly responsive to humidity and varying the structures of the bilayers seems to indicate that there is migration of protons from Nafion® to P3HT, effectively doping the semiconductor even at ambient conditions.

Further understanding of the intimate interaction of Nafion® with P3HT will be interesting for the re-design and optimisation of devices based on this hybrid system. Their potential applications range from humidity sensors, to memristors, as well as furthering the basic knowledge of the research community on the transport physics in hybrid systems.

Summary of thesis achievements

Polythiophene co-polymers offer a versatile design approach to study the effect of polar moieties, specifically -OH functional groups, in the material's ability to dope/dedope electrochemically. The charge transport and short-range order of such co-polymer derivatives was shown to be maintained upon -OH functionalisation, with up to 50 % functionalised monomers. Increasing functionalisation proved beneficial to ionic transport, which was indirectly observed by the faster electrochemical oxidation of the materials with larger functionalisation level, when tested with an aqueous electrolyte. The most hydrophilic system showed a promising response as an ion-to-electron converter when benchmarked with poly(3,4-ethylenedioxythiophene):poly(styrene sulfonate) (PEDOT:PSS). Due to being initially undoped, polythiophene co-polymer poly[(3-hexylthiophene)-co-(3-(6-hydroxyhexyl)thiophene)] with 50 % functionalisation level, labelled as P3HT(C6OH)$_{50\%}$, could be explored as the active layer for accumulation organic electrochemical transistors (OECTs). Due to the electrochemical doping of the channel when a gate voltage is applied, charges (free carriers) accumulate in the channel and the current increases. The oxidation speed, in the order of seconds, was comparable to PEDOT:PSS in an equivalent setup. Optimisation and miniaturisation of the devices employed may lead to desirably faster responses. Blending P3HT(C6OH)$_{50\%}$ with poly(vinyl alcohol) (PVA) proved to enhance ionic transport, which seemed to correlate to an improved ability to swell in water. A distinct time decay was associated with the presence of PVA, and the benefit of blending may be extended to other polar components, as it was also shown for a polar derivative of poly(methyl methacrylate) (PMMA). Ionic transport presented a complex multi-decay time dependency and for the first time an insight was given on associating these rates to charge transport in the amorphous and aggregated phases of the semi-crystalline co-polymer. Controlled humidity affected charge transport of polythiophene derivatives differently, although no clear relation to their -OH functionalisation level was found. Signs of ionic transport, based on hysteresis in I-V characteristics and larger conductivities, could be attributed to no or low functionalisation levels. The multi-component system formed by the proton conductor Nafion® and poly(3-hexylthiophene) (P3HT), in a bilayer structure, showed clear protonation of the semiconductor. The strong interaction between the components conferred interesting sensing properties to the system in humid environments as well as I-V features that closely resembled those of memristors, which

could lead to deeper understanding of the complex mixed transport physics and the design of novel architectures for sensing or other applications such as memory devices.

Bibliography

1. M. Pera, *The Ambiguous Frog.* 1992.

2. J. Walsh, "Of the Electric Property of the Torpedo," *Philos. Trans. R. Soc.*, vol. 63, pp. 461 – 480, 1773.

3. R. M. Owens and G. G. Malliaras, "Organic Electronics at the Interface with Biology," *MRS Bull.*, vol. 35, pp. 449 – 456, 2010.

4. N. Amdursky, D. Marchak, L. Sepunaru, I. Pecht, M. Sheves, and D. Cahen, "Electronic Transport via Proteins," *Adv. Mater.*, vol. 26, pp. 7142 – 7161, 2014.

5. G. S. Dhillon, S. M. Lawrence, D. T. Hutchinson, and K. W. Horch, "Residual function in peripheral nerve stumps of amputees: Implications for neural control of artificial limbs," *J. Hand Surg. Am.*, vol. 29, no. 4, pp. 605 – 615, 2004.

6. G. G. Wallace, S. E. Moulton, and G. M. Clark, "Electrode-Cellular Interface," *Science*, vol. 324, pp. 185 – 186, 2009.

7. R. Green and M. R. Abidian, "Conducting Polymers for Neural Prosthetic and Neural Interface Applications," *Adv. Mater.*, vol. 27, no. 46, pp. 7620 – 7637, 2015.

8. M. J. P. Raatikainen, D. O. Arnar, K. Zeppenfeld, J. L. Merino, F. Levya, G. Hindriks, and K. H. Kuck, "Statistics on the use of cardiac electronic devices and electrophysiological procedures in the European Society of Cardiology countries: 2014 report from the European Heart Rhythm Association," *Europace*, vol. 17, pp. i1 – i75, 2015.

9. A. Djourno, C. Eyriès, and B. Vallencien, "De l'excitation électrique du nerf cochleaire chez l'homme, par induction à distance, à l'aide d'un micro-bobinage inclus à demeure," *Comptes Rendus Soc. Biol. Paris*, pp. 423 – 424, 1957.

10. L. D. Raeve and R. V. Hardeveld, "Prevalence of cochlear implants in Europe: what do we know and what can we expect?," *J. Hear. Sci.*, vol. 3, no. 4, pp. 9 – 16, 2013.

11. R. Hassler, T. Riechert, F. Mundinger, W. Umbach, and J. A. Ganglberger, "Physiological observations in stereotaxic operations in extrapyramidal motor disturbances," *Brain*, vol. 83, pp. 337 – 350, 1960.

12. J. S. Perlmutter and J. W. Mink, "Deep Brain Stimulation," *Annu. Rev. Neurosci.*, vol. 29, pp. 229 – 257, 2006.

13. N. S. Oliver, C. Toumazou, A. E. G. Cass, and D. G. Johnston, "Glucose sensors: A review of current and emerging technology," *Diabet. Med.*, vol. 26, no. 3, pp. 197 – 210, 2009.

14. E. Stavrinidou, R. Gabrielsson, E. Gomez, X. Crispin, O. Nilsson, D. T. Simon, and M. Berggren, "Electronic plants," *Sci. Adv.*, vol. 1, no. 10, pp. 1 – 8, 2015.

15. Kristoffer Famm, "A jump-start for electroceuticals," *Nature*, vol. 496, pp. 159 – 161, 2013.

16. B. K. D. Wise, A. M. Sodagar, Y. Yao, M. N. Gulari, G. E. Perlin, and K. Najafi, "Microelectrodes, Microelectronics, and Implantable Neural Microsystems," *Proc. IEEE*, vol. 96, no. 7, pp. 1184 – 1202, 2008.

17. S. R. Forrest, "The path to ubiquitous and low-cost organic electronic appliances on plastic.," *Nature*, vol. 428, pp. 911 – 918, 2004.

18. J. M. Leger, "Organic Electronics: The Ions Have It," *Adv. Mater.*, vol. 20, no. 4, pp. 837 – 841, 2008.

19. H. Sai, K. W. Tan, K. Hur, E. Asenath-Smith, R. Hovden, Y. Jiang, M. Riccio, D. A. Muller, V. Elser, L. A. Estroff, S. M. Gruner, and U. Wiesner, "Hierarchical Porous

Polymer Scaffolds from Block Copolymers," *Science*, vol. 341, no. 6145, pp. 530 – 534, 2013.

20. L. H. Jimison, A. Hama, X. Strakosas, V. Armel, D. Khodagholy, E. Ismailova, G. G. Malliaras, B. Winther-Jensen, and R. M. Owens, "PEDOT:TOS with PEG: a biofunctional surface with improved electronic characteristics," *J. Mater. Chem.*, vol. 22, no. 37, pp. 19498 – 19505, 2012.

21. J. T. Mabeck and G. G. Malliaras, "Chemical and biological sensors based on organic thin-film transistors," *Anal. Bioanal. Chem.*, vol. 384, no. 2, pp. 343 – 353, 2006.

22. D. A. Bernards and G. G. Malliaras, "Steady-State and Transient Behavior of Organic Electrochemical Transistors," *Adv. Funct. Mater.*, vol. 17, pp. 3538 – 3544, 2007.

23. N. K. Guimard, N. Gomez, and C. E. Schmidt, "Conducting polymers in biomedical engineering," *Prog. Polym. Sci.*, vol. 32, pp. 876 – 921, 2007.

24. D. Mawad, E. Stewart, D. L. Officer, T. Romeo, P. Wagner, K. Wagner, and G. G. Wallace, "A Single Component Conducting Polymer Hydrogel as a Scaffold for Tissue Engineering," *Adv. Funct. Mater.*, vol. 22, no. 13, pp. 2692 – 2699, 2012.

25. R. Balint, N. J. Cassidy, and S. H. Cartmell, "Conductive polymers: Towards a smart biomaterial for tissue engineering," *Acta Biomater.*, vol. 10, pp. 2341 – 2353, 2014.

26. M. Sasaki, B. C. Karikkineth, K. Nagamine, H. Kaji, K. Torimitsu, and M. Nishizawa, "Highly conductive stretchable and biocompatible electrode-hydrogel hybrids for advanced tissue engineering," *Adv. Healthc. Mater.*, vol. 3, pp. 1919 – 1927, 2014.

27. M. Abidian, D. H. Kim, and D. C. Martin, "Conducting-Polymer Nanotubes for Controlled Drug Release.," *Adv. Mater.*, vol. 18, no. 4, pp. 405 – 409, 2006.

28. R. A. Green, S. Baek, L. A. Poole-Warren, and P. J. Martens, "Conducting polymer-hydrogels for medical electrode applications," *Sci. Technol. Adv. Mater.*, vol. 11, no. 1, p. 14107, 2010.

29. G. M. Spinks, B. Xi, V. T. Truong, and G. G. Wallace, "Actuation behaviour of layered composites of polyaniline, carbon nanotubes and polypyrrole," *Synth. Met.*, vol. 151, pp. 85 – 91, 2005.

30. R. K. Cheedarala, J. H. Jeon, C. D. Kee, and I. K. Oh, "Bio-inspired all-organic soft actuator based on a π-π stacked 3D ionic network membrane and ultra-fast solution processing," *Adv. Funct. Mater.*, vol. 24, no. 38, pp. 6005 – 6015, 2014.

31. K. a. Ludwig, N. B. Langhals, M. D. Joseph, S. M. Richardson-Burns, J. L. Hendricks, and D. R. Kipke, "Poly(3,4-ethylenedioxythiophene) (PEDOT) polymer coatings facilitate smaller neural recording electrodes.," *J. Neural Eng.*, vol. 8, p. 014001, 2011.

32. D. Khodagholy, T. Doublet, M. Gurfinkel, P. Quilichini, E. Ismailova, P. Leleux, T. Herve, S. Sanaur, C. Bernard, and G. G. Malliaras, "Highly Conformable Conducting Polymer Electrodes for In Vivo Recordings.," *Adv. Mater.*, vol. 23, pp. 268 – 272, 2011.

33. A. J. Heeger, "Semiconducting and Metallic Polymers: The Fourth Generation of Polymeric Materials (Nobel Lecture)," *Angew. Chem. Int. Ed.*, vol. 40, pp. 2591 – 2611, 2001.

34. R. Peierls, *Quantum Theory of Solids*. Oxford University Press, 1955.

35. A. J. Heeger, S. Kivelson, J. R. Schrieffer, and W. P. Su, "Solitons in conducting polymers," *Rev. Mod. Phys.*, vol. 60, no. 3, pp. 781 – 850, 1988.

36. U. Rauscher, H. Bassler, D. D. C. Bradley, and M. H. Hennecke, "Exciton versus band description of the absorption and luminescence spectra in poly(p-phenylenevinylene)," *Phys. Rev. B*, vol. 42, no. 16, pp. 9830 – 9836, 1991.

37. R. Noriega, J. Rivnay, K. Vandewal, F. P. V. Koch, N. Stingelin, P. Smith, M. F. Toney, and A. Salleo, "A general relationship between disorder, aggregation and charge transport in conjugated polymers," *Nat. Mater.*, vol. 12, no. 11, pp. 1038 – 1044, 2013.

38. K. Walzer, B. Maennig, M. Pfeiffer, and K. Leo, "Highly efficient organic devices based on electrically doped transport layers," *Chem. Rev.*, vol. 107, no. 4, pp. 1233 – 1271, 2007.

39. S. M. Sze and K. N. Kwok, *Physics of semiconductors*. Hoboken, New Jersey: John Wiley & Sons, Inc., third ed., 2007.

40. M. Pfaiffer, T. Fritz, J. Blochwitz, A. Nollau, B. Plönnigs, A. Beyer, and K. Leo, "Controlled doping of molecular organic layers: Physics and device prospects," *Adv. Solid State Phys.*, vol. 39, pp. 77 – 90, 1999.

41. R. H. Friend, D. C. Bott, D. D. C. Bradley, C. K. Chai, W. J. Feast, P. J. S. Foot, J. R. M. Giles, M. E. Horton, C. M. Pereira, and P. D. Townsend, "Electronic Properties of Conjugated Polymers," *Philos. Trans. R. Soc. London*, vol. A314, no. 1528, pp. 37 – 49, 1985.

42. J. E. De Albuquerque, L. H. C. Mattoso, R. M. Faria, J. G. Masters, and A. G. MacDiarmid, "Study of the interconversion of polyaniline oxidation states by optical absorption spectroscopy," *Synth. Met.*, vol. 146, no. 1, pp. 1 – 10, 2004.

43. E. F. Aziz, A. Vollmer, S. Eisebitt, W. Eberhardt, P. Pingel, D. Neher, and N. Koch, "Localized Charge Transfer in a Molecularly Doped Conducting Polymer," *Adv. Mater.*, vol. 19, no. 20, pp. 3257 – 3260, 2007.

44. J. H. Schon, C. Kloc, E. Bucher, and B. Batlogg, "Efficient organic photovoltaic diodes based on doped pentacene.," *Nature*, vol. 403, no. 6768, pp. 408 – 410, 2000.

45. Y. Zhang and P. W. M. Blom, "Enhancement of the hole injection into regioregular poly(3-hexylthiophene) by molecular doping," *Appl. Phys. Lett.*, vol. 97, no. 8, p. 083303, 2010.

46. A. G. MacDiarmid, ""Synthetic metals": A novel role for organic polymers (Nobel lecture)," *Angew. Chemie - Int. Ed.*, vol. 40, no. 14, pp. 2581 – 2590, 2001.

47. L. Cosimbescu, A. B. Padmaperuma, and D. J. Gaspar, "7,7,8,8-Tetracyanoquinodimethane-Based Molecular Dopants for p-Type Doping of OLEDs : A Theoretical Investigation," *J. Phys. Chem. A*, vol. 115, pp. 13498–13503, 2011.

48. S. Guo, S. B. Kim, S. K. Mohapatra, Y. Qi, T. Sajoto, A. Kahn, S. R. Marder, and

S. Barlow, "n-Doping of organic electronic materials using air-stable organometallics.," *Adv. Mater.*, vol. 24, no. 5, pp. 699 – 703, 2012.

49. O. Inganäs, "Hybrid electronics and electrochemistry with conjugated polymers," *Chem. Soc. Rev.*, vol. 39, no. 7, pp. 2633 – 2642, 2010.

50. X. Cui, J. F. Hetke, J. A. Wiler, D. J. Anderson, and D. C. Martin, "Electrochemical deposition and characterization of conducting polymer polypyrrole / PSS on multichannel neural probes," *Sensors Actuators A Phys.*, vol. 93, pp. 8 – 18, 2001.

51. X. Cui and D. D. Zhou, "Poly (3,4-Ethylenedioxythiophene) for Chronic Neural Stimulation," *IEEE Trans. Neural Syst. Rehabil. Eng.*, vol. 15, no. 4, pp. 502 – 508, 2007.

52. M. Asplund, T. Nyberg, and O. Inganäs, "Electroactive polymers for neural interfaces," *Polym. Chem.*, vol. 1, no. 9, p. 1374, 2010.

53. R. Baughman, "Conducting polymer artificial muscles," *Synth. Met.*, vol. 78, no. 3, pp. 339 – 353, 1996.

54. J. M. Leger, M. Berggren, and S. Carter, *Iontronics: Ionic Carriers in Organic Electronic Materials and Devices*. Taylor & Francis, 2010.

55. K. Tybrandt, R. Forchheimer, and M. Berggren, "Logic gates based on ion transistors," *Nat. Commun.*, vol. 3, p. 871, 2012.

56. G. Tarabella, F. Mahvash Mohammadi, N. Coppedè, F. Barbero, S. Iannotta, C. Santato, and F. Cicoira, "New opportunities for organic electronics and bioelectronics: ions in action," *Chem. Sci.*, vol. 4, no. 4, pp. 1395 – 1409, 2013.

57. D. Khodagholy, J. Rivnay, M. Sessolo, M. Gurfinkel, P. Leleux, L. H. Jimison, E. Stavrinidou, T. Herve, S. Sanaur, R. M. Owens, and G. G. Malliaras, "High transconductance organic electrochemical transistors.," *Nat. Commun.*, vol. 4, p. 2133, 2013.

58. J. Rivnay, P. Leleux, M. Sessolo, D. Khodagholy, T. Hervé, M. Fiocchi, and G. G. Malliaras, "Organic electrochemical transistors with maximum transconductance at zero gate bias," *Adv. Mater.*, vol. 25, no. 48, pp. 7010 – 7014, 2013.

59. G. P. Kittlesen, H. S. White, and M. S. Wrighton, "Chemical Derivatization of Microelectrode Arrays by Oxidation of Pyrrole and N-Methylpyrrole: Fabrication of Moleule-Based Electronic Devices," *J. Am. Chem. Soc.*, vol. 106, no. 24, pp. 7389 – 7396, 1984.

60. X. Strakosas, M. Sessolo, A. Hama, J. Rivnay, E. Stavrinidou, G. G. Malliaras, and R. M. Owens, "A facile biofunctionalisation route for solution processable conducting polymer devices," *J. Mater. Chem. B*, vol. 2, no. 17, pp. 2537 – 2545, 2014.

61. S. Inal, J. Rivnay, P. Leleux, M. Ferro, M. Ramuz, J. C. Brendel, M. M. Schmidt, M. Thelakkat, and G. G. Malliaras, "A High Transconductance Accumulation Mode Electrochemical Transistor," *Adv. Mater.*, vol. 26, no. 44, pp. 7450 – 7455, 2014.

62. R. H. Friend, R. W. Gymer, A. B. Holmes, J. H. Burroughes, R. Marks, C. Taliani, D. D. C. Bradley, D. A. Dos Santos, J. L. Bredas, M. Logdlund, and W. R. Salaneck, "Electroluminescence in conjugated polymers," *Nature*, vol. 397, pp. 121 – 128, 1999.

63. A. Facchetti, "π-Conjugated Polymers for Organic Electronics and Photovoltaic Cell Applications," *Chem. Mater.*, vol. 23, no. 3, pp. 733 – 758, 2011.

64. D. M. Hercules, "Chemiluminescence Resulting from Electrochemically Generated Species," *Science*, vol. 145, pp. 808 – 809, 1964.

65. Q. Pei, G. Yu, C. Zhang, Y. Yang, and a. J. Heeger, "Polymer light-emitting electrochemical cells," *Science*, vol. 269, pp. 1086 – 1088, 1995.

66. N. C. Foulds and C. R. Lowe, "Enzyme Entrapment in Electrically Conducting Polymers," *J. Chem. Soc.*, vol. 82, pp. 1259 – 1264, 1986.

67. H. Xie, S.-C. Luo, and H.-H. Yu, "Electric-field-assisted growth of functionalized poly(3,4-ethylenedioxythiophene) nanowires for label-free protein detection," *Small*, vol. 5, no. 22, pp. 2611 – 2617, 2009.

68. H. Peng, L. Zhang, C. Soeller, and J. Travas-Sejdic, "Conducting polymers for electrochemical DNA sensing," *Biomaterials*, vol. 30, no. 11, pp. 2132 – 2148, 2009.

69. Q. Pei and O. Inganäs, "Conjugated polymers and the bending cantilever method: Electrical muscles and smart devices," *Adv. Mater.*, vol. 4, no. 4, pp. 277 – 278, 1992.

70. E. W. Jager, O. Inganäs, and I. Lundström, "Microrobots for micrometer-size objects in aqueous media: potential tools for single-cell manipulation," *Science*, vol. 288, no. 5475, pp. 2335 – 2338, 2000.

71. K. Kaneto, M. Kaneko, Y. Min, and A. G. MacDiarmid, ""Artificial muscle": Electromechanical actuators using polyaniline films," *Synth. Met.*, vol. 71, pp. 2211 – 2212, 1995.

72. Q. Pei, G. Zuccarello, M. Ahlskogt, and O. Inganäs, "Electrochromic and highly stable poly(3,4-ethylenedioxythiophene) switches between opaque blue-black and transparent sky blue," *Polymer (Guildf).*, vol. 35, no. 7, pp. 1347 – 1351, 1994.

73. P. Tehrani, L.-O. Hennerdal, A. L. Dyer, J. R. Reynolds, and M. Berggren, "Improving the contrast of all-printed electrochromic polymer on paper displays," *J. Mater. Chem.*, vol. 19, no. 13, pp. 1799 – 1802, 2009.

74. X. Li and J. Kolega, "Effects of direct current electric fields on cell migration and actin filament distribution in bovine vasclar endothelial cells," *J. Vasc. Res.*, vol. 39, pp. 391 – 404, 2002.

75. J. a. Genovese, C. Spadaccio, J. Langer, J. Habe, J. Jackson, and A. N. Patel, "Electrostimulation induces cardiomyocyte predifferentiation of fibroblasts.," *Biochem. Biophys. Res. Commun.*, vol. 370, no. 3, pp. 450 – 455, 2008.

76. R. Balint, N. J. Cassidy, and S. H. Cartmell, "Electrical Stimulation: A Novel Tool for Tissue Engineering," *Tissue Eng. Part B Rev.*, vol. 19, no. 1, pp. 48 – 57, 2013.

77. S. Ghosh and O. Inganäs, "Networks of Electron-Conducting Polymer in Matrices of Ion-Conducting Polymers. Applications to Fast Electrodes," *Electrochem. Solid-State Lett.*, vol. 3, no. 5, pp. 213 – 215, 2000.

78. J. Rivnay, R. M. Owens, and G. G. Malliaras, "The Rise of Organic Bioelectronics," *Chem. Mater.*, vol. 26, no. 1, pp. 679 – 685, 2014.

79. J. G. Hardy, J. Y. Lee, and C. E. Schmidt, "Biomimetic conducting polymer-based tissue scaffolds," *Curr. Opin. Biotechnol.*, vol. 24, no. 5, pp. 847 – 854, 2013.

80. E. Stavrinidou, P. Leleux, H. Rajaona, D. Khodagholy, J. Rivnay, M. Lindau, S. Sanaur, and G. G. Malliaras, "Direct Measurement of Ion Mobility in a Conducting Polymer," *Adv. Mater.*, vol. 25, pp. 4488 – 4493, 2013.

81. E. Stavrinidou, O. Winther-Jensen, B. S. Shekibi, V. Armel, J. Rivnay, E. Ismailova, S. Sanaur, G. G. Malliaras, and B. Winther-Jensen, "Engineering hydrophilic conducting composites with enhanced ion mobility," *Phys. Chem. Chem. Phys.*, vol. 16, no. 6, pp. 2275 – 2279, 2014.

82. Y. M. Chang, W. F. Su, and L. Wang, "Influence of photo-induced degradation on the optoelectronic properties of regioregular poly(3-hexylthiophene)," *Sol. Energy Mater. Sol. Cells*, vol. 92, no. 7, pp. 761 – 765, 2008.

83. G. Scarpa, A.-L. Idzko, S. Götz, and S. Thalhammer, "Biocompatibility studies of functionalized regioregular poly(3-hexylthiophene) layers for sensing applications," *Macromol. Biosci.*, vol. 10, no. 4, pp. 378 – 383, 2010.

84. L. Groenendaal, G. Zotti, P.-H. Aubert, S. Waybright, and J. Reynolds, "Electrochemistry of Poly(3,4-alkylenedioxythiophene) Derivatives," *Adv. Mater.*, vol. 15, no. 11, pp. 855 – 879, 2003.

85. E. Zeglio, M. Vagin, C. Musumeci, F. N. Ajjan, R. Gabrielsson, X. T. Trinh, N. T. Son, A. Maziz, N. Solin, and O. Inganäs, "Conjugated Polyelectrolyte Blends for Electrochromic and Electrochemical Transistor Devices," *Chem. Mater.*, vol. 27, no. 18, pp. 6385 – 6393, 2015.

86. D. Khodagholy, M. Gurfinkel, E. Stavrinidou, P. Leleux, T. Herve, S. Sanaur, and G. G. Malliaras, "High speed and high density organic electrochemical transistor arrays," *Appl. Phys. Lett.*, vol. 99, no. 16, p. 163304, 2011.

87. M. Sessolo, J. Rivnay, E. Bandiello, G. G. Malliaras, and H. J. Bolink, "Ion-Selective Organic Electrochemical Transistors," *Adv. Mater.*, vol. 26, no. 28, pp. 4803 – 4807, 2014.

88. R. J. Kline, M. D. McGehee, E. N. Kadnikova, J. Liu, and J. M. J. Fréchet, "Controlling the field-effect mobility of regioregular polythiophene by changing the molecular weight," *Adv. Mater.*, vol. 15, no. 18, pp. 1519 – 1522, 2003.

89. P. Schilinsky, U. Asawapirom, U. Scherf, M. Biele, and C. J. Brabec, "Influence of the molecular weight of poly(3-hexylthiophene) on the performance of bulk heterojunction solar cells," *Chem. Mater.*, vol. 17, no. 8, pp. 2175 – 2180, 2005.

90. A. Giovannitti, C. B. Nielsen, J. Rivnay, M. Kirkus, D. J. Harkin, A. J. White, H. Sirringhaus, G. G. Malliaras, and I. McCulloch, "Sodium and Potassium Ion Selective Conjugated Polymers for Optical Ion Detection in Solution and Solid State," *Adv. Funct. Mater.*, vol. 26, no. 4, pp. 514 – 523, 2015.

91. E. Stavrinidou, P. Leleux, H. Rajaona, M. Fiocchi, S. Sanaur, and G. G. Malliaras, "A simple model for ion injection and transport in conducting polymers," *J. Appl. Phys.*, vol. 113, no. 24, p. 244501, 2013.

92. S. Goffri, C. Müller, N. Stingelin-Stutzmann, D. W. Breiby, C. P. Radano, J. W. Andreasen, R. Thompson, R. a. J. Janssen, M. M. Nielsen, P. Smith, and H. Sirringhaus, "Multicomponent semiconducting polymer systems with low crystallization-induced percolation threshold," *Nat. Mater.*, vol. 5, no. 12, pp. 950 – 956, 2006.

93. A. D. Scaccabarozzi and N. Stingelin, "Semiconducting:insulating polymer blends for optoelectronic applications - a review of recent advances," *J. Mater. Chem. A*, vol. 2, no. 28, pp. 10818 – 10824, 2014.

94. C. Müller, S. Goffri, D. W. Breiby, J. W. Andreasen, H. D. Chanzy, R. a. J. Janssen, M. M. Nielsen, C. P. Radano, H. Sirringhaus, P. Smith, and N. Stingelin-Stutzmann, "Tough, Semiconducting Polyethylene-poly(3-hexylthiophene) Diblock Copolymers," *Adv. Funct. Mater.*, vol. 17, no. 15, pp. 2674 – 2679, 2007.

95. N. Gomez and C. E. Schmidt, "Nerve growth factor-immobilized polypyrrole: Bioactive electrically conducting polymer for enhanced neurite extension," *J. Biomed. Mater. Res. Part A*, vol. 81, no. 4, pp. 771 – 780, 2007.

96. S. Ghosh and O. Inganäs, "Self-assembly of a conducting polymer nanostructure by physical crosslinking: applications to conducting blends and modified electrodes," *Synth. Met.*, vol. 101, pp. 413 – 416, 1999.

97. G.-L. Bao, W.-Q. Yun, S.-B. Fang, and Y.-Y. Jiang, "Ionic conductivity of polyelectrolyte derivatives of poly(vinyl alcohol) - lithium ion complex films," *Polym. Bull.*, vol. 18, pp. 143 – 148, 1987.

98. J. Chatterjee, T. Liu, B. Wang, and J. P. Zheng, "Highly conductive PVA organogel electrolytes for applications of lithium batteries and electrochemical capacitors," *Solid State Ionics*, vol. 181, pp. 531 – 535, 2010.

99. C. Hellmann, N. D. Treat, A. D. Scaccabarozzi, J. Razzell Hollis, F. D. Fleischli, J. H. Bannock, J. de Mello, J. J. Michels, J.-S. Kim, and N. Stingelin, "Solution processing of polymer semiconductor:insulator blends - Tailored optical properties through liquid-liquid phase separation control," *J. Polym. Sci. Part B Polym. Phys.*, vol. 53, pp. 304 – 310, 2015.

100. N. D. Treat, J. a. Nekuda Malik, O. Reid, L. Yu, C. G. Shuttle, G. Rumbles, C. J. Hawker, M. L. Chabinyc, P. Smith, and N. Stingelin, "Microstructure formation in molecular and polymer semiconductors assisted by nucleation agents," *Nat. Mater.*, vol. 12, no. 7, pp. 628 – 633, 2013.

101. D. Sparrowe, M. Baklar, and N. Stingelin, "Low-temperature printing of crystalline:crystalline polymer blend transistors," *Org. Electron.*, vol. 11, no. 7, pp. 1296 – 1300, 2010.

102. L. Qiu, J. A. Lim, X. Wang, W. H. Lee, M. Hwang, and K. Cho, "Versatile use of vertical-phase-separation-induced bilayer structures in organic thin-film transistors," *Adv. Mater.*, vol. 20, no. 6, pp. 1141 – 1145, 2008.

103. J. Jaczewska, I. Raptis, A. Budkowski, D. Goustouridis, J. Raczkowska, M. Sanopoulou, E. Pamula, A. Bernasik, and J. Rysz, "Swelling of poly(3-alkylthiophene) films exposed to

solvent vapors and humidity: Evaluation of solubility parameters," *Synth. Met.*, vol. 157, no. 18 - 20, pp. 726 – 732, 2007.

104. J. Zhao, W. Z. Yuan, A. Xu, F. Ai, Y. Lu, and Y. Zhang, "Perfluorinated sulfonic acid ionomer/poly(N-vinylpyrrolidone) nanofiber membranes: Electrospinning fabrication, water stability, and metal ion removal applications," *React. Funct. Polym.*, vol. 71, no. 11, pp. 1102 – 1109, 2011.

105. P. Westacott, J. R. Tumbleston, S. Shoaee, S. Fearn, J. H. Bannock, J. B. Gilchrist, S. Heutz, J. DeMello, M. Heeney, H. Ade, J. Durrant, D. S. McPhail, and N. Stingelin, "On the role of intermixed phases in organic photovoltaic blends," *Energy Environ. Sci.*, vol. 6, pp. 2756 – 2764, 2013.

106. C. Scharsich, R. H. Lohwasser, M. Sommer, U. Asawapirom, U. Scherf, M. Thelakkat, D. Neher, and A. Köhler, "Control of aggregate formation in poly(3-hexylthiophene) by solvent, molecular weight, and synthetic method," *J. Polym. Sci. Part B Polym. Phys.*, vol. 50, no. 6, pp. 442 – 453, 2012.

107. G. Horowitz, "The organic transistor: state-of-the-art and outlook," *Eur. Phys. J. Appl. Phys.*, vol. 53, no. 3, p. 33602, 2011.

108. D. Yu, Y. Q. Yang, Z. Chen, Y. Tao, and Y. F. Liu, "Recent progress on thin-film encapsulation technologies for organic electronic devices," *Opt. Commun.*, vol. 362, pp. 43 – 49, 2016.

109. M. S. A. Abdou, F. P. Orfino, Y. Son, and S. Holdcroft, "Interaction of oxygen with conjugated polymers: Charge transfer complex formation with poly(3-alkylthiophenes)," *J. Am. Chem. Soc.*, vol. 119, no. 19, pp. 4518 – 4524, 1997.

110. G. H. Gelinck, T. C. T. Geuns, and D. M. de Leeuw, "High-performance all-polymer integrated circuits," *Appl. Phys. Lett.*, vol. 77, no. 10, pp. 1487 – 1489, 2000.

111. E. J. Meijer, C. Detcheverry, P. J. Baesjou, E. Van Veenendaal, D. M. De Leeuw, and T. M. Klapwijk, "Dopant density determination in disordered organic field-effect transistors," *J. Appl. Phys.*, vol. 93, no. 8, pp. 4831 – 4835, 2003.

112. C.-H. Chang, M.-F. Chen, and C.-H. Chien, "An Investigation of Transient Effects in Poly(3-hexylthiophenes) Based Thin Film Transistors Caused by Oxygen and Water Molecules," *J. Electrochem. Soc.*, vol. 158, no. 9, pp. H854 – H859, 2011.

113. S. Hoshino, M. Yoshida, S. Uemura, T. Kodzasa, N. Takada, T. Kamata, and K. Yase, "Influence of moisture on device characteristics of polythiophene-based field-effect transistors," *J. Appl. Phys.*, vol. 95, no. 2004, pp. 5088 – 5093, 2004.

114. W. Boukhili, M. Mahdouani, M. Erouel, J. Puigdollers, and R. Bourguiga, "Reversibility of humidity effects in pentacene based organic thin-film transistor: Experimental data and electrical modeling," *Synth. Met.*, vol. 199, pp. 303 – 309, 2015.

115. a. B. Mostert, B. J. Powell, F. L. Pratt, G. R. Hanson, T. Sarna, I. R. Gentle, and P. Meredith, "Role of semiconductivity and ion transport in the electrical conduction of melanin," *Proc. Natl. Acad. Sci.*, vol. 109, no. 23, pp. 8943 – 8947, 2012.

116. P. Meredith, C. J. Bettinger, M. Irimia-Vladu, a. B. Mostert, and P. E. Schwenn, "Electronic and optoelectronic materials and devices inspired by nature," *Reports Prog. Phys.*, vol. 76, no. 3, p. 034501, 2013.

117. L. J. van der Pauw, "A Method of Measuring Specific Resistivity and Hall Effect of Discs of Arbitrary Shape," *Philips Res. Reports*, vol. 13, no. 1, pp. 1 – 9, 1958.

118. A. B. Mostert, *Proton conduction in biomacromolecules: The search for the dominant charge carrier within melanin.* Honours thesis, University of Queensland, 2006.

119. C. Eames, J. M. Frost, P. R. F. Barnes, B. C. O'Regan, A. Walsh, and M. S. Islam, "Ionic transport in hybrid lead iodide perovskite solar cells," *Nat. Commun.*, vol. 6, p. 7497, 2015.

120. C. J. T. von Grotthuss, "Sur la décomposition de l'eau et des corps qu'elle tient en dissolution à l'aide de l'électricité galvanique," *Ann. Chim.*, vol. 58, pp. 54 – 73, 1806.

121. L. Chua, "Memristor - The Missing Circuit Element," *IEEE Trans. circuit theory*, vol. 18, no. 5, pp. 507 – 519, 1971.

122. D. B. Strukov, G. S. Snider, D. R. Stewart, and R. S. Williams, "The missing memristor found," *Nature*, vol. 453, pp. 80 – 83, 2008.

123. Y. Aoki, C. Wiemann, V. Feyer, H.-S. Kim, C. M. Schneider, H. Ill-Yoo, and M. Martin, "Bulk mixed ion electron conduction in amorphous gallium oxide causes memristive behaviour.," *Nat. Commun.*, vol. 5, p. 3473, 2014.

Appendices

Appendix A

Electrochromic testing

The data presented in this appendix complement that of Chapter 3, Sections 3.3.3 and 3.3.4, in which the real-time electrochromism of materials **2** - **5** is characterised. Full collection of samples (in triplicate) of each material is presented, providing their raw absorbance spectra over time, the corresponding spectra normalised to the absorbance at 550 nm at $t = 0$ s and the relative absorbance spectra at 550 nm vs. time for the complete bias run (subsequently, $V_{ON} = 0.75$ V, $V_{OFF} = 0$ V and $V_{REV} = -0.75$ V, for a duration of 28 s each).

Films of materials **2** and **3** (Figures A.1 and A.2) were also prepared using THF as solvent (shown as sample "s3" in both cases). Although the dynamics of the electrochromism remains unchanged, $CHCl_3$ was a better solvent as assessed by the improved quality of the films produced (reduced formation of large aggregates/particles that could be observed by eye).

2: P3HT(C6OH)$_{10\%}$

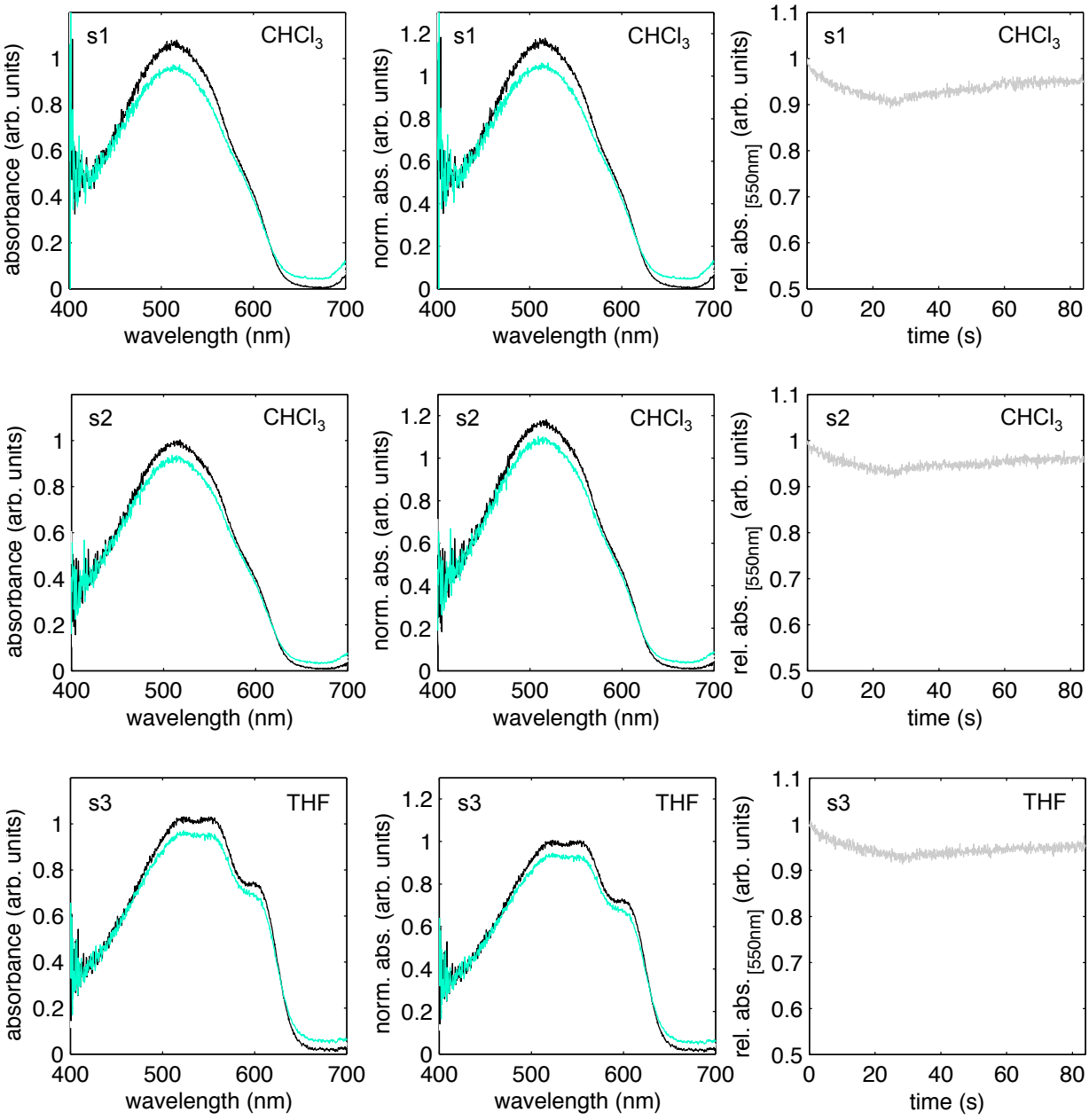


Figure A.1: From top to bottom rows: samples 1 - 3 (s1 - s3) of material **2:** P3HT(C6OH)$_{10\%}$. **Left:** Real-time absorbance during applied bias V_{ON}. **Centre:** Normalised absorbance to that at 550 nm at time $t = 0$ s. **Right:** Relative absorbance at 550 nm vs. time during $V_{ON} = 0.75$ V (0 - 28 s), $V_{OFF} = 0$ V (28 - 56 s) and $V_{REV} = -0.75$ V (56 - 84 s).

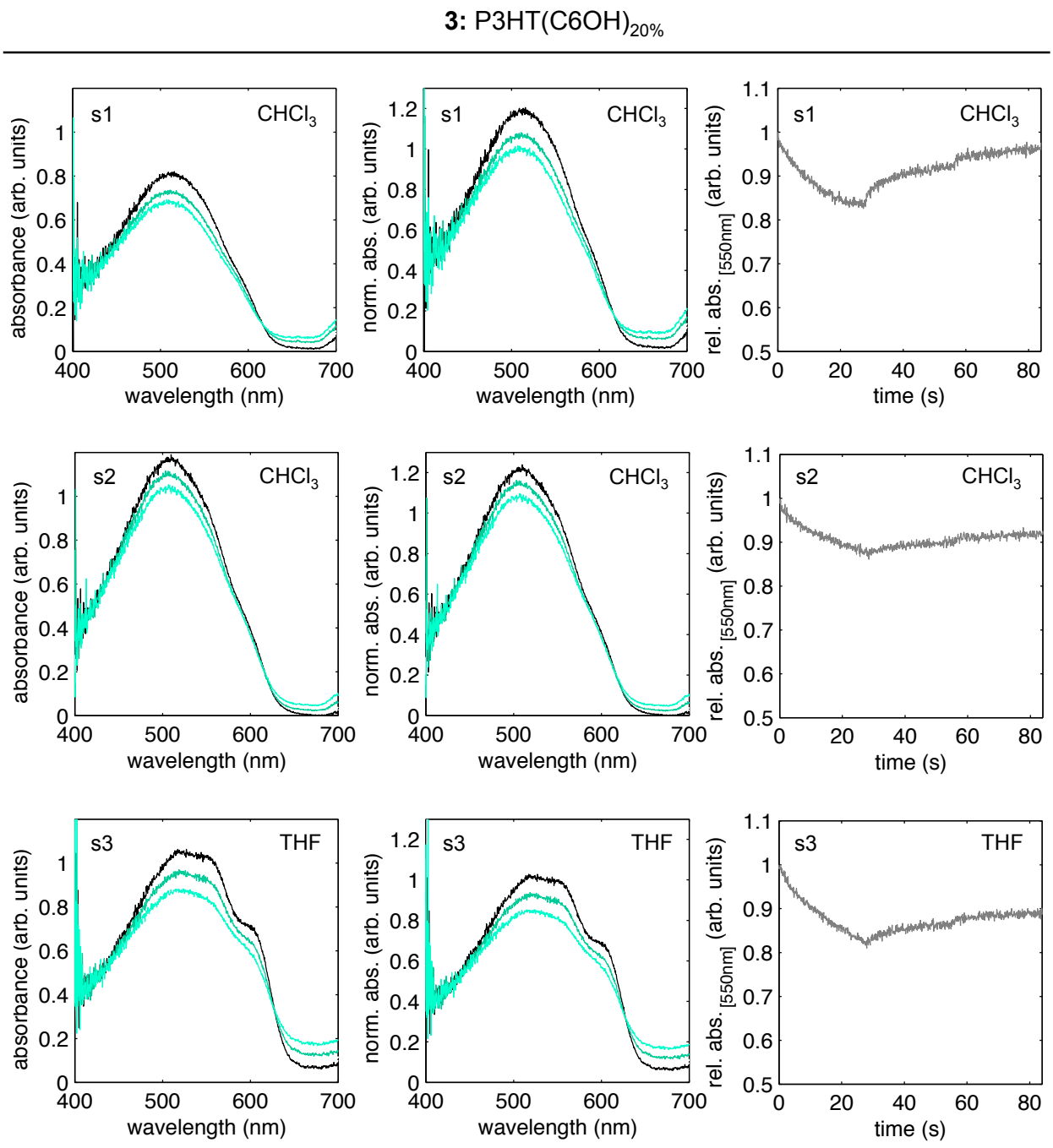


Figure A.2: From top to bottom rows: samples 1 - 3 (s1 - s3) of material **3:** P3HT(C6OH)$_{20\%}$. **Left:** Real-time absorbance during applied bias V_{ON}. **Centre:** Normalised absorbance to that at 550 nm at time $t = 0$ s. **Right:** Relative absorbance at 550 nm vs. time during $V_{ON} = 0.75$ V (0 - 28 s), $V_{OFF} = 0$ V (28 - 56 s) and $V_{REV} = -0.75$ V (56 - 84 s).

4: P3HT(C6OH)$_{50\%}$

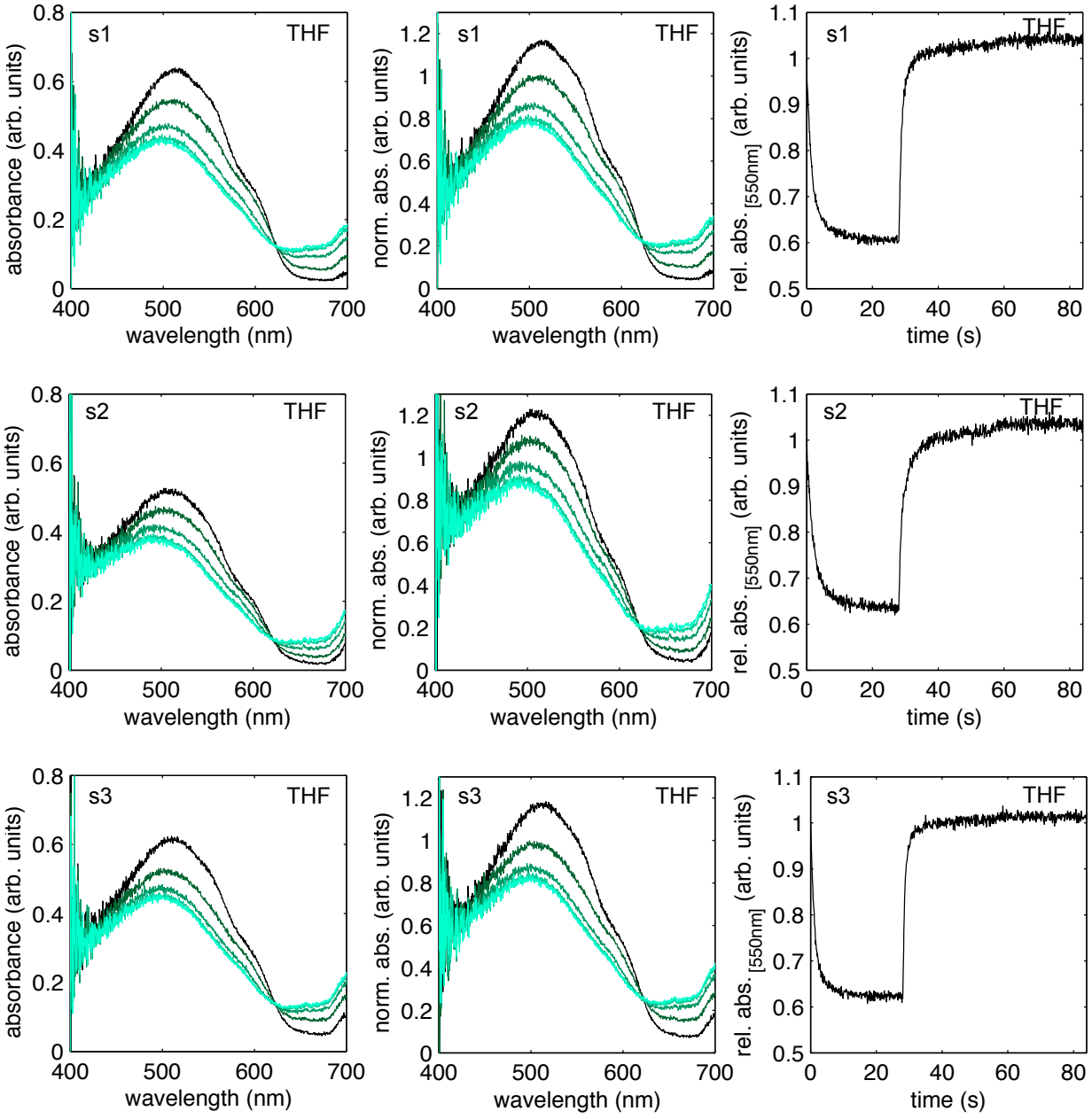


Figure A.3: From top to bottom rows: samples 1 - 3 (s1 - s3) of material **4:** P3HT(C6OH)$_{50\%}$. **Left:** Real-time absorbance during applied bias V_{ON}. **Centre:** Normalised absorbance to that at 550 nm at time $t = 0$ s. **Right:** Relative absorbance at 550 nm vs. time during $V_{ON} = 0.75$ V (0 - 28 s), $V_{OFF} = 0$ V (28 - 56 s) and $V_{REV} = -0.75$ V (56 - 84 s).

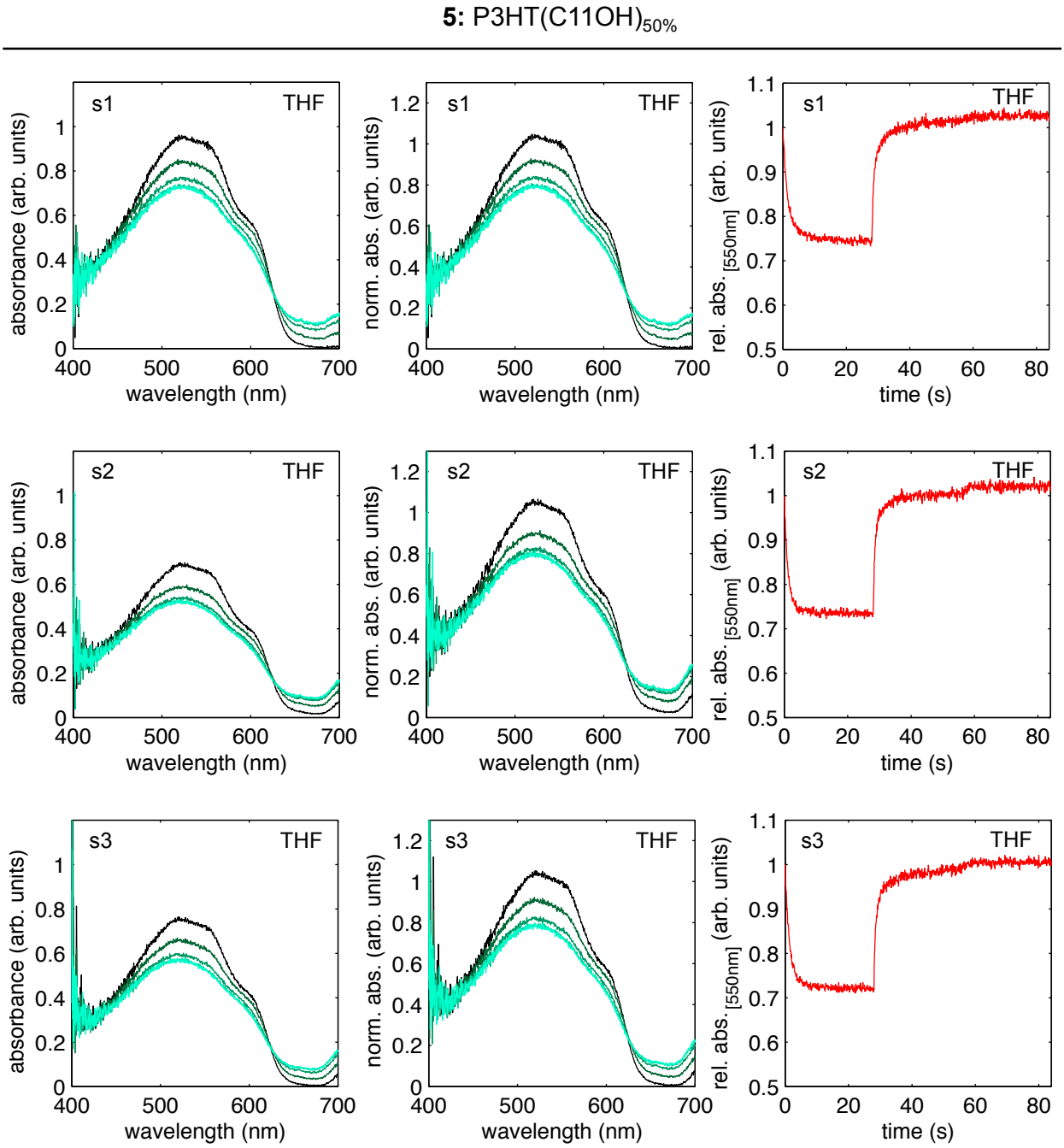


Figure A.4: From top to bottom rows: samples 1 - 3 (s1 - s3) of material **5:** P3HT(C11OH)$_{50\%}$. **Left:** Real-time absorbance during applied bias V_{ON}. **Centre:** Normalised absorbance to that at 550 nm at time $t = 0$ s. **Right:** Relative absorbance at 550 nm vs. time during $V_{ON} = 0.75$ V (0 - 28 s), $V_{OFF} = 0$ V (28 - 56 s) and $V_{REV} = -0.75$ V (56 - 84 s).